Leibniz-Institut für
Astrophysik Potsdam

Potsdam University
Leibniz Institute for Astrophysics Potsdam (AIP)

Analysing the Magnetic Field Evolution in the Intracluster Medium

---

Larissa Tevlin
Matriculation Number 812126

Supervisor:	**Prof. Dr. Christoph Pfrommer**
First Referee:	**Prof. Dr. Christoph Pfrommer**
Second Referee:	**Prof. Dr. Tim Dietrich**

A thesis submitted for the degree
Master of Science
May 2023

Abstract

Galaxy clusters consist of hundreds to thousands of galaxies. The space between the galaxies is filled with a hot plasma, known as the intracluster medium (ICM). Galaxy clusters are magnetised. Radio observations reveal that the magnetic fields, embedded into the ICM, have field strengths of $\sim \mu$G and coherence lengths of $\sim$ kpc. The details about how these magnetic fields are created and how they evolve to the observed state are not yet fully known. Magnetic fields in galaxy clusters can be created in structure formation processes via means of the Biermann battery at the order of $\approx 10^{-20}$G. Theories suggest that, starting with a small seed field, the magnetic fields in the ICM can be amplified to the observed strengths. The underlying process is referred to as a turbulent small-scale dynamo. It converts turbulent, kinetic energy into magnetic energy. Non-radiative galaxy cluster simulations show that the turbulent small-scale dynamo is able to grow magnetic fields to the observed strengths within the age of the universe. In the framework of this thesis, we analyse how adding radiative physics modifies this picture. We analyse the fifth most massive galaxy cluster with a mass of $\sim 3 \cdot 10^{15}$M$_\odot$ from a cosmological simulation. We analyse two different simulations of this galaxy cluster. The first simulation includes a module for solving the ideal magnetohydrodynamics (MHD) equations, a gravity solver and a module for radiative physics. The second simulation only includes the MHD and the gravity module. We analyse and compare both simulations. The magnetic field grows faster in the radiative simulation. In the radiative simulation, the magnetic field reaches the final strength of $\sim 5\mu$G in the central regions at a redshift of $z \approx 3.5$. In the non-radiative simulation, this happens at $z \approx 1$. The galaxies in the radiative simulation grow magnetic fields with strengths of $\sim 20\mu$G approximately within the same time. The magnetic field grows in three epochs in the radiative simulation. After the collapse of the protocluster, from $9.5 > z > 4.5$, the magnetic field grows mainly in the central ICM. The center is dominated by the high densities and feedback induced turbulence in the central galaxy of the cluster. After the first merger, from $4.5 > z > 3.5$, the magnetic field experiences an exponential growth phase. The exponential growth is associated with the galactic magnetic fields. These are injected into the ICM via galactic winds or ram pressure stripping. The merger at $z = 4.5$ injects turbulence into the ICM such that the turbulent small-scale dynamo can pick up the high galactic magnetic fields as initial fields and amplify them until $z = 3.5$. From $z = 3.5$ on, merging substructures enrich the ICM with their own gas. The gas has a similar magnetic field strength, compared to the ICM. The merging substructures also keep the level of turbulence in the ICM high. This turbulence feeds the magnetic field, which would otherwise decay, and mixes central and higher radii ICM. Inside galaxies, the magnetic field grows fast due to high gas densities and a high level of turbulence. A large fraction of galaxies loses all their gas. This starts already at $z = 9$. This fraction grows with time. We see evidence for ram pressure stripping, as well as for galactic winds caused by supernovae. The magnetic field profile evolution is closely related to the metallicity profile evolution. Furthermore, there is a positive correlation between the metallicity and the magnetic field strength in the ICM from $z = 2$ on. The similarity between the magnetic field and metallicity distributions in the ICM shows, how closely related galactic magnetic fields are to those in the ICM. In the non-radiative simulation, the magnetic field experiences an initial growth of the magnetic field with the collapse of the protocluster. Afterwards, it stays constant between the redshifts $9.5 > z > 4.5$. We define two growth phases for the following growth of the magnetic field in the non-radiative simulation. Between the first and the second major mergers, at $4.5 > z > 2$ it starts to grow exponentially. After the second merger at $2 > z > 1$ it grows with an increased rate. The amount of turbulence is approximately the same in both simulations. Only the very central ICM shows an increased level of turbulence at $9.5 > z > 4.5$ in the radiative simulation. Our findings are an important step towards understanding the evolution of the magnetic field in galaxy clusters and the contribution of galaxies and their interactions with the ICM. Understanding the evolution of magnetic fields is important as they are intrinsically linked to physical processes in the ICM such as conduction, viscosity, cosmic ray acceleration and transport, and the observed radio emission.

Zusammenfassung

Galaxienhaufen enthalten hunderte bis tausende Galaxien. Den Raum zwischen den Galaxien füllt ein heißes Plasma, bekannt als das Intracluster Medium (ICM). Galaxienhaufen sind magnetisiert. Radio Observationen zeigen, dass die Magnetfelder, eingebettet in das ICM, Feldstärken im Bereich $\sim \mu$G und Kohärenzlängen von $\sim$ kpc haben. Die Details darüber, wie diese Magnetfelder entstehen und wie sie sich entwickeln sind noch nicht komplett bekannt. Magnetfelder in Galaxienhaufen können in Strukturformationsprozessen mit der Biermann Batterie in der Größenordnung von $\approx 10^{-20}$G kreiert werden. Theorien zufolge können kleine Ausgangs-Magnetfelder durch einen Prozess namens turbulenter Dynamo zu den beobachteten Stärken amplifiziert werden. Der turbulente Dynamo konvertiert turbulente, kinetische Energie in magnetische Energie. Nicht-radiative Simulationen von Galaxienhaufen zeigen, dass der turbulente Dynamo Magnetfelder mit den beobachteten Stärken im Alter des Universus erzeugen kann. Im Rahmen dieser These analysieren wir, wie radiative physikalische Prozesse dieses Bild modifizieren. Wir analysieren den fünft massereichsten Galaxienhaufen mit $\sim 3 \cdot 10^{15}$M$_\odot$ aus einer kosmologischen Simulation. Wir analysieren zwei verschiedene Simulationen von diesem Galaxienhaufen. Die erste Simulation enthält ein Modul für die magnetohydrodynamischen (MHD) Gleichungen, einen Gravitations-Solver und ein Modul für radiative Prozesse. Die zweite Simulation enthält nur das MHD Modul und den Gravitations-Solver. Wir analysieren und vergleichen beide Simulationen. Das Magnetfeld wächst schneller in der radiativen Simulation. In der radiativen Simulation erreicht das Magnetfeld die finale Stärke von $\sim 5\mu$G bei einer Rotverschiebung von $z = 3.5$. In der nicht-radiativen Simulation wird das bei einer Rotverschiebung von $z \approx 1$ erreicht. Die Galaxien in der radiativen Simulation haben Magnetfelder mit Stärken $\sim 20\mu$G, die etwa zur selben Zeit erreicht werden. Das Magnetfeld in der radiativen Simulation wächst in drei Epochen. Nach dem Kollaps des Proto-Galaxienhaufens, von $9.5 > z > 4.5$, wächst das Magnetfeld primär im zentralen ICM. Das Zentrum wird von den hohen Dichten und Feedback-induzierten Turbulenzen der zentralen Galaxie dominiert. Nach dem ersten Merger $4.5 > z > 3.5$, wächst das Magnetfeld exponentiell. Das exponentielle Wachstum ist verbunden mit den Magnetfeldern in Galaxien. Die galaktischen Magnetfelder können durch Staudruck oder galaktische Winde mit dem ICM vermischt werden. Der Merger bei $z = 4.5$ versetzt das ICM mit Turbulenzen, so dass der turbulente Dynamo die galaktischen Magnetfelder als Ausgangsfelder nutzen kann und so die Magnetfelder im ICM bis $z = 3.5$ verstärken kann. Ab $z = 3.5$ mixen Merger ihr eigenes Gas, welches eine ähnliche Magnetfeldstärke hat, mit dem ICM. Die Merger sorgen auch für ein konstant hohes Turbulenz-Level im ICM. Diese Turbulenzen füttern das Magnetfeld, welches sonst zerfallen würde, und sie mixen zentrales ICM mit äußerem ICM. Eine große Fraktion aller Galaxien verliert ihr Gas. Dieser Prozess startet schon ab $z = 9$. Diese Fraktion wird mit der Zeit größer. Wir sehen Hinweise darauf, dass das Gas durch Staudruck oder galaktische Winde entfernt wird. Die Evolution des Profils des Magnetfeldes weist große Ähnlichkeiten zu dem Profil der Metallizität auf. Wir sehen eine positive Korrelation zwischen der Metallizität und der Magnetfeldstärke, beginnend ab $z = 2$. Die Ähnlihkeit zwischen Magnetfeld und Metallizität im ICM zeigt, wie eng galaktische Magnetfelder und die im ICM, miteinander verbunden sind. Auch in der nicht-radiativen Simulation erfährt das Magnetfeld ein erstes Wachstum mit dem Kollaps des Proto-Galaxienhaufens. Darauf bleibt das Magnetfeld konstant zwischen $9.5 > z > 4.5$. Wir definieren zwei Wachstumsphasen für das Magnetfeldwachstum danach. Zwischen dem ersten und dem zweiten größeren Merger, $4.5 > z > 2$ beginnt es, exponentiell zu wachsen. Nach dem zweiten Merger, zwischen $2 > z > 1$, wächst es mit einer erhöhten Rate. Das Level an Turbulenzen ist ungefähr gleich in beiden Simulationen. Nur das zentrale ICM zeigt ein leicht erhöhtes Level an Turbulenzen zwischen $9.5 > z > 4.5$ in der radiativen Simulation. Unsere Ergebnisse sind ein wichtiger Schritt hin zu dem Verständnis von der Evolution von Magnetfeldern in Galaxienhaufen und wie Galaxien damit zusammenhängen. Es ist wichtig, dass wir Magnetfelder verstehen, da sie fundamental sind um physikalische Prozesse, wie Konduktion, Viskosität, die Beschleunigung und den Transport von kosmischer Strahlung und die beobachtete Radio Strahlung zu begreifen.

Acknowledgement

This thesis would have not been possible without the stunning contribution of human individuals in my life. I want to thank Dr. Thomas Berlok for his professional assistance, long discussions and endless E-Mail exchanges. I want to thank Prof. Dr. Christoph Pfrommer for giving me motivation boosts. Also, a special thank to my family, friends and boyfriend who support me with their love (and English writing skills).

Thank you to everybody in the Cosmology section at AIP for making this last year a wonderful experience and providing a comfortable working environment.

Contents

1 Introduction

The Universe is magnetised. Astrophysical magnetic fields can be found across a great range of different scales (Donnert et al., 2018). These scales reach from stars (10^6km), at the small scales to galaxy clusters ($\sim$ Mpc), the biggest gravitationally collapsed objects that we know of (Reblinsky, 2000). Magnetic fields in galaxy clusters can be observed via synchrotron emission at radio wavelengths (van Weeren et al., 2009; Botteon et al., 2022). Other measurement methods go via the Faraday rotation measure (Taylor et al., 2001; van Weeren et al., 2019; Osinga et al., 2022). How are magnetic fields in galaxy clusters created? What amplifies them? So far, there is no definite answer. There are different astrophysical mechanisms that can potentially produce magnetic fields in galaxy clusters, similar to the ones that we observe.

Numerical simulations are a useful tool to investigate these questions. The creation and amplification of magnetic fields has been studied in simulations of stars, galaxies, galaxy clusters and whole cosmological boxes. These simulations differ in their setups. The objects can be simulated in isolation, which means that there is no large scale interaction with the environment. Or they are simulated as part of a bigger cosmological box, where environmental effects can heavily influence the simulated object. Furthermore, the simulations can include radiative physics, meaning a model for gas cooling, star formation, black hole formation and associated feedback models is included in the simulation. To choose a setup, it is a question of computational power, desired output and availability. To be mentioned are simulations of galaxy clusters that investigate the evolution of the magnetic field performed by other groups. Marinacci et al. (2015) perform a cosmological simulation, where they run a setup, including radiative physics and the other one, only using adiabatic considerations. They analyse the magnetic field evolution in the cosmological box. Miniati & Beresnyak (2015b) simulate an isolated cluster using the CHARM code without radiative physics. The structure formation induced feedback is reconstructed from a merger history code. Roh et al. (2019) also simulate an isolated cluster without radiative physics. Interactions with the environment are computed separately and inforced. Basu & Sur (2021) use the FLASH code to simulate a non-radiative, isolated cluster. Also here, the environmental interactions are inforced. Vazza et al. (2018) use the ENZO code to perform a cosmological simulation of a galaxy cluster. They do not include radiative physics. Steinwandel et al. (2022) do a cosmological, non-radiative simulation using the GADGET3 cosmological code. Adduci Faria et al. (2020) studied the magnetic field in a whole cosmological box, including galaxies, clusters and filaments. They only add passive magnetic fields in equipartition with the thermal gas pressure, instead of actively simulating the magnetic field. Donnert et al. (2018) review the magnetic field evolution in simulated galaxy clusters. Most of the simulations come with the problem that a large variety in scales must be covered in order to properly simulate the magnetic field. The scales reach from small objects, for example supernovae to large objects, for example merger with other clusters. All these processes can influence the magnetic field.

What is our understanding on the magnetic field evolution in galaxy clusters so far? Magnetic seed fields can be created in the early Universe. With the so called Biermann battery (Biermann, 1950; Kunz et al., 2022), an astrophysical battery that uses baroclinic motions of charged gas, magnetic fields can be created from scratch. Such a baroclinic motion can be induced in different scenarios: structure formation processes, ionization fronts or in supernovae to mention a few (Miranda et al., 1998; Furlanetto & Loeb, 2001; Kulsrud et al., 1997; Zhao et al., 2008; Doi & Susa, 2011; Garaldi et al., 2021; Mtchedlidze et al., 2021). These weak seed fields can be amplified via adiabatic compression, for example in gravitationally collapsed gas or in cooled gas (see e.g. Pfrommer 2022). They

can also be amplified non-adiabatically, in a turbulent medium, such as the gas in galaxy clusters. Merger, as well as interactions with galaxies constantly inject turbulence in galaxy clusters (Wittor et al., 2017; Vazza et al., 2017; Wittor & Gaspari, 2020). The amplification works in such a way that the turbulence stretches the magnetic field lines. This effect is especially applicable to small scale turbulence, that has a shorter timescale and can faster stretch the magnetic field. This process is also referred to as turbulent small-scale dynamo (Kunz et al., 2022). It is described with the Kazantsev theory (Kazantsev, 1968; Kraichman, 1966).

The turbulent small-scale dynamo cannot only work in galaxy clusters, but also in galaxies (Schober et al., 2013) and stars (Schober et al., 2012). Here, stars can grow a strong magnetic field and carry it to the gas in galaxies through supernova explosions. This also adds a high amount of turbulence to the gas (de Gouveia Dal Pino et al., 2009), giving potentially rise to a turbulent small-scale dynamo. Due to their smaller length scales and shorter dynamical timescales, galaxies can grow a strong magnetic field in a short period of time. Galaxies can potentially lose their gas due to feedback processes that cause galactic winds (Heckman et al., 1990; Veilleux et al., 2005). In galaxy clusters, galaxies can also lose their gas due to interactions with the gas in clusters (Jáchym et al., 2019; Serra et al., 2023). Thus, galaxies provide a source for a fast amplification of the magnetic field in galaxy clusters.

We analyse the evolution of the magnetic field in galaxy clusters in a cosmological, radiative simulation with active magnetic field simulation. In a cosmological simulation, the environmental effects are included, while in a radiative simulation, galaxy formation and associated feedback is included. We want to tackle the question: how does including radiative physics influence the magnetic field evolution in galaxy clusters? In order to investigate this, we run a cosmological simulation with two different setups: one, where we enable radiative physics and one, where we disable it. We compare the magnetic field evolution in both simulations. We use the cosmological moving-mesh code AREPO (Springel, 2010) with a module for magnetohydrodynamics (Springel, 2010; Pakmor et al., 2011) to simulate a cosmological box. We run a zoom-in technique on postselected galaxy clusters (Springel et al., 2001). We use the galaxy formation module FABLE (Henden et al., 2018) to simulate the run including radiative physics.

In section 2, we give the theoretical background. We describe what a galaxy cluster is, how it evolves together with the Universe, we describe the gas dynamics in galaxy clusters and how the magnetic field is embedded into this gas. We summarize the physics of the magnetic field evolution: the seed field creation with the Biermann battery and the amplification with the turbulent small-scale dynamo. Then, we also give an overview on galaxy evolution. We focus on the effects that are connected to the magnetic field evolution: the evolution of stars and stellar feedback, galactic winds and interactions with the cluster. For each of these topics, we give a description on how we model these physical processes in our simulation. In section 3, we analyse the magnetic field growth in our simulation. In section 4, we summarize the most important results and eventually give an outlook.

2 Background

What kind of information do we need in order to understand, how the magnetic field in galaxy clusters evolves with time? How can we simulate this? This section provides the needed background to answer these questions. The section is split into four subsections: Cosmological evolution, the intracluster medium, magnetic fields and galaxies. Each subsection begins the topic with an observational introduction. Then, the theory is explained. Eventually, every subsection provides the information on how we exactly simulate this.

In order to understand the evolution of magnetic fields in galaxy clusters, understanding the development of galaxy clusters, within cosmic history, is important. The evolution of galaxy clusters is tightly related to the evolution of the Universe. According to the theory of hierarchical structure formation, they form latest, building up on previous steps of structure formation (Kravtsov & Borgani, 2012). We give an overview on the cosmological evolution of galaxy clusters in subsection 2.1.

Galaxy clusters are filled with a hot, $\sim 10^7$-10^8K gas, called the intracluster medium (ICM). The ICM is so hot, that mostly all particles are thermally ionized (Mohr et al., 1999). This makes the magnetic field embedded into this hot plasma. It is strongly dependent on the dynamics in the ICM and vice versa. We introduce the hydrodynamical properties of the ICM in subsection 2.2.

There are different mechanisms that can create weak astrophysical magnetic fields (Mtchedlidze et al., 2022; Rees, 1987; Andreasyan, 1996; Gnedin et al., 2000; Durrive & Langer, 2015). Astrophysical magnetic fields can be amplified with the turbulent small-scale dynamo. It converts turbulent kinetic energy into magnetic energy (Schober et al., 2012; Pakmor et al., 2020; Kunz et al., 2022; Pfrommer et al., 2022). Magnetic fields in galaxy clusters are introduced in subsection 2.3.

Galaxy clusters contain hundreds to thousands of galaxies (Zenteno Vivanco, 2014). This makes them dependent on the evolution and dynamics of the galaxies and vice versa. Galaxies have shorter dynamical times as well as higher density gas. This can enable the turbulent dynamo to work more efficiently (Kunz et al., 2022). The gas can be removed from galaxies by galactic winds or ram pressure stripping (Wada et al., 2009; Gent et al., 2023; Van De Ven et al., 2009; Serra et al., 2023). This enables the galaxies to pollute the ICM with their gas. We give an overview on galaxies in galaxy clusters in subsection 2.4

2.1 Cosmological Evolution

Galaxy clusters are the largest collapsed objects that we know of (Reblinsky, 2000). They are the product of ongoing structure formation during cosmic history and they are still forming today (Kravtsov & Borgani, 2012). This makes them strongly coupled to the evolution of the cosmos. This section describes the evolution of galaxy clusters dependent on the evolution of the cosmos. Additionally, we introduce, how sizes and masses of galaxy clusters can be described.

2.1.1 Observations and the General Picture

What is a galaxy cluster? Galaxy clusters are an assemble of galaxies. They contain hundreds to thousands of galaxies (Zenteno Vivanco, 2014). Galaxy cluster's masses range between $\sim 10^{14}-10^{15} M_{\odot}$ (Snowden et al., 2008). The radii lie in the range of a few hundred kpc to a few Mpc (Rees & Ostriker, 1977). Galaxy clusters are rare objects. Figure 1 shows a galaxy cluster. The picture was taken with the Hubble Space Telescope that records in the optical. The picture shows hundreds of galaxies with the brightest ones in the center. Optical matter though makes only $\sim 2\%$ of the total matter content (see e.g. Pfrommer 2022). Most of the matter is in the form of dark matter.

Figure 1: The galaxy cluster ACO S 295. The image is taken by the Hubble Space Telescope. The cluster contains hundreds of galaxies. This image shows optical and infrared wavelengths. Image credit: NASA / ESA / Hubble / F. Pacaud / D. Coe.

Galaxy clusters are the product of ongoing structure formation. Structure formation is dominated by the gravitational interaction of dark matter. At large scales, the matter in the Universe forms to build the so called cosmic web. Galaxy clusters sit as overdense knots in this cosmic web. They connect smaller substructures.

How does the cosmic web form? Figure 2 shows temperature anisotropies in the cosmological microwave background (CMB). This is the oldest light in the Universe. It was released 380000 years after the Big Bang, when baryonic matter and radiation decoupled. Dark matter only interacts gravitationally. It has already build substructures at this early time through gravitational interactions. These density fluctuations are the seeds for structure formation. They are imprinted onto the CMB. In figure 2, the red areas show regions with slightly higher temperatures. These correspond to regions with higher densities. The blue areas correspond to regions with lower densities. Once, the baryonic matter and radiation are decoupled, the baryonic matter follows the potential wells of the dark matter substructures. The first stars and galaxies start to form. The very first galaxies grow with time. They keep attracting less massive substructures. At later times, even smaller mass

galaxy clusters can be attracted (Kravtsov & Borgani, 2012). Galaxy clusters form in the most dense regions as the endproducts (so far) of previous structure formation steps.

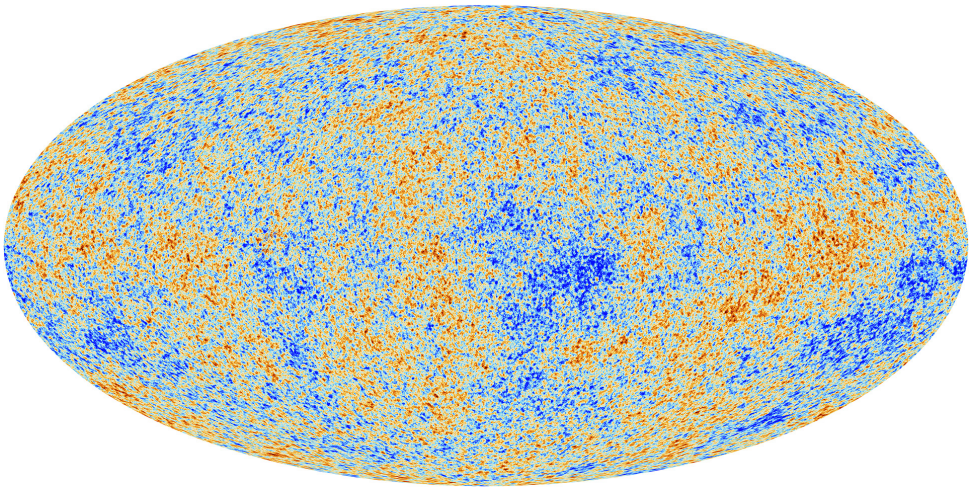

Figure 2: Anisotropies in the CMB. The light was emitted 380 000 years after the Big Bang. At this time, matter and radiation decoupled. Seeds of structure formation are imprinted onto the CMB. Blue regions shows underdense regions with slightly lower temperatures, whereas red indicates slightly overdense regions; higher temperatures. Image credits: ESA Planck Collaboration

The central galaxies in galaxy cluster are giant elliptical galaxies. They are also referred to as Brightest Cluster Galaxies (BCGs) (De Lucia & Blaizot, 2007; O'Dea et al., 2010; Laporte et al., 2013; Ito et al., 2019; Kubo et al., 2021). These BCGs are the most massive galaxies Universe wide (De Lucia & Blaizot, 2007; Von Der Linden et al., 2007). The BCGs contain the most massive black holes universe wide (Von Der Linden et al., 2007). Active Galactic Nuclei (AGN) are powered by these Supermassive black holes. Also the AGN grow constantly in time through attraction of matter and merging with other black holes. Feedback from AGN influences the dynamics in the centers of clusters (Ehlert et al., 2021).

2.1.2 Cosmological Model

How can we describe this analytically? The key assumptions to do cosmology are isotropy and homogeneity (Bartelmann, 2012): on large scales , the Universe looks the same at every position, no matter what direction we are looking into. We introduce the scale factor a as a proxy for the size of the Universe. Conveniently, we set $a = 1$ nowadays. In order to map this to observations, we translate the scale factor to a redshift z:

$$z = \frac{1}{a} - 1. \tag{1}$$

The most widely used cosmological model is the Lambda Cold Dark Matter (ΛCDM) model (Springel & Hernquist, 2003; Baugh et al., 2005; Gao et al., 2008; Meng & Dou, 2009; Governato et al., 2012). With the ΛCDM model, we describe the evolution of the cosmos with time, ranging from shortly after the Big Bang, until now. According to this model, the large scale dynamics of the Universe is dominated by cold dark matter and dark energy (Λ). The expansion of the universe is described with the Friedmann equation (Bartelmann, 2012; Meng et al., 2005; Meng & Dou, 2009):

$$H^2(a) = H_0^2(a)\left[\Omega_{\mathrm{m0}} a^{-3} + \Omega_\Lambda\right], \tag{2}$$

where $H(a) = \dot{a}/a$ is the scale factor dependent Hubble function. It describes the velocity of the expansion in units of the scale factor a. Here, $H_0 = \dot{a}(t_0)/a(t_0) = 100h\mathrm{kms}^{-1}\mathrm{Mpc}^{-1}$ is the Hubble constant. The density components Ω_{m0} and Ω_λ are the fraction of matter energy density and dark energy density over the critical energy density respectively. We treat the density components by relating the actual density to the so called critical density $\Omega(t) = \rho(t)/\rho_{\mathrm{cr}}(t)$. Here, the critical density is (Bartelmann, 2012; Wang & Steinhardt, 1998)

$$\rho_{\mathrm{cr}} = \frac{3H^2}{8\pi G}, \tag{3}$$

i.e. a sphere filled with this density can gravitationally exactly balance it's kinetic energy. Here, G is the gravitational constant. From the latest measurements of the Planck satellite (Aghanim et al., 2020), $h = 0.67$, $\Omega_{\mathrm{m0}} = 0.315$ and $\Omega_\Lambda = 0.685$. We have set the curvature energy density and the radiation energy density to zero. Most of the matter is in the form of dark matter (White & Frenk, 1991; Meng & Dou, 2009). For small scale factors, the expansion is dominated by (mostly) dark matter. For $a > 1$, it is dominated by dark energy. To make estimates about cosmological times, we rearrange (2) and integrate (Bartelmann, 2012):

$$H_0 t = \int_0^a \frac{\sqrt{a'}da'}{\sqrt{\Omega_{\mathrm{m0}} + \Omega_\Lambda a'^3}}. \tag{4}$$

The result is (Bartelmann, 2012):

$$H_0 t = \frac{2}{3\sqrt{1-\Omega_{\mathrm{m0}}}}\mathrm{arcsinh}\left[\sqrt{\frac{\Omega_{\mathrm{m0}}-1}{\Omega_{\mathrm{m0}}}}a^{3/2}\right]. \tag{5}$$

With equation (2), we can make assumptions on how clusters form, when they form and with which abundances. We do this by describing the amplitude of a density contrast with the variance of a Gaussian distribution. The abundance of these overdensities can be estimated with a Gaussian probability function. The growth of the overdensities can be described with equation (2) (Kravtsov & Borgani, 2012). Once, the overdensities reach a certain amplitude, they collapse and start to form the first dark matter halos.

How can we describe the sizes and masses of galaxy clusters? Galaxy clusters evolve together with their surroundings. One common approach to define the size of a galaxy cluster is to define it via the critical density (Pfrommer, 2022; Press & Davis, 1982):

$$200 \cdot \rho_{\mathrm{cr}} = \frac{M_{200}}{\frac{4}{3}\pi R_{200}^3}. \tag{6}$$

We take a sphere with radius R_{200} and a mass M_{200}, so that the mean density inside the sphere is 200 times the critical density.

We can assign a corresponding characteristic temperature. We assume the thermal gas to be in equilibrium with the cluster potential. This is also referred to as virial temperature:

$$\frac{3}{2}k_{\mathrm{B}}T_{200} = \bar{m}\frac{M_{200}G}{R_{200}}, \tag{7}$$

where k_B is the Boltzmann constant and $\bar{m} = \mu m_{\mathrm{p}}$ is the mean particle mass. Here, $\mu \approx 0.588$ is the mean molecular weight (see e.g. Pfrommer 2022) and m_{p} is the proton mass. With $R_{200} = 2\mathrm{Mpc}$ and $M_{200} = 10^{15}\mathrm{M}_{\odot}$, this yields virial temperatures of $T_{200} \approx 10^8$ K. The R_{200} radius is also referred to as virial radius, the radius, up to which we can apply the virial theorem.

2.1.3 Cosmological Simulation

How do we perform a cosmological simulation? We assume that the universe can initially be described as weakly magnetised gas and dark matter. These interact gravitationally. The hydrodynamical interactions can be described with magnetohydrodynamics (MHD). We use AREPO (Springel, 2010) to solve the gravitational and hydrodynamical equations. We use the subgrid model for galaxy formation FABLE (Henden et al., 2018) to simulate radiative physics. How does the magnetic field look like in this cluster? How does including radiative physics influence the evolution of the magnetic field? We run 2 different simulation setups to answer these questions. One, where we use gravity, MHD and include radiative physics. In the other setup, we only use MHD and gravity.

In figure 3, we show the simulated cluster that we analyse in this thesis. The cluster has been re-simulated from a cosmological simulation, using the zoom-in technique. The figure shows a proxy for the optical spectrum. At $z = 0$, it contains 8795 galaxies within the virial radius. The size is $R_{200} = 2968.495\mathrm{kpc}$ and the mass $M_{200} = 2.76 \cdot 10^{15}\mathrm{M}_{\odot}$. Equation (7) yields a virial temperature of $1.9{\cdot}10^8\mathrm{K}$. This cluster is the fifth most massive one in the simulation.

Figure 5 shows our cosmological box at $z = 0$. We see the density of the gas forming the cosmological web. The isotropy and homogenity of the simulated cosmos is shown beautifully. The black frame shows one of the halos that we postselected from this box. We run a cosmological simulation with a boxsize of one comoving Gpc/h. Comoving means that the box is expanding with the expansion of the universe. We run the simulation from $z = 127$ to $z = 0$. The initial size of the box is thus a factor of 128 smaller than at $z = 0$ (see equation 1). We save all properties of the simulation in a snapshot in a non-linear redshift spacing. In total, there are 248 snapshots in this redshift range. In figure 4, we show the redshift range of the snapshots and the corresponding age of the Universe.

We use the moving mesh code AREPO (Springel, 2010) to solve the hydrodynamical and gravitational equations. The mesh consists of unstructured voronoi cells. These represent the finite volume discretization of our fluid. It is a quasi lagrangian code, such that the cells are moving together with the movement of the fluid. We let the mesh expand together with the expansion of the universe. We calculate the redshift dependent Hubble parameter (equation 2) to calculate the expansion rate. We use the parameters from Planck measurements (Aghanim et al., 2020), $\Omega_{\Lambda} = 0.684$ and $\Omega_{\mathrm{m0}} = 0.316$, where $\Omega_{\mathrm{b0}} = 0.049$. The Hubble parameter is $h = 0.673$.

What are our initial conditions at the first snapshot? We use the CAMB code to generate an initial power spectrum (Lewis & Bridle, 2002; Lewis et al., 2000) and the NGENIC code to set up a N-body implementation of Gaussian random fields prescribed with the

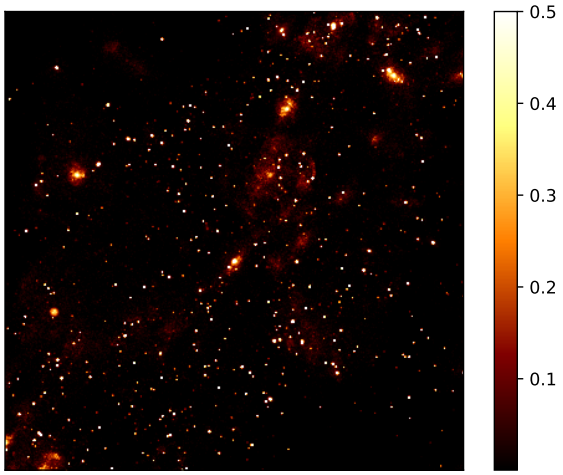

Figure 3: Halo4: A projection of the fifth most massive galaxy cluster from our cosmological simulation. The image has sidelengths of $4 \cdot R_{200}(z = 0)$, where $R_{200}(z = 0) = 2969\text{kpc})^3$, and a similar projection depth. This cluster is going to be analysed in this thesis. Indicated in red, we show the projected masses of the star particles. The colors correspond to $10^{10} M_\odot/h$, weighted within the projection depth. The image shows thousands of galaxies at different sizes.

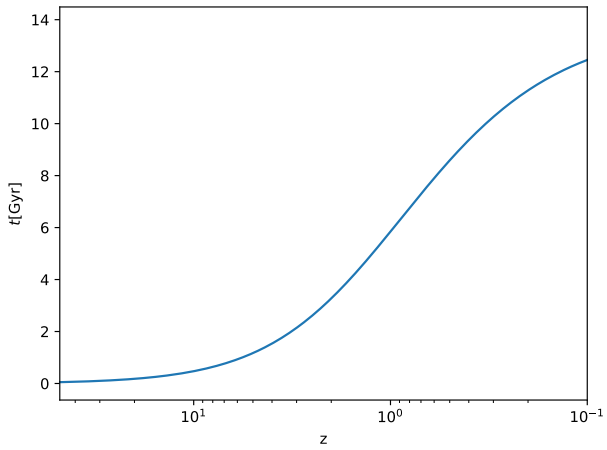

Figure 4: Our snapshots cover this redshift range. The corresponding age of the Universe is indicated on the x-axis.

power spectrum (e.g. as described in Springel et al. 2005; Angulo et al. 2012). At the beginning of the simulation, we place the dark matter particles accordingly. We run the parent simulation with 1024^3 particles and a mass resolution of $1.0 \times 10^{11} \text{M}_\odot$ per particle. We evolve the cosmological box until $z = 0$. We pick the most massive halos at $z = 0$ using a Friend of Friends algorithm (FoF) (Springel et al., 2001) and rerun the simulation with a higher mass resolution in this region (zoom-in technique). Every particle that ends up in the halo is attributed with a higher resolution. We use three different resolutions: zoom4, zoom8 and zoom12. In this thesis, we focus on the highest resolution run, zoom12. For the zoom12 high resolution simulation, we have 7.5×10^8 dark matter particles, each with a mass of $3.99 \times 10^7 \text{M}_\odot$. The high resolution particles are distributed within a radius

of three times R_{200}. Between this region of high resolution inside the halo and lower resolution outside, we use a third dark matter particle type with an intermediate mass to smooth the transition between both regions. Each high resolution particle creates a gas cell with the same mass. The code refines by splitting or merging cells so that every cell contains approximately the same gas mass. Cells with higher densities split automatically in order to fulfill this mass criterion. This automatically enables a higher resolution in the high density regions. The gravitational interactions are solved by AREPO. It uses a TreePM code (e.g. as introduced in Springel 2005), which splits gravitational forces into long- and short-range forces. The long-range force is calculated using a Fourier transform on a mesh. The short-term contribution is solved with an oct-tree algorithm (J. Barnes & Hut, 1986).

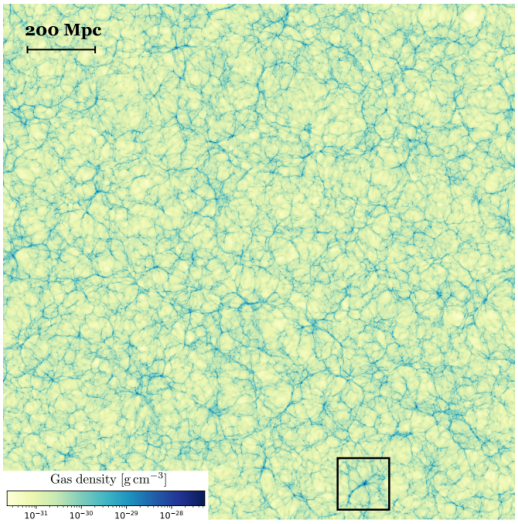

Figure 5: A projection of our simulation box at $z = 0$ with sidelengths of 1 Gpc/h and a projection depth of 10Mpc/h. The image shows the cosmic web. Blue colors indicate dense regions, while light colors indicate underdense regions. The black square shows a cluster that we select in a post processing step. Credits: Thomas Berlok

2.2 The Intracluster Medium

Most of the baryonic matter in galaxy clusters is in the form of X-ray emitting, hot $10^7 - 10^8$K gas (Walker & Nagai, 2019; Rudnick, 2019), which we refer to as Intracluster Medium (ICM). Due to the high temperatures, most particles are ionized. Thus, the magnetic field is embedded into this gas. The magnetic field evolution is strongly dependent on the dynamics in the ICM and vice versa. This section gives an overview on how to describe the fluid dynamical processes in galaxy clusters. We focus on the properties density and turbulence. These can both influence the evolution of the magnetic field.

2.2.1 Observations

How do we know that galaxy clusters are filled with hot gas? This was revealed by the first X-ray missions that were launched in the 70's (Gunn & Gott, 1972; Sarazin, 1986). They found that galaxy clusters are among the brightest X-ray sources in the sky (Snowden et al., 2008; Walker & Nagai, 2019; Sarkar et al., 2022). The X-ray emission is created by Bremsstrahlung (Cavaliere & Fusco-Femiano, 1976; Sarazin, 1986). Here, electrons get deflected in the electric field of ions and emit photons. The X-ray emission is proportional to the ion and electron densities in the gas and also depends on temperature. The ICM makes up most of the baryonic matter and roughly 7% of the total matter (see e.g. Pfrommer 2022). Figure 6 shows the Perseus cluster. The right panel shows an optical image. The BCG is shown with its neutral hydrogen content in blue and red. The left panel shows an X-ray image of the same cluster. It shows, how the space between the galaxies is filled with X-ray emitting plasma. The left panel shows how the gas density is very dense in the center and then declines steeply towards the outskirts. The plasma nature of the ICM tightly couples the magnetic field to its density.

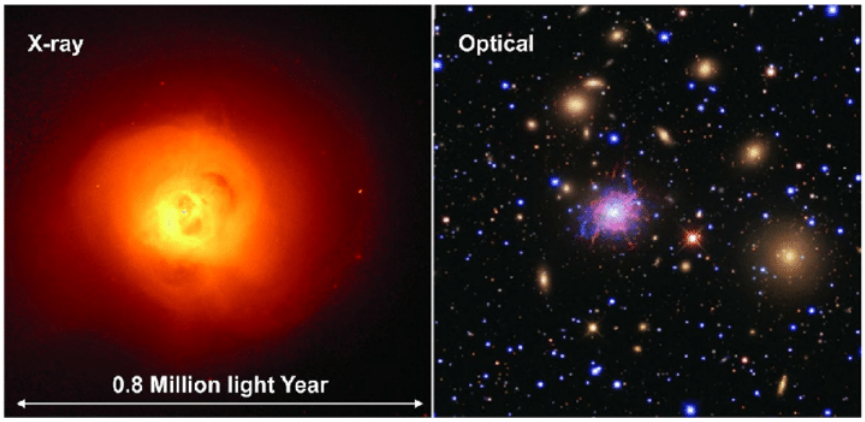

Figure 6: The Perseus cluster shown in the X-rays and optical. The X-ray image traces the gas in the cluster. It is denser in the center and declining towards the outskirts. Two cavities near the center show the effects of AGN feedback that dilutes the gas. The optical image shows the stars and galaxies in the cluster. The most massive galaxy is overlayed with $H\alpha$ observations, indicating the cold gas reservoir. Image credits: Fabian et al. (2011), Gabany (2009).

The X-ray image shows two cavities near the center with a lower density. These are caused by the central AGN that injects energy into the gas and dilutes it. Feedback by the AGN causes turbulence in the central regions. Also structure formation processes add a high amount of turbulence to the ICM. Not only plasma densities influence the magnetic field, but also turbulence (as we will show in section 2.3). Turbulence can be detected via

Doppler broadening of emission lines, but this requires a high spectral resolution (Rudnick, 2019). This is the reason that the origin and effects of turbulence in the ICM are still poorly understood (Rudnick, 2019). An X-ray mission that observed turbulence in the Perseus cluster center, was the HITOMI X-ray satellite. It observed the center of the Perseus cluster (higher densities give rise to a higher amount of X-ray emission), where the turbulence is mainly associated to AGN activity (Hitomi Collaboration, 2016; Zhang, Zhuravleva, et al., 2022). Turbulent kinetic energy can be converted into magnetic energy. The theory is described by the turbulent small scale dynamo in section 2.3.3. Thus, it is important to understand the properties and the dynamical state of the ICM.

2.2.2 Thermodynamical Considerations

What kind of analytical assumptions can we make about the ICM? We describe the ICM as a fluid. A system can be described as fluid, if the particle mean free path is smaller than the characteristic size of the system (so a few Mpc for a galaxy cluster): $\lambda_{\mathrm{mfp}} \ll L$ (Kunz et al., 2022). This requirement ensures the occurrence of particle scatterings that are characteristic for a fluid. We describe the particle mean free path as (e.g. as described in Pfrommer 2022)

$$\lambda_{\mathrm{mfp}} = \frac{1}{n\sigma \ln \Lambda} = \frac{1}{n\pi r_{\mathrm{e}}^2 \ln \Lambda}. \tag{8}$$

We assume that the particle mean free path is dominated by large angle electron scatterings. Here, $n = \rho/\bar{m}$ is the particle number density. The $\sigma = r_{\mathrm{e}}\pi$ term is the Coulomb scattering cross section and r_{e} the classical electron radius. The $\Lambda = r_{\mathrm{e}}/\lambda_{\mathrm{D}}$ term is the Coulomb logarithm $\ln \Lambda \sim 35 - 40$. It takes into account, that we are dealing with a plasma, which is neutral on large scales, but not within the Debye length λ_{D}. The Debye length reads (Block, 1978):

$$\lambda_D = \sqrt{\frac{k_{\mathrm{B}} T}{4\pi e^2 Z}}, \tag{9}$$

where Z is the charge number of the ion species ($Z = 1$ for hydrogen). The Coloumb logarithm enlarges the scattering cross section, taking also long range electromagnetic wave interactions into account. Equation (8) yields values of 0.1 kpc in the center and 10 kpc in the outskirts (Kunz et al., 2022). Though particle-particle collisions are very rare, due to the low densities in the ICM, electromagnetic wave-particle scatterings can actively act as collisions to justify the fluid treatment (see e.g. Pfrommer 2022).

We can describe the processes in a fluid as adiabatic, if the process induces no change in entropy. In terms of the first law of thermodynamics, this reads:

$$dq = 0 = Tds = d\epsilon + PdV, \tag{10}$$

where q is the internal specific heat, s is the specific entropy, ϵ is the specific internal energy, P is the pressure and V the volume.

A common approach to describe the state variables of the ICM is to use an effective equation of state (Hernquist & Springel, 2003; Vogelsberger et al., 2013):

$$\epsilon = \frac{P}{(\gamma - 1)\,\rho}. \tag{11}$$

With equation (11), we state that the state of the ICM can be described by pressure and density $\rho = \bar{m}/V$ only. The adiabatic index is $\gamma = c_V/c_P = 5/3$, the ratio of heat capacity at constant volume and pressure, respectively, for non-relativistic particles.

2.2.3 Density Profiles

Why are density profiles of the ICM important? The density in the ICM is tightly coupled to the magnetic field. The Alfvénic flux freezing theorem states that the magnetic field is flux frozen into the plasma and depends on its density (Mouschovias, 1976; Field & Carroll, 2000).

The density profile is mainly dominated by gravity, cooling and heating. How can we describe the cooling of the ICM? Cooling is efficient, where the particle number density $n = \rho/\mu$ is high. The cooling time of a gas cloud can be calculated with (Sarkar et al., 2022):

$$t_{\text{cool}} = \frac{5nk_{\text{B}}T}{2n^2\Lambda_{\text{cool}}(T)}. \tag{12}$$

Here, $\Lambda_{\text{cool}}(T)$ is the cooling function. It is dependent on the element abundances in the gas as well as on the processes that cause the cooling. Thus, the cooling is very efficient in the centers of galaxy clusters, where the densities are high.

Galaxy clusters can be split into two groups, based on the plasma temperatures in the center. The clusters, represented by a cooler core ($T \sim 2$keV) are referred to as Cool Core (CC) clusters. While the clusters with an ehanced central temperature profile belong to the group of non-Cool Core (nCC) clusters (Chen et al., 2007; Hudson et al., 2010). What exactly causes this bimodal distribution, is area of active research (Planelles et al., 2014; Biffi et al., 2016; Giacintucci et al., 2017; D. J. Barnes et al., 2018; Ruppin et al., 2021). Simulations suggest that the interplay of cooling, AGN heating and gravity influence the central profiles (Nobels et al., 2022; Ruppin et al., 2022).

How can we describe the density profiles in galaxy clusters? Density profiles are commonly inferred from X-ray observations. X-ray observations show high densities in the center and an exponential decline towards the outskirts. A so called beta profile is commonly used to describe the ICM density profile. Here $\beta = \bar{m}\sigma_{gal}^2/k_BT$ (Aghanim et al., 1997; Pfrommer, 2022) is the ratio of specific kinetic energy of a galaxy and the internal gas energy (not to be confused with the plasma β, which is the ratio of thermal and magnetic pressure). The β parameter varies with distance from the center. We define a central density profile and a profile beyond a scaling radius (Churazov et al., 2003; Pfrommer, 2022):

$$\rho(r) = \rho_{0,1}\left[1 + \left(\frac{r}{r_{0,1}}\right)^2\right]^{-3\beta_1/2} + \rho_{0,2}\left[1 + \left(\frac{r}{r_{0,2}}\right)^2\right]^{-3\beta_2/2}. \tag{13}$$

X-ray measurements are usually used to constrain the parameters. The densities $\rho_{0,1}$ and $\rho_{0,2}$ are asymptotically approached at radius $r_{0,1}$ and $r_{0,2}$, respectively. We differentiate between a single beta profile ($\rho_{0,2} = 0$) and a double beta profile ($\rho_{0,2} \neq 0$). The single beta profile is characterised by a flat distribution in the central region $r < r_{0,1}$. It is used to describe nCC clusters. For $r > r_{0,1}$, it drops with a power law. The double beta profile is characterised by an enhanced density in the center. We use it to describe the class of CC

clusters. Beyond R_{200}, both density profiles approach the mean baryonic matter density of the universe.

The magnetic field is flux frozen into the plasma. An easy way to amplify magnetic fields (or decrease) is therefore by adiabatic compression (or expansion) (Winske & Quest, 1988; Martin-Alvarez et al., 2022). Consider the mass inside a sphere and the magnetic flux through it staying constant (e.g. Pfrommer 2022):

$$\rho r^3 \frac{4}{3}\pi = \text{const.} \Leftrightarrow \rho \propto r^{-3} \tag{14}$$

and

$$\Phi = B 4\pi r^2 = \text{const.} \Leftrightarrow B \propto r^{-2}, \tag{15}$$

so that

$$B \propto \rho^{2/3}. \tag{16}$$

Such simple, spherically symmetric density profiles are in general to be treated carefully, as they do not account for the unique history of each cluster. Turbulence, feedback processes and cooling can modify the inner density profiles (Wittor et al., 2017). Merger, structure formation processes, and cooling of gas clumps are what mostly influences deviations in the outer regions (Bennett & Sijacki, 2022; Gaspari & Churazov, 2013). Accounting for more baryonic effects, these models can easily get more and more complicated (see for example Vikhlinin 2019; Halenka & Miller 2020 who use more advanced gas density profiles). Here, we are essentially interested in when the cluster deviates from such self similar approaches. Deviations are associated to turbulence, which gives rise to the turbulent dynamo. In the next section, we will introduce how to describe turbulence in the ICM.

2.2.4 Turbulence, Vorticity and Enstrophy

The other way to influence the magnetic field evolution goes via turbulence. What exactly is turbulence? How is turbulence connected to the magnetic field? Turbulent kinetic energy can be converted into magnetic energy. The underlying theory is described with the turbulent small scale dynamo. In a turbulent medium, it is able to amplify small magnetic seed fields. The velocity field in the ICM is highly turbulent (Wittor et al., 2017; Vazza et al., 2017; Wittor & Gaspari, 2020). In this subsection, we give the basics of hydrodynamic turbulence, which is a prerequisite for the turbulent dynamo discussion in section 2.3.3. Note that turbulence in the ICM is in fact plasma turbulence, which complicates the picture (see e.g. Schekochihin 2022 for a review).

Turbulence is, for example injected in shocks. What is a shock? At this point, it is useful to define the Mach number (Pfrommer et al., 2006):

$$\mathcal{M} = \frac{v}{c_s}. \tag{17}$$

It relates the speed of an object (or a fluid parcel) to the speed of sound $c_\mathrm{s} = \sqrt{\gamma P/\rho}$ in the surrounding medium. When $\mathcal{M} > 1$, the fluid cannot properly communicate changes in states anymore. If an object or fluid parcel is moving at this speed, it inforces jumps

in the state of the fluid. This is referred to as a shock. Shocks convert kinetic energy into heat and can add subsonic turbulence to the ICM (Price, 2012). In galaxy clusters, shocks can be caused by accretion or mergers (Ensslin et al., 1998; Markevitch & Vikhlinin, 2007), AGN (Wittor & Gaspari, 2020) or supernovae (SN) (Spitzer, 1978; Woosley & Weaver, 1995).

Turbulence can be described as random, heuristically chaotic motions in a fluid. In general, we can decompose any vector field into a compressible and a solenoidal part (Helmholtz, 1858). In the ICM, most of the turbulence is in solenoidal form (Gaspari & Churazov, 2013; Vazza et al., 2017). We refer to a rotating fluid parcel as a vortex or an eddy. In general, anything can be described as vorticity, where the motion is incompressible: $\boldsymbol{\nabla} \cdot \mathbf{v} = 0$. Vorticity is $\boldsymbol{\omega} = \boldsymbol{\nabla} \times \mathbf{v}$. We refer to vorticity as the the eddy turn over rate (Pfrommer, 2022):

$$|\boldsymbol{\omega}_\lambda| = \frac{\mathrm{v}_\lambda}{\lambda}. \tag{18}$$

Here, λ is the eddy size and v_λ the eddy velocity. Equation (18) shows, that higher vorticity is caused by smaller eddies or higher velocities. Kinetic energy is injected on large scales (for example by a merger). Large scale eddies cascade down to smaller eddies until viscous effects set in and turn the kinetic energy into thermal energy. In the presence of a magnetic field, the kinetic energy is also converted into magnetic energy. We describe the specific kinetic energy within an eddy with

$$\epsilon_\lambda = \frac{\mathrm{v}_\lambda^2}{2}. \tag{19}$$

The cascade from large scales to small scales is described by the Kolmogorov spectrum (Kolmogorov, 1941; Gaspari & Churazov, 2013) in wavenumber k space:

$$E\left(k\right) \propto \dot{\epsilon}_\lambda^{2/3} k^{-5/3}, \tag{20}$$

where (Pfrommer, 2022)

$$\dot{\epsilon}_\lambda = \frac{\mathrm{v}_\lambda^2}{2} \frac{\mathrm{v}_\lambda}{\lambda} = \frac{\mathrm{v}_\lambda^3}{2\lambda} \tag{21}$$

is the constant energy flux from scale to scale through an eddy. It corresponds to dividing the specific kinetic eddy energy by the eddy turnover time. In equation (20), $1/k = \lambda$ is the size of an eddy and reaches from the large injection scales to the small viscous scales. The larger eddies contain more power, compared to the smaller eddies, but the smaller eddies have a higher vorticity. The vorticity evolution with time reads (see e.g. Wittor et al. 2017):

$$\frac{\partial \boldsymbol{\omega}}{\partial t} = \boldsymbol{\nabla} \times (\mathbf{v} \times \boldsymbol{\omega}) + \frac{\boldsymbol{\nabla}\rho \times \boldsymbol{\nabla} P}{\rho^2}. \tag{22}$$

What influences vorticity in (22), is a first term, which describes how vorticity can be advected or produced in compression and stretching, and a baroclinic term. The baroclinic term describes, how misaligned gradients of density and pressure (or equivalently temperature) will create vorticity. This happens, for example, in bow shocks, where

vorticity is transported along sideways of the shock.

In a fluid with no viscosity and no baroclinic term, the vorticity is frozen into the fluid in the same way that the magnetic field is. The energy flow through the eddies stays constant: (21) = const.. The eddies are dissolved, when they reach a size that equals the particle mean free path. Viscous effects set in and turn the kinetic energy into heat.

We would like to have a measure of the amount of turbulence in a (simulated) galaxy cluster. Since the vorticity is a vector field, a simple sum will have contributions cancelling out. It is useful to define a quantity called enstrophy (see e.g. Wittor et al. 2017):

$$e = \frac{1}{2}|\boldsymbol{\omega}|^2. \tag{23}$$

Enstrophy is also injected in shocks or mergers (or any baroclinic motion). It is a proxy for turbulence.

In order to quantise the level of turbulence in a fluid, we define an advection time $t_{\mathrm{adv}} = \lambda/\mathrm{v}_\lambda$ and a dissipation time $t_{\mathrm{diss}} = \lambda^2/\nu$. Here, $\nu = \lambda_{\mathrm{mfp}}\mathrm{v}$ is the viscosity. Their ratio defines the Reynolds Number (Pfrommer, 2022; Nishikawa & Liu, 2018):

$$\mathrm{Re} = \frac{t_{\mathrm{diss}}}{t_{\mathrm{adv}}}. \tag{24}$$

It is is a number to characterise whether the fluid is susceptible to turbulence. A high number means the fluid is dominated by advection and that the flow is turbulent. A low number means it is dominated by dissipation and that the flow is laminar.

2.2.5 Simulating the ICM

How can we simulate the ICM and use the MHD module in AREPO (Springel, 2010; Pakmor et al., 2011) to solve the magnetohydrodynamical (MHD) equations? A voronoi cell is created from each DM particle with the cell center coinciding with the DM particle position. We solve the MHD equations on this voronoi mesh. The magnetized fluid obeys mass, momentum and total energy (kinetic, internal and magnetic) conservation.

The MHD equations are solved on a moving grid using quasi Lagrangian finite volume method. In MHD, we assume a perfectly conducting (no resistivity and viscosity) fluid. In order to ensure no resistivity, we assume, that electrons move sufficiently fast, so that they can short circuit all electric fields ($\partial \boldsymbol{E}/\partial t = 0$) (see Pfrommer 2022). The absence of resistivity also causes the absence of magnetic diffusion (magnetic diffusion shows up due to numerical errors, so called numerical resistivity, as described in section 2.3.4). The MHD equations without gravity and cooling read (Pakmor et al., 2011)

$$\frac{\partial}{\partial t}\rho + \boldsymbol{\nabla}\cdot(\rho\mathbf{v}) = 0, \tag{25}$$

$$\frac{\partial(\rho\mathbf{v})}{\partial t} + \boldsymbol{\nabla}\cdot\left(\rho\mathbf{v}\mathbf{v}^{\mathrm{T}} + p - \boldsymbol{B}\boldsymbol{B}^{\mathrm{T}}\right) = 0, \tag{26}$$

$$\frac{\partial(E)}{\partial t} + \boldsymbol{\nabla}\cdot(E\mathbf{v} + p\mathbf{v} - \boldsymbol{B}(\mathbf{v}\cdot\boldsymbol{B})) = 0, \tag{27}$$

$$\frac{\partial \boldsymbol{B}}{\partial t} + \boldsymbol{\nabla} \cdot \left(\boldsymbol{B}\mathbf{v}^{\mathrm{T}} - \mathbf{v}\boldsymbol{B}^{\mathrm{T}} \right) = 0. \tag{28}$$

The magnetic pressure is added to the total pressure: $p = p_{\mathrm{gas}} + \mathbf{B}^2/2$ and the magnetic energy density is added to the total energy density: $E = \rho u + \rho \mathbf{v}^2/2 + \mathbf{B}^2/2$, where $\mathbf{v}$ is the velocity of the fluid. Equation (25) is the mass continuity equation. It states that mass is conserved. Equation (26) is the momentum conservation equation. The momentum density changes due to a movement of the fluid, pressure that acts on the fluid or the magnetic field that adds the Lorentz force $\mathbf{F_L} = e(\mathbf{E} + \frac{\mathbf{v_e}}{\mathbf{c}} \times \mathbf{B})$ onto the fluid. Equation (27) is the energy conservation equation. The energy density changes due to spatially varying density, momentum or magnetic field. Equation (28) is the magnetic induction equation. The magnetic field changes due to a rotation of the magnetic field. The MHD equations are subject to the no-magnetic-monopoles constraint: $\boldsymbol{\nabla} \cdot \mathbf{B} = 0$.

It is possible to combine equations (25) and (28) to see that the magnetic field is frozen onto the motion of the fluid (Alfvén flux freezing theorem) in the absence of magnetic diffusion. The flux-freezing strongly couples the magnetic field evolution to the fluid movement.

How does AREPO solve equations (25) - (28)? The MHD equations obey the form of a conservation equation (Springel, 2021):

$$\frac{\partial \mathbf{U}}{\partial t} + \boldsymbol{\nabla} \cdot \mathbf{F}(\mathbf{U}) = 0. \tag{29}$$

A finite volume discretisation is used, where the equations are evolved in time. Within a timestep, the conservation laws are integrated and the average over the cell is taken, yielding the exact solution between the cell interfaces. The timesteps are chosen, such that the fluid cannot traverse a cell within a timestep (that is the CLF timestep criterion, see e.g. Springel 2021):

$$t < \Delta x / c_{\mathrm{max}} \tag{30}$$

where c_{max} is the maximum wave speed and Δx the one dimensional size of a cell. Between the cell interfaces, there is an exact Riemann solution, representing the flux from one cell to another one. We use a HLLD Riemann solver, which is an approximate solver. Exact Riemann solvers are rarely used in real applications. AREPO uses a second order Gudunov unsplit scheme to calculate the eigenstructure within the cell and also the upwind direction. Unsplit means, that the fluxes into different 3D directions are calculated separately, but simultaneously applied to the cell. Second order, because we consider a linear gradient over the cell. For the Riemann solver, it is assumed that the values at the interfaces are constant. To enable this, the flux calculation has to be done within half a timestep and is then extrapolated to the cell interfaces. A slope limiting function is added, otherwise local extrema could cause the extrapolated interface values to overshoot. Each mesh generating point gets a velocity assigned. The timestep has to be modified from the hydrodynamical consideration (30) to account for faster MHD waves:

$$\Delta t < C_{\mathrm{CFL}} \frac{\Delta x}{c_{\mathrm{h}}}, \tag{31}$$

where C_{CFL} is the timestep coefficient from only hydrodynamics and Δx the size of a cell and c_{h} the speed of the fastest MHD wave. Using the Riemann solver in the rest frame of

the mesh generating points would give only small fluxes, as the points move almost with the same velocity as the flow. This could in the approximation lead to negative fluxes. Instead, the MHD equations are solved in the rest frame of the interfaces. We have to subtract the velocity of the flow by the velocity of the interfaces: $\mathbf{w} = \mathbf{v_{fluid}} - \mathbf{v_{interface}}$. Then we transform from the interface restframe to the mesh points restframe by adding $\frac{\partial \mathbf{U}}{\partial t} + \boldsymbol{\nabla} \cdot \mathbf{F}(\mathbf{U}) + V(\mathbf{U}) = 0$ (Pakmor et al., 2011):

$$V(\mathbf{U}) = \begin{Bmatrix} 0 \\ \rho \mathbf{w} (\mathbf{v} - \mathbf{w})^{\mathrm{T}} \\ \rho (\mathbf{v} \cdot \mathbf{w})(\mathbf{v} - \mathbf{w}) - \rho/2 \mathbf{w}^2 (\mathbf{v} - \mathbf{w}) + p\mathbf{w} - \mathbf{B}(\mathbf{w} \cdot \mathbf{B}) \\ -\mathbf{w}\mathbf{B}^{\mathrm{T}} \end{Bmatrix}. \tag{32}$$

The volume and time discretization approach introduces numerical errors that have the form of magnetic divergence $\nabla \cdot \mathbf{B}$ acting as source term:

$$\frac{\partial \mathbf{U}}{\partial t} + \nabla \cdot \mathbf{F}(\mathbf{U}) = \mathbf{S}, \tag{33}$$

but there are no magnetic monopoles, so we require $\nabla \cdot \mathbf{B} = 0$. These divergence errors grow exponentially in time. In order to remedy this, we use the Powell 8 divergence control scheme Powell et al. (1999) that adds additional terms to reduce the error:

$$\frac{\partial \mathbf{U}}{\partial t} + \boldsymbol{\nabla} \cdot \mathbf{F}(\mathbf{U}) + \mathbf{G}(\mathbf{U}) = \mathbf{S}_{\mathrm{small}}. \tag{34}$$

What is done basically is that we calculate equations with the divergence error, but then subtract the error from the initial state. This reduces the error and ensures stability.

The grid is moving with the expansion of the universe; all MHD quanities are calculated in comoving form. Here we have described the ideal MHD equations in their standard form. In our simulations, we actually solve these equations in a form that takes into account (Pakmor & Springel, 2013):

$$\mathbf{r} = a\mathbf{x} \tag{35}$$

$$\mathbf{u} = \mathbf{v} - a\dot{\mathbf{x}} \tag{36}$$

$$\rho = \rho_{\mathrm{c}} a^{-3} \tag{37}$$

$$P = P_{\mathrm{c}} a^{-3} \tag{38}$$

$$\mathbf{B} = \mathbf{B}_{\mathrm{c}} a^{-2}. \tag{39}$$

Check out the appendix for a more detailed description on the conversion: Berlok (2022).

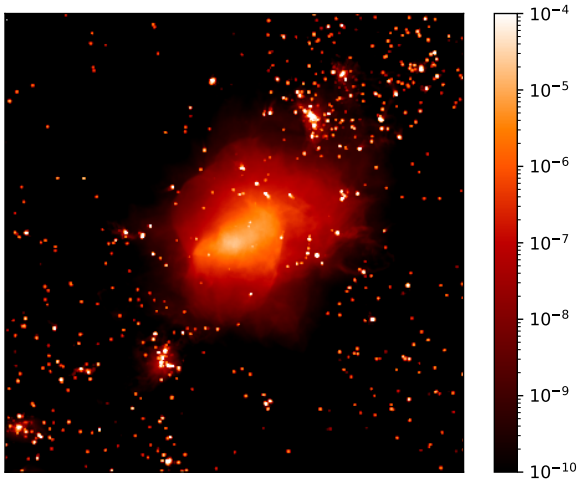

Figure 7: A projection of halo4 with sidelengths of $R_{200} = 2969$kpc at $z = 0$ and a similar projection depth. Red indicates a proxy for X-ray emission, which we calculate as $L \propto \rho^2\sqrt{T}$. The galaxies shine bright in X-rays, because the gas cannot form neutral hydrogen. The colorscheme indicates the values of L in comoving code units, weighted within the projection depth.

Figure 7 shows a proxy for the X-ray emission of the ICM of our simulated cluster. The figure shows how higher densities in the center enable a more efficient cooling and brighter X-ray luminosity. The bright spots (that don't show up in the X-ray observation of the Perseus cluster in figure 6) show up as a result of our one phase ICM. Once, the gas reaches a certain density threshold, the cooling is so efficient that electrons and protons recombine to form neutral hydrogen. Neutral hydrogen does not emit Bremsstrahlung. Instead in the simulation, we do not form neutral hydrogen. Galaxies are shining bright in X-rays thus, instead of being invisible in neutral hydrogen.

2.3 Magnetic Fields

The goal of this thesis is to study the generation of magnetic fields in simulations of the ICM of galaxy clusters. This is important to check if we can match the field values inferred from observations, but it is further motivated by the effect magnetic fields can have on other astrophysical processes. Magnetic fields are for instance important for the acceleration, transport and cooling of cosmic rays (H. Xu, 2009). They can influence the evolution of galaxies within the cluster, for example by magnetic draping (Sparre et al., 2019). They cause anisotropic particle movement, which is important to understand the properties of the ICM. In this subsection, we describe how magnetic fields can be created with astrophysical batteries. We also describe how magnetic fields can be amplified with the turbulent small-scale dynamo.

2.3.1 Observations

How do we know that galaxy clusters host magnetic fields? Their existence was first proven by radio observations (van Weeren et al., 2009) and later by the Faraday rotation measure (Taylor et al., 2001; van Weeren et al., 2019; Osinga et al., 2022). These observations revealed that galaxy clusters are filled with magnetic fields of a few μG strength. They have coherence lengths at the order of a few kpc (Subramanian, 2008).

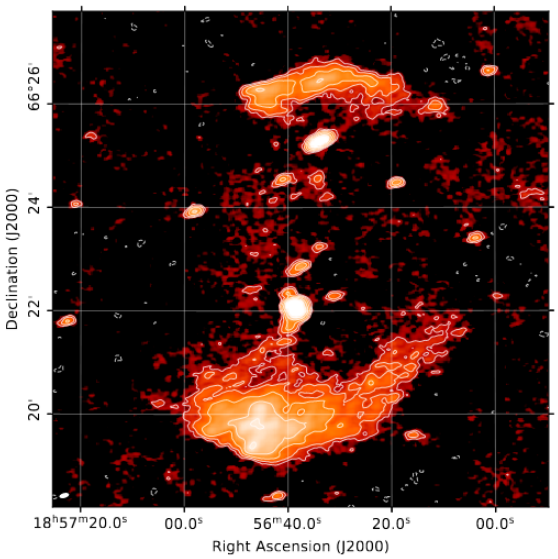

Figure 8: The galaxy cluster PSZ2 G096.88+24.18 shown in the radio wavelengths. Radio observations of clusters trace their magnetic field. The arc shaped features are so called radio relics. They sit at the outskirts of the cluster. They are associated to accretion or merger shocks. The light bubbles further inside are aged AGN bubbles. The articles in the bubbles are reaccelerated by the shock and emit radio emission. Credits: Jones et al. 2021

As an example, we show in figure 8 a radio image of a galaxy cluster. The radio emission is created by relativistically moving, charged particles, which get deflected by magnetic field lines. This is known as synchrotron emission. Regions with orange colors indicate a high radio emission. The emission regions sit as arc shaped areas at the outskirts of the cluster. These are called radio relics and they sit at Mpc scales (H. Xu, 2009; Brunetti & Jones, 2014; van Weeren et al., 2019). The particles are thought to be accelerated at shocks that can be caused by merger or accretion (Brunetti & Jones, 2014; van Weeren et al., 2019). The light radio bubbles closer to the center are spatially correlated to galaxies

in the cluster. These are thought to be aged AGN bubbles. The accretion shock runs over the bubbles and reaccelerates the particles.

We can calculate the magnetic field strength from radio observations. We do this by assuming equipartition of the particle (electrons and protons) kinetic energy and magnetic energy (H. Xu, 2009):

$$E_{\mathrm{tot}} = E_{\mathrm{kin,e}} + E_{\mathrm{kin,P}} + E_{\mathrm{B}}, \tag{40}$$

where the magnetic energy is

$$E_{\mathrm{B}} = B^2 V. \tag{41}$$

Here, B is the magnetic field strength and V is the volume that is occupied by the magnetic field. In equation (40), we assume that the electron kinetic energy is equivalent to a fraction of the protons kinetic energy: $E_{\mathrm{kin,P}} = aE_{\mathrm{kin,e}}$. These values for the kinetic energy depend on the injection mechanism, which comes with big uncertainties (H. Xu, 2009).

The radio measurements can be complemented by X-ray measurements. We assume, that the same particles that create the radio emission also undergo inverse Compton (IC) scattering with CMB photons. Here, the hot, relativistically moving electrons in the ICM collide with CMB photons and upscatter them to higher energies. This enables us to relate the fluxes of IC scattered CMB photons, F_{IC} to the synchrotron photons, F_{S}. We do this by dividing the CMB energy density, U_{CMB} by the magnetic field energy density (Beck & Krause, 2005; Akamatsu et al., 2013):

$$\frac{F_{\mathrm{IC}}}{F_{\mathrm{S}}} = \frac{U_{\mathrm{CMB}}}{B^2}. \tag{42}$$

Another way of measuring magnetic fields uses the so called Faraday rotation measure (van Weeren et al., 2019; Osinga et al., 2022). The effect describes, how the plane of polarization of linearly polarized light rotates when traveling through a magnetized medium. This is due to a different refractive index for left and right handed circularly polarized light (Kunz et al., 2022). The rotation measure is given by:

$$\mathrm{RM} \propto \int n_{\mathrm{e}}(l) \cdot B(l) dl, \tag{43}$$

where $B(l)$ is the line of sight component of the magnetic field. In order to get the electron line of sight density $n_{\mathrm{e}}(l)$, the measurement needs to be combined with X-ray measurements (Clarke et al., 2001). Rotation measurements yield magnetic fields of few μG (3.9-5.4 μG in the coma cluster Kunz et al. 2022).

2.3.2 Magnetic Seed Fields

How is the magnetic field in the ICM created? The turbulent dynamo is able to amplify weak magnetic seed fields (see section 2.3.3). But where do these seed fields come from? The creation of seed fields is still under debate. There are two ideas being discussed: the generation from structure formation in the early Universe (Subramanian, 2008; Mtchedlidze et al., 2022), or via astrophysical batteries. Here, we focus on the creation from astrophysical

scenarios.

The best known approach to do astrophysical battery is the Biermann battery (Biermann, 1950; Kunz et al., 2022). It describes, how an inhomogeneity in the electron number density induces a current. If the induced electric field is spatially varying, this will create a magnetic field. The effect relies on the mass difference between electrons and protons. The ICM consists mostly of ionized particles. It is neutral on scales larger than the Debye length. This means, that there are in principle as many electrons as protons in a hydrogen plasma. Introducing a pressure gradient, the electrons move faster than the protons. This creates a pressure supported electric field. If this field is spatially varying, Faraday's law of induction $\boldsymbol{\nabla} \times \mathbf{E} = -c^{-1}\partial \mathbf{B}/\partial t$ allows to create a magnetic field.

In the following, we show how this works technically. The result is the Biermann battery equation. First, we look at the the electric field resulting from the charge separation. We do this by balancing the electric field force density onto an electron by its pressure support (Andreasyan, 1996):

$$\boldsymbol{E} = \frac{\boldsymbol{\nabla} P_\mathrm{e}}{e n_\mathrm{e}}. \tag{44}$$

We only consider the electrons, as they move faster than the protons by a factor of $\sqrt{m_\mathrm{p}/m_\mathrm{e}}$. We add this term (44) to the right hand side of Ohm's law with zero resistivity: $\boldsymbol{E} = -\mathbf{v}_\mathrm{e}/c \times \boldsymbol{B}$ and apply the curl to it. This allows us to insert it into Farady's law. We use the ideal gas law $P_\mathrm{e} = n_\mathrm{e} k_\mathrm{B} T_\mathrm{e}$ to rewrite the pressure in equation (44) in terms of density and temperature. We arrive at the Biermann battery equation (Kunz et al., 2022; Pfrommer, 2022):

$$\frac{\partial \boldsymbol{B}}{\partial t} = \boldsymbol{\nabla} \times (\mathbf{v}_\mathrm{e} \times \boldsymbol{B}) - \frac{c k_\mathrm{B}}{e} \frac{\boldsymbol{\nabla} n_\mathrm{e}}{n_\mathrm{e}} \times \boldsymbol{\nabla} T_\mathrm{e}. \tag{45}$$

The first term is similar to the term on the RHS in the induction equation (28) (only that here we only include electrons). It describes, how the magnetic field changes due to advection, compression and stretching. The second term is new. It is referred to as the baroclinic term. It describes the evolution of the magnetic field due to non-aligned gradients of electron number density and temperature. Starting with no initial magnetic field $\boldsymbol{B} = 0$, the baroclinic term can create magnetic fields.

Such a baroclinic term can be created within different scenarios. In ionization fronts, the electrons are more easily hit by the photons, because of the larger Thomson cross section (Gnedin et al., 2000). This can occur e.g. in quasars, supernovae or starburst galaxies (Miranda et al., 1998; Furlanetto & Loeb, 2001; Doi & Susa, 2011; Garaldi et al., 2021). Also, for example, bow shocks or structure formation shocks can create magnetic fields, using the Biermann battery effect (Kulsrud et al., 1997; Zhao et al., 2008; Mtchedlidze et al., 2021). This mechanism has been applied to various scenarios (Rees, 1987; Andreasyan, 1996). The created fields are at the order of $10^{-21} - 10^{-18}$G at the coherence length of a few kpc. Now we introduce three further mechanisms that are able to produce small magnetic seed fields.

Photoionization during reionization can create magnetic fields. It adds an additional electron charge separation (Gnedin et al., 2000; Durrive & Langer, 2015). This uses the same assumption as stated above for the Biermann battery equation (45). The effects

of photoionization add two additional terms. They account for the additional electron pressure and momentum gradients created by the ionizing photons. Both Gnedin et al. (2000) and Durrive & Langer (2015) find that the strength of the created fields is comparable to those created with the Biermann battery.

Schlickeiser & Shukla (2003), Bret et al. (2010), Bresci et al. (2022) and Kunz et al. (2022) suggest, that the Weibel instability could create a magnetic seed field at the order of $10^{-4}\mu$G (e.g. Kunz et al. 2022) on small scales. The Weibel instability is induced by a small transverse magnetic field perturbation. This can occur either due to counterstreaming flows or via temperature anisotropies. The Lorentz force will naturally sort particles with positive charge and negative charge, such as electrons and positrons, into counterstreaming current sheats. This amplifies the magnetic field perturbation and induces a magnetic instability. The remaining question is whether the generated small-scale field can be carried to larger scales (this is under active research, see e.g. Cagas et al. 2017; Zhang, Wu, et al. 2022).

Primodial magnetic fields from the early Universe are also potential candidates for seed magnetic fields. Discussed scenarios include vacuum electromagnetic field fluctuations that are stretched to large scales during inflation (Mtchedlidze et al., 2021, 2022) or seed field creation via phase transitions (Vachaspati, 1991; Subramanian, 2016). The phase transition results from quarks that are confined within hadrons. The free binding energy can be converted into magnetic energy (Grasso & Rubinstein, 2001). Both these approaches come with the problem that the expansion of the Universe will lower the magnetic field values. Therefore, initially very high seed field values are required.

There are different scenarios that are able to create initially weak seed fields. Commonly, it is assumed that, on cluster scales, seed fields are created by structure formation via means of the Biermann battery (Mtchedlidze et al., 2021). None of the above described mechanisms are able to create magnetic fields at the strength that is being observed on their own. We need to find mechanisms that are able to amplify weak magnetic fields.

2.3.3 The Turbulent Small-Scale Dynamo

Magnetic seed fields can be generated within different astrophysical scenarios, for example via means of the Biermann battery (45) (section 2.3.2). But how can those rather weak seed fields get amplified to the values of a few μG that we observe today? In this subsection, we describe how the magnetic field can get non-adiabatically amplified via the turbulent small-scale dynamo.

What is the turbulent small-scale dynamo? The ICM is turbulent. Feedback processes, as well as structure formation processes add energy mostly in kinetic or thermal form (at first) to the ICM (section 2.2.4). How can we convert these into magnetic energy? To see this, we compare the Biermann battery equation (45) to the vorticity evolution equation (22). Both come with a "convective" term that describes how the magnetic field/vorticity is frozen into the flux. Also the second terms look very similar: both describe a misalignment between the density and temperature gradients (or pressure, which can be rewritten as temperature, using the ideal gas law $P = nk_{\mathrm{B}}T$). The vorticity evolution is tightly coupled to the magnetic field evolution. This is a manifestation of the famous stretching, twisting, folding and merging of magnetic field lines (Asgari-Targhi & Berger, 2009). This process increases the magnetic field line density and thus the magnetic field strength, as shown in figure 9. Vorticity is the eddy velocity divided by its size (equation 18). Small eddies have a high vorticity. Thus, on the smallest scales, the stretching, twisting, folding and

merging of field lines works most efficiently. Together with this, also the magnetic field amplification works fastest on the smallest scales.

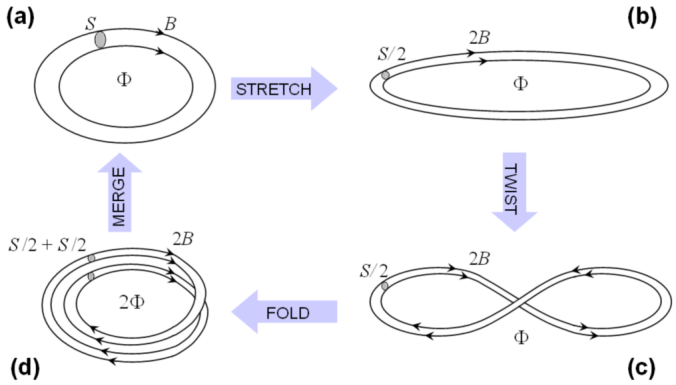

Figure 9: An illustration of the stretching, twisting, folding, merging of magnetic field lines. This process amplifies the magnetic field strength by increasing the field line number density. Credits: www.mpifr-bonn.mpg.de/3622111/lectures6-9.pdf.

How does the turbulent dynamo work? Figure 10 provides an illustration of the turbulent small-scale dynamo. Turbulence is injected in form of eddies at large scales. The eddies decay, accordingly to the Kolmogorov spectrum (equation 20). The vorticity is truncated at the viscous scales $l_{\mathrm{visc}} = k_{\mathrm{visc}}^{-1}$. The magnetic field though can dynamically evolve below these scales, if the resistivity is much smaller than the viscosity (which is he case in the ICM). In this case, the resistive scales lie below the viscous scales: $l_{\mathrm{res}} = k_{\mathrm{res}}^{-1}$. The magnetic field dynamics is truncated at the resistive scales. There, resistive diffusion prevents any further folding of the field lines. The resistive scales lie below the viscous scales: $l_{\mathrm{res}} \sim L\mathrm{Re}^{-1/4}\mathrm{Re}_{\mathrm{m}}^{-1/2} \sim l_{\mathrm{visc}}\mathrm{Pm}^{-1/2} << l_{\mathrm{visc}}$ for a plasma with a high magnetic Prandtl number (Kunz et al., 2022). We define the magnetic Reynolds number (similar to the "normal" Reynolds number in equation 55)(Pfrommer, 2022):

$$\mathrm{Re}_{\mathrm{m}} = \frac{\text{convection}}{\text{diffusion}} = \frac{\mathrm{v}B}{L} \cdot \left(\frac{DB}{L^2}\right)^{-1}. \tag{46}$$

Here, D is the magnetic diffusion coefficient. The diffusion coefficient is dependent on the electric resistivity η. The ICM is turbulent. The convective term dominates and the magnetic Reynolds number is high. The fluid is very conductive. The magnetic Prandtl number reads (Kunz et al., 2022):

$$\mathrm{Pm} = \frac{\mathrm{Re}_{\mathrm{m}}}{\mathrm{Re}} = \frac{\nu}{\eta}. \tag{47}$$

It sets viscosity ν and magnetic resistivity η into relation. The right panel of figure 10 shows how the magnetic field, on large scales, follows the rotational movement of the flow. On small scales, it inspirals further, where it is stretched over the subviscous scales. On the smallest scales that have the highest vorticity, the amplification works fastest and the magnetic field grows exponentially. Technically, this is described by a correlation function (Rincon, 2019). It correlates motion in the velocity field to motion in the magnetic field, but on smaller scales.

The amplification of the magnetic field on small scales is truncated at the resistive scales. This is due to resistive dissipation. The magnetic field cannot grow any further on small

scales. All small scale kinetic energy is used up. Looking at the Kolmogorov spectrum (20), indicated in figure 10, the larger scale eddies provide more power, though they have a smaller vorticity. Thus, the magnetic field keeps growing with the larger eddies, that provide more power, but on larger time scales. This phase is referred to as the non-linear regime.

This is described by Kazantsev theory (Kazantsev, 1968; Kraichman, 1966). We do not provide a mathematical description here, but instead refer to Subramanian (2008); Schober et al. (2013); Subramanian (2018); Rincon (2019); Kunz et al. (2022); Steinwandel et al. (2022). In contrast to the Kolmogorov spectrum scaling with $-5/3$, see equation (20), the Kazantsev spectrum reads (Kunz et al., 2022)

$$E(k) \propto k^{3/2}. \tag{48}$$

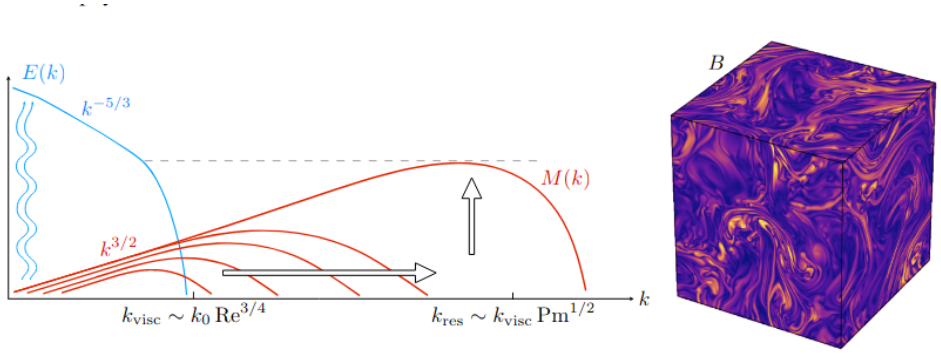

Figure 10: On the right: A MHD simulation of a three dimensional box. The magnetic energy is concentrated at the resistive scales, where Pm ~ 300. It shows nicely, how the magnetic field lines follow the large scale rotational movement, but then inspiral further on smaller scales. On the left: turbulence is injected with the Kolmogorov spectrum and truncated at the viscous scales. The magnetic field inspirals further until it reaches the resistive scales, where it is amplified fastest. Once, the magnetic field energy is in equipartition with the eddy energy at the viscous scales, the magnetic field keeps growing with the larger eddies, until their energies are in equipartition. This is referrred to as non-linear regime. It grows, accordingly to the Kazantsev spectrum Credits: (Kunz et al., 2022).

During the amplification through the turbulent dynamo, Schober et al. (2013) estimate the growth of the magnetic field with an exponential (also Pfrommer et al. 2022 estimate with an exponential):

$$B(t) = \begin{cases} B_0 \exp(\Gamma t) & t < t_{\rm sat}, \\ B_{\rm sat} & t > t_{\rm sat} \end{cases}. \tag{49}$$

Here, B_0 is the amplitude of the magnetic seed field and Γ is the growth rate. The time at which the maximum magnetic energy is reached at the injection scales is $t_{\rm sat}$. The growth rate can be estimated with (Pfrommer et al., 2022):

$$\Gamma = \frac{\mathcal{V}}{\mathcal{L}} {\rm Re}^{1/2}, \tag{50}$$

where $\mathcal{V}$ and $\mathcal{L}$ are the velocities and sizes of the injected eddies. The growth rate is most efficient for a high Reynolds number (equation 55).

At what strength $B_{\rm sat}$ is the magnetic field saturated? In theory, the magnetic field saturates, when the magnetic energy is in equipartition with the turbulent kinetic energy. The coherence length equals the eddy injection scale (see figure 10). Near the equipartition scale, the magnetic field is so strong that it backreacts onto the plasma (see e.g. Pfrommer et al. 2022). In strong, curved magnetic fields, the magnetic tension force is high and prevents the magnetic field from further folding. The tension can be released by a process called diffusive reconnection (Treumann & Baumjohann, 2013). Partly, it is released to turbulence in form of kinetic energy again. The diffusive reconnection lowers the magnetic field energy again and leads to an increase in the turbulent energy (S. Xu & Lazarian, 2020). At this point, the turbulent stretching of the magnetic field exactly balances the shrinking due to reconnection.

What is magnetic tension and why does it act in curved field lines? The coherence length and the energy in the magnetic field are strongly coupled to the curvature. This is referred to as helicity (Balsara et al., 2004). We take another look at the Lorentz force to better visualize this (Pfrommer et al., 2022):

$$\mathbf{f_L} = \frac{1}{c}\left(\mathbf{j}\times\mathbf{B}\right) = \frac{1}{4\pi}\left(\mathbf{B}\cdot\boldsymbol{\nabla}\right)\mathbf{B} - \frac{1}{8\pi}\nabla B^2 = \frac{B^2}{4\pi}\left(\mathbf{b}\cdot\boldsymbol{\nabla}\right)\mathbf{b} - \frac{1}{8\pi}\boldsymbol{\nabla}_\perp B^2. \tag{51}$$

Here, $\mathbf{j}$ is the current density, $\mathbf{B} = B\mathbf{b}$ and $\boldsymbol{\nabla}_\perp = (\mathbf{1} - \mathbf{bb})\boldsymbol{\nabla}$. The Lorentz force can be divided into two terms. The first one, $B^2/4\pi\left(\mathbf{b}\cdot\boldsymbol{\nabla}\right)\mathbf{b}$ is referred to as curvature term. The second term $1/8\pi\boldsymbol{\nabla}_\perp B^2$ is referred to as pressure term. Both act perpendicular to the field lines. The pressure term can be seen analogous to pressure in a fluid. It always points into the direction of less magnetic flux densities. The curvature force always acts to straighten the magnetic field lines. In highly curved fields with strong field strengths, the force becomes large and pushes the field lines to larger radii. There, the curvature force becomes weaker again. Physically speaking, the magnetic diffusive reconnection releases the high tension force in highly curved magnetic fields. Some of the energy is released back to turbulence (S. Xu & Lazarian, 2020).

In practise, it is topic of current research, what exactly causes the saturation of the magnetic dynamo at the large scales. Real turbulence is not only provided in solenoidal form. S. Xu & Lazarian (2020) suggest, that at the injection scales, for a self-gravitating system, the gas gets compressed again. This can cause the magnetic field to saturate, dependent on the density. They find a scaling of $B \propto \rho^{0.535}$ for a saturated dynamo, being subject to diffusive reconnection and being compressed (note, that they derived this for a star forming cloud, which can very efficiently cool and compress). Fitting to observations of nearby clusters yields a scaling of $B \propto \rho^{0.47}$ (Govoni et al., 2017; Kunz et al., 2022). We adapt a scaling of

$$B \propto \rho^{1/2} \tag{52}$$

as indicator for a saturated dynamo.

Not all kinetic energy can be converted into magnetic energy. Real turbulent motions do not only contain solenoidal motions, but also bulk motions and compressible motions (Schober et al., 2013; Carteret et al., 2023). Also, parts of the turbulent energy are dissipated into heat. Wittor et al. (2017) introduce an efficiency factor

$$E_{\mathrm{B}} = C_{\mathrm{E}} E_{\mathrm{turb}}, \tag{53}$$

stating, how much of the turbulent kinetic energy (equation 19) can be converted into magnetic energy (equation 40). Wittor et al. (2017) estimate the efficiency coefficient with $C_E = 4 - 5$ %. Carteret et al. (2023) find that a high amount of compressible motions in turbulence does not change the slope of the Kazantsev spectrum (48).

2.3.4 Simulating the Turbulent Small-Scale Dynamo

How can we create magnetic fields in a cosmological simulation? In our simulation, we do not include any astrophysical batteries. We add an initial homogeneous magnetic seed field, which we justify with the Biermann mechanism that can work in the early universe via means of structure formation processes. We use a magnetic seed field of comoving $10^{-14} G$ at $z = 127$.

How can we simulate the turbulent small scale dynamo? The efficiency of the turbulent dynamo is dependent on the smallest scales. The dynamo relies on the effects at the viscous and resistive scales. In our MHD equations (25)-(28), we assume a perfectly conducting (no resistivity and viscosity) fluid. Nevertheless, these show up as numerical effects. This is due to the finite volume and time discretization of our MHD solving approach (see subsection 2.2.5). Numerical diffusion can be described with (Wittor et al., 2017)

$$\eta_{\mathrm{n}} = 0.014 \epsilon^{3/2} l_{\mathrm{visc}}^2. \tag{54}$$

The numerical diffusivity is dependent on the eddy kinetic energy (equation 19) and the minimum scale of the turbulence. Here $l_{\mathrm{visc}} = 2 \cdot dx$, where dx is the cellsize (Wittor et al., 2017).

Our resolution is what defines the viscous scales, which is equivalent to the smallest eddy scales. The numerical Reynolds number can be estimated with (Pfrommer et al., 2022):

$$\mathrm{Re}_{\mathrm{n}} = \frac{\mathcal{L}\mathcal{V}}{\nu_{\mathrm{n}}} \sim \frac{3\mathcal{L}\mathcal{V}}{dx \mathrm{v}_{\mathrm{th}}}. \tag{55}$$

Here, ν_{n} is the numerical viscosity and dx is the cellsize. The velocity v_{th} is the thermal velocity of the cell. Both, the viscous scales and the resistive scales are dependent on the smallest cell sizes. Thus, $\mathrm{Pm} \approx 1$.

How does the magnetic field evolve in our simulation? How good can we resolve the turbulent dynamo in the ICM? How does including radiative physics in the simulation modify the performance? We analyse these questions in the analysis part of this thesis.

2.4 Galaxies

Why is it important to consider galaxies at this point? Galaxy clusters are filled with galaxies (see section 2.1.1). Galaxies provide a setup to grow a strong magnetic field in a short period of time, due to higher gas densities and a high amount of turbulence. In galaxy clusters, there is a large fraction of galaxies without any self-bound gas (Butcher & Oemler, 1984; Abadi et al., 1999). Different processes, such as galactic winds and ram pressure stripping can remove the high magnetic field gas from galaxies to pollute the ICM (de Gouveia Dal Pino et al., 2009; Serra et al., 2023).

2.4.1 Observations

Galaxies are subject to the theory of structure formation (section 2.1). Their sizes and masses, abundances and feedback processes are highly dependent on the age and environment of the galaxy (Kauffmann et al., 2003; Perret et al., 2014; Santini et al., 2017). Galaxies form from the collapse of an initial gas cloud inside dark matter halos. The first stellar populations start to form. Galaxies consist of dark matter, gas, which we refer to as Interstellar Medium (ISM) and stars. Most galaxies contain AGN. The halo masses lie in the range of $\sim 10^8 - 10^{14} M_\odot$. The star mass fraction lies in the range of $0.001 - 0.1$ (Mandelbaum et al., 2006). The gas mass fractions in galaxies vary widely. This is due to feedback processes and environmental effects.

Galaxy cluster at higher redshift are observed with large fractions of blue galaxies (they have a large gas amount and are star forming). Low redshift clusters show larger fractions of red galaxies (less gas and less star formation). This is referred to as the Butcher-Oemler effect (Butcher & Oemler, 1984; Abadi et al., 1999). This evolution is shown in figure 11. Each dot represents a galaxy cluster at different redshifts. With increasing redshift, the fraction of blue galaxies in the cluster increases. At $z = 0$, there are almost no blue galaxies in clusters. Thus, throughout time, galaxies undergo a morphology evolution from star forming to quiescent. What causes this?

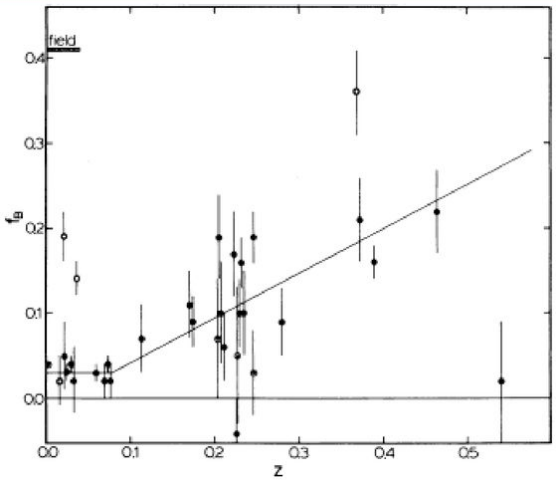

Figure 11: The Butcher-Oemler effect: with increasing redshift, the fraction of blue galaxies f_b increases. Each dot shows a galaxy cluster at different redshift. At low redshifts, there are almost no blue galaxies in clusters. Credits: (Butcher & Oemler, 1984).

What kind of feedback processes are there? Figure 12a shows a starburst galaxy with a galactic wind. It exhibits a period of enhanced star formation. The galactic wind, indicated in purple, is inferred from X-ray and Hα emission. The Hα emission is likely

(a) The starburst galaxy M82. The purple colors trace a galactic wind that is caused by supernovae in the starburst region. It indicates Hα emission, where hydrogen atoms in the winds are energized by radiation coming from the starburst region. Credits: Adam Block / UA SkyCenter / Caelum Obs

(b) The galaxy ESO 137-001 in the Norma cluster. ESO 137-001 is a so called jellyfish galaxy. The ICM strips gas from the galaxy, as it moves through the cluster. The stripped gas can cool, allowing to form neutral hydrogen (purple) and molecules, such as carbon dioxide (orange) (Jáchym et al., 2019).

Figure 12: Two different mechanisms that can remove gas from galaxies: galactic winds (left) and ram pressure stripping (right).

caused by high energy radiation that interacts with the galactic wind. High mass stars in the starburst region are sources for highly energetic radiation. The X-ray emission is likely caused by a shock that is embedded in the wind and heats up the surrounding gas (Lehnert et al., 1999).

What kind of environmental effects are there? Some galaxies in clusters are observed with a tail of neutral hydrogen that is stripped from the galaxy (Quilis et al., 2000; Serra et al., 2023). In high density environments (such as the ICM), gas from the galaxy can be pushed out, while the galaxy moves. Figure 12b shows a so-called jelly fish galaxy inside a cluster. The emission from the tail, indicated with purple colors, is tracing the neutral hydrogen. The orange spots are caused by molecular gas; hotspots of carbon dioxide emission (Jáchym et al., 2019).

Metals can be used as tracer for stellar activity and the processes in galaxies. The metal enrichment in the ICM is closely linked to the stellar evolution within galaxies. All metals in the ICM were created in stars and removed from the galaxies. At early times, the baryonic matter in the universe contained little to no metals (Prochaska et al., 2003). Metal distributions in nearby galaxy clusters can be observed with X-Ray telescopes via their emission lines. The ICM in nearby clusters is observed to have a metallicity of $Z \approx 0.3 Z_\odot$ (see e.g. Pfrommer 2022). The values are slightly higher in the centers, but homogeneous in the outskirts (Biffi et al., 2017). Metals are produced in galaxies and can be added to the ICM via galactic winds or ram pressure striping (Boselli et al., 2022).

2.4.2 Stellar Evolution in Galaxies, Galactic Winds and Ram Pressure Stripping

Why is it important to understand the stellar evolution in galaxies? Magnetic seed fields can be created in structure formation processes, supernovae or AGN outflows via means of the Biermann battery. Supernovae and AGN also provide energetic feedback, injecting turbulence onto the ISM. They can also launch galactic winds that remove the gas from galaxies. Here, we take a little detour on stellar evolution, to better understand how stellar and AGN feedback changes with time.

What is a galactic wind? Generally speaking, we refer to galactic wind as any kind of gas, that leaves a galaxy. The underlying feedback processes excert a pressure on the ISM and can potentially remove it from the galaxy. Galactic winds can be launched by stars or by the AGN (Heckman et al., 1990; Veilleux et al., 2005). What causes galactic winds? In starburst galaxies, galactic winds are mainly due to stellar feedback (Bookbinder et al., 1980; Heckman et al., 1990). In older and more massive galaxies, they are mainly due to AGN activity (Schawinski et al., 2007, 2014). SN and AGN can launch energetic feedback that drives hot bubbles. The bubbles push out the ISM. It can leave the galaxy (which we refer to as galactic wind). It can also fall back onto the galaxy, where it drives turbulence (de Gouveia Dal Pino et al., 2009).

The masses and abundances of the created stars in galaxies change throughout cosmic times. We describe the abundances of stars at different masses that form from the collapse of an initial gas cloud with a so called Initial Mass Function (IMF) (Vogelsberger et al., 2013):

$$\Phi(m) = \begin{cases} Am^{-3} \exp \frac{-log(m/m_c)^2}{2\sigma^2} & m < 1M_\odot, \\ Bm^{-2.3} & m > 1M_\odot \end{cases} . \tag{56}$$

We call a population of stars described with an IMF a Single Stellar Population (SSP). Here, $\Phi(m)[dN/d\log m]$ gives the number of stars that form with a certain mass m. The normalization coefficients m_c, σ, A and B can be tuned to match observed stellar populations at different redshifts. The possible masses of stars lie usually in the range $0.01M_\odot < m < 100M_\odot$. This IMF (equation 56) is characterised by a less steep slope of -2.3 for stars lighter than the sun and a steeper slope of -3 for stars with more than one solar mass. The slopes of this IMF are from Chabrier (2003). Physically speaking, this shows, how an SSP contains lots of low mass stars and only few high mass stars. The slopes of the IMF though changes throughout cosmic times. At early times, we use a so called bottom heavy IMF (Sartorio et al., 2023). It is indicated by a steeper slope for low mass stars and a less steep slope for high mass stars. Physically speaking, the bottom heavy IMF creates less low mass stars, but more higher mass stars. Throughout their lifetimes, galaxies have multiple starburst episodes. Thus, galaxies contain multiple SSP.

Why are stars in the young universe more massive and what kinds of implications does this have? At early times, the universe was much hotter, denser (see equation 6) and metal-poor (Jappsen et al., 2009). Gravitationally collapsed gas with these properties has a lower cooling efficiency (Yoshida et al., 2003). This allows to form very massive stars (Yoshida et al., 2006). Massive stars are short lived (Abel et al., 2002). The fuel for nuclear fusion is truncated fast and they explode as SN. This can transport the magnetic fields of the stars to the ISM, it can generate magnetic seed fields via means of the Biermann battery (Hanayama et al., 2005) (equation 45), it can add turbulence that amplifies already existing magnetic fields via means of the turbulent dynamo (Schober et al., 2013) (section 2.2.4) and it can cause galactic winds. The occurrence of galactic winds is dependent on the masses and abundances of stars. In young galaxies, galactic winds are thought to be mainly caused by stars (Bookbinder et al., 1980). Galaxies consist of multiple stellar populations. These form at different epochs in a galaxies life.

The photons emitted by the very first stars are highly energetic. They can potentially ionize whole galaxies. This phase in the cosmological evolution is referred to as reionization (Barkana & Loeb, 2001). It takes place at redshifts of $z \approx 7$ (Gnedin & Ostriker, 1997).

Galaxies with a low virial temperature (equation 7) $T_{200} < 10^4$ K can lose all their gas due to reionization (Barkana & Loeb, 1999).

AGN add energetic feedback onto the ISM. An AGN is powered by a supermassive black hole in the center of a galaxy. The black hole is surrounded by a gas accretion disk. The galaxy feeds the accretion disk with its gas reservoir. The AGN launches bipolar, high energy jets that are caused by strong toroidal magnetic fields (Lobanov, 1998). The amount of AGN feedback is dependent on the accretion efficiency. We differentiate between quasar mode feedback for a high accretion efficiency and radio mode feedback for a lower accretion efficiency. In the quasar mode, the jets consist mainly of highly energetic radiation. Quasars are among the brightest light sources in the night sky at high wavelengths. Quasars appear primarily at high redshifts. The amount of AGN feedback grows together with the bulge of their host galaxies (Shields et al., 2008; Lapi et al., 2014). The epoch of maximum quasar feedback is at $z \approx 2$ (Zakamska et al., 2016). This coincides with the peak of star formation efficiency (as star formation induced feedback feeds the AGN) (Dadina et al., 2022). Radio mode AGN are more effective in launching galactic winds and adding turbulence. They emit primarily in radio (Urry & Padovani, 1995). The launched jets consist mainly of relativistically moving, charged particles. The jets of radio mode AGN can inflate low density, high temperature bubbles that add mechanical feedback to the surrounding gas. The bubbles are filled with relativistic particles that create the radio emission. These bubbles are also referred to as radio bubbles (McNamara & Nulsen, 2012). They can be seen in X-ray images as cavities with lower densities (Bîrzan et al., 2004) (as seen in figure 6). These bubbles rise buoyantly. They excert a pressure on the ISM and can launch galactic winds (Torrey et al., 2020) and add turbulence. Radio mode feedback plays a dominant role in launching galactic winds for $z < 2$.

Galaxies can not only lose their gas reservoir through internal processes, but also via interactions with their surroundings. While moving through the ICM, it excerts a ram pressure on the ISM. This can potentially remove the gas from the galaxy (Jáchym et al., 2019; Serra et al., 2023).

How does this work? Though the ICM has a comparable low density, the velocities of the galaxies can be rather high. This creates a large ram pressure force. The gas is removed when the ram pressure is greater than the gravitational restoring energy per unit volume. Higher densities, as well as higher velocities cause a higher ram pressure. Thus, ram pressure stripping is mostly effective near the centers of galaxy clusters (Van De Ven et al., 2009).

We can calculate the possibility for ram pressure stripping to occur by balancing the restoring gravitational binding force onto the galaxy with the ram pressure excerted onto the galaxy. Assuming the galaxy to obey a cylindrical geometry, such that the geometry can be described by radius r_d and height z only. The gravitational potential of the galaxy is mainly dominated by dark matter. We therefore neglect baryons and only account for dark matter. We assume the galaxy to move through the ICM face on. In order to calculate the gravitational force, we would need to integrate the Poisson equation. In principle, it is complicated to get the density. We can decompose the galaxy into disk, bulge, halo and differentiate between stars and gas and also take the triaxial distribution of the dark matter halo into account. Instead, we assume a constant density of a cylindrical object that is moving face on through the ICM. The ram pressure criterion reads (Van De Ven et al., 2009):

$$\rho_{\mathrm{ICM}}(r)\mathrm{v}_{\mathrm{gal}}^2(r) = \frac{4\pi G M_{\mathrm{tot}}^2}{r_{\mathrm{d}}^4 \pi^2}, \tag{57}$$

where $\mathrm{v}_{\mathrm{gal}}(r)$ is the velocity of the galaxy, relative to the ICM velocity, M_{tot} is the total dark matter mass in the galaxy and r_{d} is the radius of the galaxy, assuming it to have a cylindrical form. If the ram pressure, on the left, exceeds the gravitational binding force, on the right, gas can be stripped from the galaxy. This is also referred to as Gunn and Gott criterion (Gunn & Gott, 1972).

2.4.3 Simulating Galaxies

How does including radiative physics influence the growth of the magnetic field in a cosmological simulation? In order to answer this question, we include the galaxy formation module (GFM) FABLE (Henden et al., 2018) in our simulation. It uses a subgrid model for star formation that is based on the GFM described by Vogelsberger et al. (2013). It includes a star formation and AGN module based on Hernquist & Springel (2003) and a module for radiative cooling and chemical enrichment based on Wiersma, Schaye, & Smith (2009). The feedback models are calibrated to reproduce observations.

How do we treat star formation and stellar feedback in our simulation? Similar to Vogelsberger et al. (2013), FABLE uses an effective equation of state for gas (equation 11) and a model for cooling of gas. Once, the gas reaches a density threshold ($0.13\ \mathrm{cm}^{-3}$), the gas cells are turned into star forming cells. A probability of turning into a star or a wind particle is assigned to each cell with an associated star forming time. To decide whether a cell is turned into a star or wind particle, a probability is assigned to it: $x \in (0, 1)$, where $x < \frac{1}{1+\eta_{\mathrm{W}}}$ is turned into a star particle with η_{W} being the wind mass load factor. Each star particle displays a SSP that is described with an IMF (equation 56). Vogelsberger et al. (2013) use the normalization coefficients $m_c = 0.079$, $\sigma = 0.69$, $A = 0.852464$ and $B = 0.237912$. The wind particles are decoupled from the hydrodynamics and only interact gravitationally. They carry the mass, metallicity and momentum of the initial gas cell. They recouple to the hydrodynamics again, after they travel for a certain time or when they encounter a gas cell that has a certain density treshold. Then, they deposit their mass, metallicity and momentum to the gas cell again. FABLE is based on the GFM of Vogelsberger et al. (2013) and uses the same approach (Henden, 2019).

With the IMF, the fraction of different star masses that are created is described. The feedback is dependent on the mass of the stars. Within each timestep, a mass loss and metal enrichment of the stellar population as a whole is calculated, based on the IMF. The times at which the wind particles are launched, as well as their abundance depend on the abundance of stars with different masses. The mass and metal return of high mass stars is treated directly in the same timestep, in which the wind particle forms. For the wind particles, representing the feedback from lower mass stars, it is more complicated. These have a time delay function that returns their mass in a later timestep. These two different wind models are referred to as the local and the non-local wind. The velocity of the wind is based on the 1D DM velocity dispersion $\sigma_{\mathrm{DM}}^{\mathrm{1D}}$ (assuming the galaxy to be virialized) (Vogelsberger et al., 2013):

$$\mathrm{v}_{\mathrm{W}} = \kappa_{\mathrm{W}} \sigma_{\mathrm{DM}}^{\mathrm{1D}}, \tag{58}$$

where κ_W is a dimensionless parameter, taking into account that the wind velocity is also correlated to the maximum rotational velocity of the galaxy. FABLE includes a bipolar wind model, where the wind particle can only be launched two directional (Henden, 2019).

The wind mass load factor is calculated as

$$\eta_W = \frac{1}{v_W^2}\left(\epsilon_W + \sqrt{\epsilon_W^2 + v_W^2 p^2}\right) \tag{59}$$

with ϵ_W being the specific wind energy provided by the SN and p is the momentum. In contrast to Vogelsberger et al. (2013), where the stellar feedback is purely kinetic (so $\epsilon_W = 0$), in FABLE, one third of the wind energy is deposited as thermal energy. This lowers the cooling efficiency and prevents the gas from directly falling back onto the galaxy (Henden et al., 2018; Henden, 2019).

The metal mass that is deposited, when the wind particle recouples to the hydrodynamics again, Z_W, is slightly modified from the metallicity of the initial gas cell, Z_{ISM}. This is due to the fact that a real wind will strip and carry ISM, as it moves through the galaxy. The metal loss factor γ_W (Vogelsberger et al., 2013) reads:

$$Z_W = \gamma_W Z_{ISM}. \tag{60}$$

In order to account for cooling, FABLE includes a cooling function, based on the work of Wiersma, Schaye, Theuns, et al. (2009):

$$\Lambda(T, \rho, z, Z) = \Lambda_p(T, \rho, z) + \frac{Z}{Z_\odot}\Lambda_m(T, \rho, z) + \Lambda_C(T, \rho, z). \tag{61}$$

Metal line cooling $\frac{Z}{Z_\odot}\Lambda_m(T, \rho, z)$ is dependent on CLOUDY cooling tables, including different element abundances, temperatures and associated cooling rates: Also Compton cooling off the CMB $\Lambda_C(T, \rho, z)$ is added. Primordial cooling and heating $\Lambda_p(T, \rho, z)$ is accounted for separately. It is derived from ionization equations that rely on the cooling, recombination and ionization rates of primodial gas. The UV background (mainly caused by quasars and starburst galaxies) is included. A uniform time-dependent UV background is assumed (Wiersma, Schaye, Theuns, et al., 2009; Vogelsberger et al., 2013).

The AGN module in FABLE is based on the AGN module of Vogelsberger et al. (2013). The feedback induced by AGN depends on the AGN accretion rate. The gas accretion rate is modeled with a Bondi-Hoyle-Lyttleton based Eddington limited rate. The accretion efficiency gets lower with rising galaxy masses. 10 percent of the accreted mass is added to the BH mass, the rest is released as energy in form of feedback. The feedback model is a two state model. It is differentiated based on the mass accretion rate. For $\dot{M}_{BH}/\dot{M}_{Edd} < 0.01$, the actual accretion rate of the black hole, compared to the Eddignton accretion rate, the BH is in radio mode, adding mechanical energy to its environment. Otherwise it is in quasar mode and adding thermal energy to its environment. In the quasar mode, a fraction of the accreted mass is released and couples as thermal energy (with an efficiency $\epsilon_r = 0.1$) isotropically to nearby gas cells within the thermal feedback radius. The quasar mode is dominant at high redshifts. In contrast to the approach of Vogelsberger et al. (2013), the quasar mode feedback in FABLE is not continuous, the feedback is injected all $\Delta t = 25$ Myr timesteps (Henden, 2019). For the radio mode, the AGN injects hot, buoyantly rising bubbles. The radio mode AGN module is based on the work of Sijacki

et al. (2007). The time of the bubble injection and energy content and sizes are based on the BHs mass and and accretion rate. The bubbles are injected, whenever the BH mass has grown by a factor $\delta_{\mathrm{BH}} = \delta M_{\mathrm{BH}}/M_{\mathrm{BH}}$. The bubbles have fixed radii, travel distances, energies and an efficiency factor (with an efficiency factor $\epsilon_q = 0.08$). The radio mode feedback is the dominant channel for lower redshifts. The remainder of the available energy for feedback in quasar and radio mode is released as radiation in the direct surroundings of the black hole (Henden, 2019).

In order to identify galaxies in our simulation, we use the SUBFIND algorithm (Dolag et al., 2009). In addition to the FoF algorithm, as discussed in section 2.1.3, the SUBFIND algorithm takes baryonic physics into account. First, overdense structures are identified by drawing density contours around overdense regions. In a next step, a gravitational unbinding procedure is applied, where random velocities are assigned to the particles in an overdense structure. If more than a threshold of the particles survives this procedure, the halo is counted as subhalo (galaxy). The procedure is applied to the DM particles, but also to the stars and black holes. A virial radius and center of mass is calculated for each subhalo.

3 Analysis

3.1 Magnetic Field at $z = 0$

How does including radiative physics in a cosmological simulation influence the magnetic field evolution in galaxy clusters? We analyse the evolution of the magnetic field in the radiative setup and in the non-radiative setup. We start the analysis with looking at the large-scale behaviour of the magnetic field in both simulation setups across the galaxy cluster. In figure 13, we show a projection of the magnetic field strength at $z = 0$ for both simulation runs. The left panel shows the radiative run and the right panel the non-radiative run. The magnetic field strength looks comparable in both runs inside the virial radius, which is indicated with the white circle.

The highest magnetic field strength values are reached in the center, where the densities are highest. It decreases towards the outskirts. Both runs reach values of $\sim 5\mu$G in the center with locally, small-scale higher peaks. There are small differences in the fine-structure of the magnetic field. The non-radiative run has a more filamentary structure. This can be an artefact of the projection. Projecting along non-overlying filaments could erase them in the radiative run. This can be caused by turbulence. The magnetic field strength has a smoother distribution in the radiative run. It shows slightly higher values, compared to the non-radiative run, in the outskirts. The non-radiative run shows a steeper decline towards the outskirts. This is due to the fact that accreted objects (galaxies and smaller clusters) bring their own high magnetic field gas. This enriches the outskirts.

In the radiative run, we see little dots with high magnetic field values beyond the virial radius. These are galaxies. The accretion of already pre-enriched objects also yields higher magnetic field values beyond the virial radius in the radiative run. The magnetic field beyond the virial radius is non-symmetric. This is due to the filaments of the cosmic web. They are connected to the cluster in the upper left and lower right. In the radiative run, the infalling galaxies move on the filaments. The galaxies can be seen as spots with an increased magnetic field strength (in the upper left and right). In the galaxies, where the cooling is very efficient, the gas can reach high densities. The flux freezing enables higher magnetic field strengths. The magnetic field values are slightly higher in filamentary-direction, especially to the lower right.

To summarize, at $z = 0$, the magnetic field looks comparable in both runs inside the virial radius. The non-radiative run shows a slightly higher amount of fine-structure. Beyond, it is more extended along the filaments and more puffy in the radiative run. In the radiative run, the filaments carry already pre-enriched gas that is being accreted onto the cluster.

3.1.1 Discussion

Our magnetic field strength values are matching with observations. Faraday rotation measures yield 3.9-5.4μG in the coma cluster (Kunz et al., 2022). Osinga et al. (2022) find central values of $5 - 10\mu$G and declining with a power law towards the outskirts. They use depolarizaion of radio emission from clusters to measure the magnetic field strength in a sample of galaxy clusters at $z < 0.35$. Radio emission emitted by a narrow source is polarized. When measuring the radio emission from a large volume, different polarization states would cancel and yield, in total, unpolarized emission. Osinga et al. (2022) find that the state of depolarization is high in the center. For dynamically disturbed clusters, they also find a high depolarization state at the outer radii. Comparing to our findings, where the non-radiative run shows a higher fine structure, we can associate this to a more

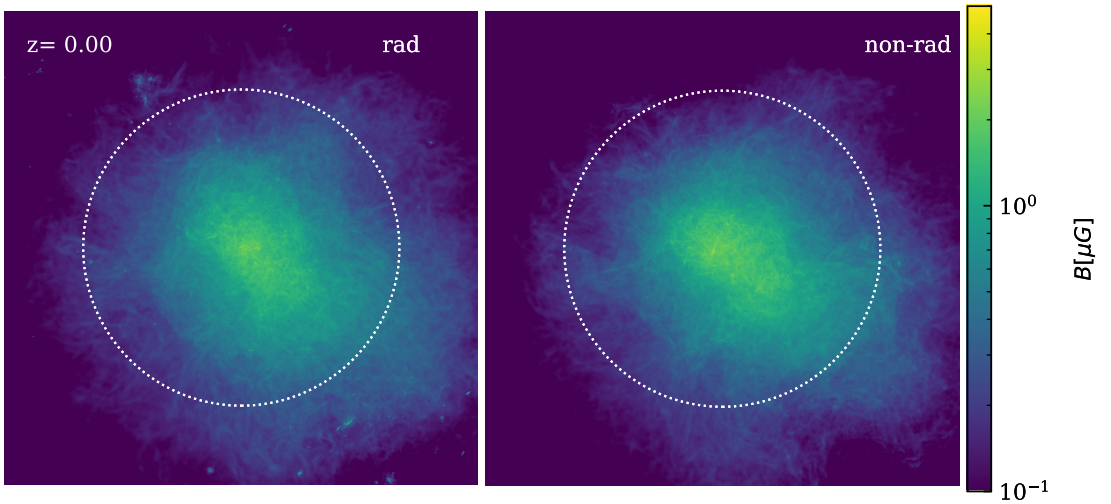

Figure 13: A projection of the volume averaged root mean square magnetic field strength at $z = 0$. The projection box has side lengths of $3 \cdot R_{200}(z = 0)$ with $R_{200}(z = 0) = 2967.94$ kpc and a similar projection depth. The virial radius is indicated with the white circle. We show the radiative simulation on the left and the non-radiative simulation on the right.

narrow region containing the magnetic field. Whereas in the radiative run, the magnetic field is more volume filling.

Marinacci et al. (2015) do cosmological simulations, where they compare non-radiative simulations with simulations including a galaxy formation and feedback module. They also find that, at $z = 0$, both simulations yield the same large scale magnetic field features. In agreement with our findings, they find that the peak values of the magnetic field are coinciding with density peaks, such that the magnetic field strength is high in the center of massive halos. In contrast to our findings, they find that the magnetic field strength in halos reaches over all higher values at $z = 0$ in the radiative simulation than in the non-radiative simulation. They also find that their most massive halos are still connected to the cosmic web, which is weakly magnetised in the filaments. In agreement with our results, they find that outside the virial radius, locally increased magnetic fields are coinciding with density peaks carried by infalling substructures.

3.2 Density Profiles

The magnetic field can be strongly coupled to the plasma density via compression (see equation 16). We show the radial density profiles in figure 14. We show the radiative run on the upper row and the non-radiative run in the lower row. We compare the physical quantities, on the left, against the scaled quantities, on the right. We scale against the critical density and the virial radius. We show the profiles for nine different redshifts, indicated with the color scheme. All profiles have central peaks and a decline with radius. This is matching with our findings of the magnetic field strength following the same morphology (see figure 13).

At low redshift, the density profiles in the radiative and in the non-radiative simulation are very similar. We fit a single beta profile (equation 13) to the density profile at $z = 0$. The fit yields parameters of $\rho_{0,1} = 5.73 \cdot 10^{-27}\text{gcm}^{-3}$, $r_{0,1} = 139\text{kpc}$, and $\beta_1 = 0.3$ for the radiative run. For the non-radiative run, it yields $\rho_{0,1} = 4.7 \cdot 10^{-27}\text{gcm}^{-3}$, $r_{0,1} = 330\text{kpc}$, and $\beta_1 = 0.46$. Inside the virial radius, the fitted profiles match the simulated profiles well. Beyond, the fitted profile yields higher values. This can be due to the fact, that the

beta parameter varies with radius, whereas we assumed it to be constant. Especially in the outskirts, the thermal energy decreases, which would yield a higher beta parameter and thus a steeper fall of the beta profile. The outskirts are dominated by merger and accretion of gas. Comparing to generic profiles, such as the beta profile, is non-robust in these regions.

The physical profiles, on the left, show a redshift dependent trend. The radiative simulation shows central higher values at high redshifts. This is due to more efficient cooling (that scales with density squared and is very effective in the center; see equation 61) and thus higher densities. With lower redshift, the high central values decrease in both runs. This can be due to AGN feedback and less efficient cooling in the radiative run. As the critical density decreases with decreasing redshift, also the accreted matter comes with lower densities. This lowers the density of the total cluster. In the left panel, we also see how the virial radius grows with decreasing redshift. We compare to the right panel. In the non-radiative run, the density profile seems to be redshift-independent. This shows, how the cluster grows self-similarly with redshift. The density profile within the virial radius is only dependent on the critical density of the universe. In the radiative run, the central profiles are not self-similar across different redshifts. At higher redshift, the values are higher and decrease towards lower redshift. This can be also associated to more efficient cooling in the center. Later, the AGN injects energy into the central regions, diluting the ICM and yielding lower values again. The size of the central region stays fixed in units of the virial radius at the high redshifts.

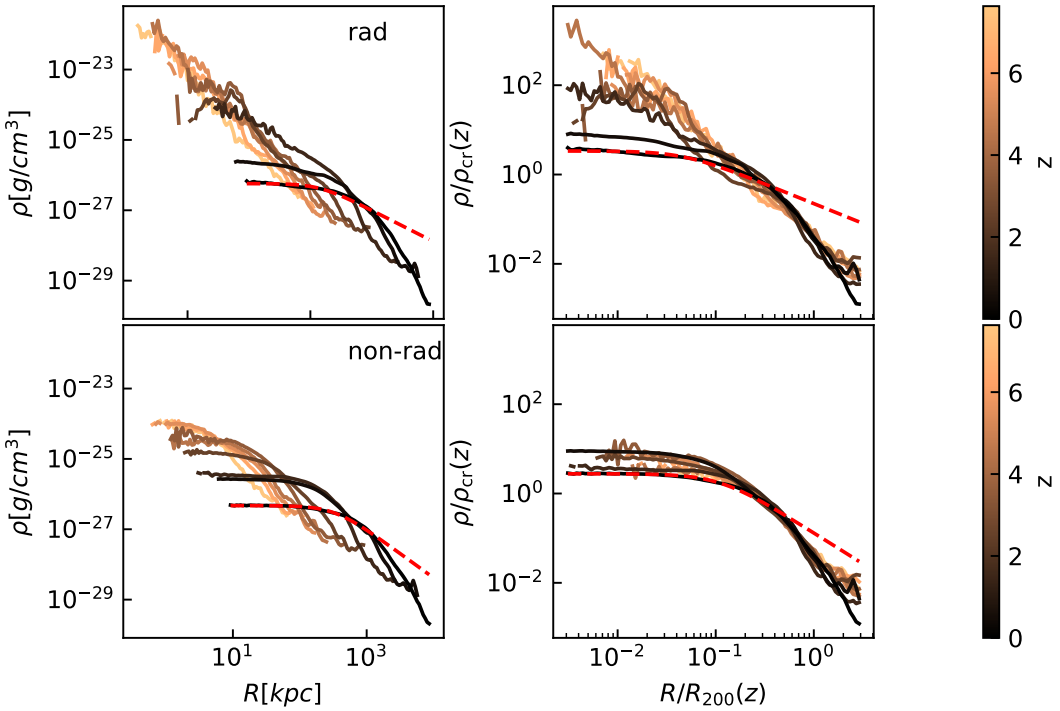

Figure 14: Radial profiles of the volume weighted density. The upper panel shows the radiative run, the lower one the non-radiative run. On the left, we show the physical quantities. On the right, we show the density in units of the critical density and the radius in units of the virial radius. The different colors indicate nine different redshifts. The red, dashed line indicates a beta profile, fitted to the $z = 0$ density profile.

3.2.1 Discussion

The single beta profile is characteristic for non-cool core clusters (Patej & Loeb, 2015). McDonald et al. (2017) compare observations of a cool core cluster sample at $0 < z < 1.9$ taken from Sunyaev-Zeldovich and X-ray measurements. They find that a cool core cluster density profile can be combined from a high density core profile that has a fixed size and density across different redshifts and a lower density profile that determines the outer radii and grows self-similar together with the critical density of the Universe across different redshifts. This is matching with our findings, assuming that our non-cool core cluster only follows this self-similar growth. In difference to McDonald et al. (2017), we simulate at higher redshifts and not only at lower ones. Thus, we cannot compare the redshift evolution beyond $z > 2$. Also, we simulate a non-cool core cluster, whereas McDonald et al. (2017) observe cool core clusters. Nevertheless, we also see, how the outer profiles evolve self-similar with redshift (see figure 10 from McDonald et al. (2017)). Also our cluster core in the radiative run have approximately the same size and density across the higher redshifts (see upper right panel of figure 14).

Mohr et al. (1999) observe a sample of nearby clusters in the X-rays. They fit a single beta profile. They find lower β values compared to $\beta \sim 1$, which is usually assumed (Pfrommer, 2022). This is matching with our findings. They find a distribution of beta parameters for different clusters $0.35 < \beta < 0.7$ (see their figure 9). Our fit values sit at the low end of this range. Mohr et al. (1999) also find that central lower X-ray temperatures correspond to a peak in the density profile in the center. Thus, higher temperatures imply lower beta values. As the cluster from our simulation sits at the high mass end, this can explain our low beta values. Higher masses correspond to higher gas temperatures (see equation 7). Mohr et al. (1999) only fit within the virial radius. They also highlight that the radial dependence of β should be kept in mind and that thus, the fitted profiles do not account for all radii.

Patej & Loeb (2015) establish a model for density profiles of non-cool core clusters and compare against the observations of Mohr et al. (1999). They find that the density in the center is dependent on the central cooling time. Assuming different entropy levels in the center, they find a flat, high density profile (for lower entropy) and a flat, low density profile (for higher entropy). In the outer radii, they recover the same profile for all entropy levels (see figure 7 of Patej & Loeb 2015). They find that balance between AGN activity, gravity and cooling is not sufficient to explain the central flat density profiles. They suggest that the infalling gas is preheated. Comparing to our findings, this could explain why, beyond the virial radius, our density profiles lie below our fitted beta profiles. Before entering the cluster, the gas is preheated via an accretion shock, yielding the low densities.

3.3 Magnetic Field Evolution with Time

We want to study the magnetic field evolution with time in our simulated galaxy cluster. What are the differences in the evolution between the radiative and the non-radiative run? Comparing these, enables us to separate the effects caused by radiative physics from other effects that could influence the magnetic field, such as the turbulent dynamo.

In figure 15, we show how the magnetic field strength evolves with redshift. We show the radiative run in the upper panel and the non-radiative one in the lower panel. We differentiate between the physical quantities, on the left and the comoving ones, on the right (see equation 39 for the calculation from physical to comoving). We show four

different radial bins in fractions of the virial radius $R_{200}(z)$, indicated with the color scheme. The magnetic field in galaxies is indicated with the red color for the radiative run. The dashed vertical lines indicate the collapse of the protocluster at $z = 9.5$ and two merger that are happening at $z = 4.5$ and at $z = 2$. The magnetic field grows faster in the radiative run and reaches saturation earlier. This can be due to galaxies that eject their high magnetic field gas into the ICM in the radiative run. In the galaxies, we reach magnetic field strengths of $B \approx 20\mu$G. The saturated values for the ICM, in the radiative and in the non-radiative run, are very similar. In the most central bin, we reach values of $B \approx 5\mu$G, while in the most outer bin, 0.8μG

3.3.1 The Radiative Simulation

After the collapse of the protocluster at $z = 9.5$, the magnetic field strength rises almost vertically in all panels. This is due to the abrupt density increase, caused by the collapse. Afterwards, a structure formation shock adds turbulence to the ICM and can amplify the magnetic field further, for example with the small-scale dynamo. In the radiative run, the magnetic field is saturated at $z \approx 3.5$. The amplification in the radiative run can be divided into two phases $9.5 < z < 4.5$ and $4.5 < z < 3.5$ that are separated by the structure formation collapse (first black vertical line) and the first bigger merger (second vertical line).

In the first phase, the magnetic field reaches a peak value and decreases again. In the ICM, the magnetic field is strongest in the central $1/4R_{200}$ bin. The magnetic field strength decreases with radius. The bump in the first phase is most pronounced for the galaxies, followed by the central radial bin and least pronounced for the outer radial bin. Inside galaxies, gas cooling leads to higher densities, enabling also a higher magnetic field strength. Also the first SN start to go off and add turbulence to the gas in the galaxies, which is efficient to amplify the magnetic field in the galaxies. We see that the shape of the curves in the cluster follows tightly the one from the galaxies. The galaxy curve starts to rise earlier and reaches higher values. The magnetic field grows together with the star forming regions. At these high redshifts, $9.5 < z < 4.5$, the star forming regions are dominated by the BCG, where most stars are created. The high magnetic field gas, associated to the star forming regions (mostly in the center), is ejected into the central ICM and gets diluted towards the outskirts. This could explain the very pronounced bump in the inner radial bin and least pronounced bump in the outer radial bin in the first phase.

Now we look at the second phase, after the first merger. In the second phase, from $4.5 < z < 3.5$, the magnetic field rises exponentially in the whole ICM and in the galaxies. After the exponential growth, it saturates in all radial bins. Again, the trend in the ICM follows the one in the galaxies, only at lower values. The first merger coincides with a drop of the magnetic field strength in all radial bins and in the galaxies. The merger adds new galaxies and gas to the cluster that have potentially lower field strengths. The explanation is that these objects are attracted by the cluster, meaning that they are less massive and have formed later and had less time to form a magnetic field. The merger also adds a high amount of turbulence to the ICM, which can give rise to a turbulent dynamo. How can we explain the similarity between the magnetic field evolution in the galaxies and in the ICM? Stars in the early Universe go off as SN, as soon as they are created. These first stars are very massive and big due to a lack of efficient cooling (as discussed in section 2.4.3). The SN add a high amount of turbulence to the star forming regions. In the star forming regions, the cells are small due to the efficient gas cooling. Both enables the turbulent dynamo to efficiently amplify magnetic fields, which explains

the high magnetic field in the star forming regions. Looking at the ICM, galaxies can lose their gas due to ram pressure stripping or galactic winds. Additionally, the first merger injects a high amount of turbulence, which can enable the turbulent dynamo to further amplify the magnetic field in the ICM.

3.3.2 The Non-Radiative Simulation

In the non-radiative simulation, the magnetic field saturates at $z \approx 1$. We also separate the evolution, dependent on the merger. From $9.5 > z > 4.5$, the physical magnetic field strength stays constant in the inner radial bins and decreases slightly in the outer radial bin. The ICM is gravitationally collapsed, but can not reach higher densities, because it cannot cool in the inner bins. In the outer bins, the high temperatures cause the gas to expand, yielding lower magnetic field values. In the second phase, from $4.5 > z > 2$, where the second merger is happening (indicated with the third vertical line), the magnetic field rises exponentially. The exponent is highest for the inner radial bin. Directly after the merger, there is an initial rise and decrease of the magnetic field in the outer most radial bin. This bump is less pronounced for the inner bins. As the merger enters the cluster, it can add its central, high magnetic field gas to the outer radial bin. As the merger proceeds, turbulence distributes this gas throughout the whole ICM, yielding lower values in the outer radial bins again. The merger injects a high amount of turbulence, enabling the turbulent dynamo to act. In the center, the densities are highest, which can make the turbulent dynamo more efficient (as higher densities enable smaller cells). After the second merger, that again adds a high amount of turbulence, the magnetic field grows even faster, again fastest in the center. In contrast to the radiative run, the transition from a growing magnetic field to a saturated one is more smooth instead of abrupt. In the outer radial bin, this transition happens the slowest.

3.3.3 High Redshifts and Low Redshifts

Before the collapse of the protocluster, at $z = 9.5$, the magnetic field strength is dominated by the expansion of the universe. We use the high resolution region to compute the magnetic field strength. We fit a power law to the physical magnetic field strengths in the radiative and in the non-radiative run. For the non-radiative run, we find a scaling $B \propto z^{1.9}$. This is an indicator for the magnetic field being diluted due to the expansion of the universe. In the case of adiabatic expansion of a density field, the magnetic field scales as $B \propto \rho^{2/3}$ (see equation 16). The density scales with the scale factor as $\rho \propto a^{-3}$, such that $\rho \propto (1+z)^3$. This yields $B \propto (1+z)^2$. In the non-radiative simulation with the comoving quantities, the magnetic field strength stays constant before the collapse. It gets diluted, because the universe expands. In the radiative run, we fit the magnetic field strength to scale as $B \propto z^{2.9}$, which is a too steep decrease for it to be caused by adiabatic expansion only. The dilution of the magnetic field is associated to radiative physics acting on top of the dilution because of the expansion of the universe. Looking at the our gas cooling function (equation 61), this additional decrease can be caused by primordial heating or by our UV background. It cannot be caused by AGN or stars adding energy, because the first AGN and stars only form after the collapse of the protocluster.

The magnetic field stays saturated until $z = 0$ (we only show until $z = 10^{-2}$ because of the logarithmic scaling). In the absence of any process that amplifies the magnetic field, it would decay due to numerical diffusion. Frequent merger keep injecting turbulent energy that is converted to magnetic energy and keeps the magnetic field strength constant (we

discuss this in section 3.4).

To summarize, including radiative physics enables the magnetic field to grow faster. In the radiative run, there are two phases of interest: $9.5 < z < 4.5$, where we see the bump and $4.5 < z < 2$, where the magnetic field rises exponentially. These regimes look different in the non-radiative run. There is no change in the magnetic field strength in the first phase in the non-radiative run. Thus, the bump in the radiative run is purely caused by the effects of radiative physics. Especially, it is dominated by the star forming regions that, in return, are mostly dominated by the BCG. In the second phase, the magnetic field rises steeper in the radiative run and reaches saturation before the end of the second phase, while in the non-radiative run, it also keeps growing afterwards. In the non-radiative run, the growth is presumably caused by turbulence, added by the first merger. In the radiative run, the effects of radiative physics act on top of the (presumably) dynamo. Galaxies can faster grow a stronger magnetic field. Cooling of gas enables high densities, especially in galaxies. Through adiabatic compression, this can yield higher magnetic field values. Additionally, massive SN explosions in the early universe add turbulence to the high density regions, enabling a more efficient turbulent dynamo to work (we discuss this in sections 3.6 and 3.8.2). The galaxies can lose their high magnetic field gas to the ICM, where it acts such that it adds higher initial seed field values, making a dynamo even more efficient (we discuss this in sections 3.3.6 and 3.8).

3.3.4 Fitting Growth Rates

We want to compare the growth of the magnetic field, dependent on the age of the universe, in the radiative and in the non-radiative run. As introduced in the previous section, we look at the second growth phase, separated by the two merger at $z = 4.5$ and $z = 2$. These redshifts corresponds to an age of the universe of $t = 1.4$Gyrs and $t = 3.3$Gyrs, respectively (see equation 5). In this phase, the radiative run experiences the exponential growth between $t = 1.4$Gyrs and $t = 1.9$Gyrs (corresponding to $z = 4.5$ and $z = 3.5$). In the non-radiative run, the magnetic field experiences its first exponential growth phase. Only here, we also analyse the zoom8 run. We compare the zoom8 and the zoom12 growth rates to see the effects of the resolution. We analyse the growth rates for the center of the cluster $R < 1/4 \cdot R_{200}$, where the densities are highest and thus, the cell sizes are smallest.

In figure 16, we fit growth rates to the growth of the magnetic field in the radiative zoom8 and zoom12 run and also to the star forming regions in the zoom8 and zoom12 run (on the left) and to the zoom8 and zoom12 non-radiative runs (on the right). We fit the growth rates accordingly to equation (49). The growth rates in the radiative run are higher by more than a factor of 10. In the radiative run, the growth rates in the galaxies and in the different zoom factors are at the same order of magnitude. In the non-radiative run, the zoom8 growth rate is smaller by a factor of 2, compared to the zoom12 run. In the radiative run, the growth rates are higher by a factor of 10 (compared to the zoom12 non-radiative run) and higher by a factor of roughly 20 (compared to the zoom8 non-radiative run).

First, we analyse the radiative run. We compare the zoom8 and zoom12 run. The magnetic field strength of the zoom8 run lies above the zoom12 run, when the universe has an age of 1.3Gyrs, which is contradictory to dynamo theory, where the magnetic field grows faster with a higher resolution. The exponential growth starts and the zoom12 run catches up. We fit the growth rates for the ICM to be $\Gamma_8 = 14.45\text{Gyr}^{-1}$ in the zoom8 run and $\Gamma_{12} = 13.94\text{Gyr}^{-1}$ in the zoom12 run. For the galaxies, we fit growth rates of $\Gamma_{G8} = 14.85\text{Gyr}^{-1}$ in the zoom8 run and $\Gamma_{G12} = 16.03\text{Gyr}^{-1}$ in the zoom12 run. The fitted exponential curves approximately match the magnetic field curves. An exponential rise of

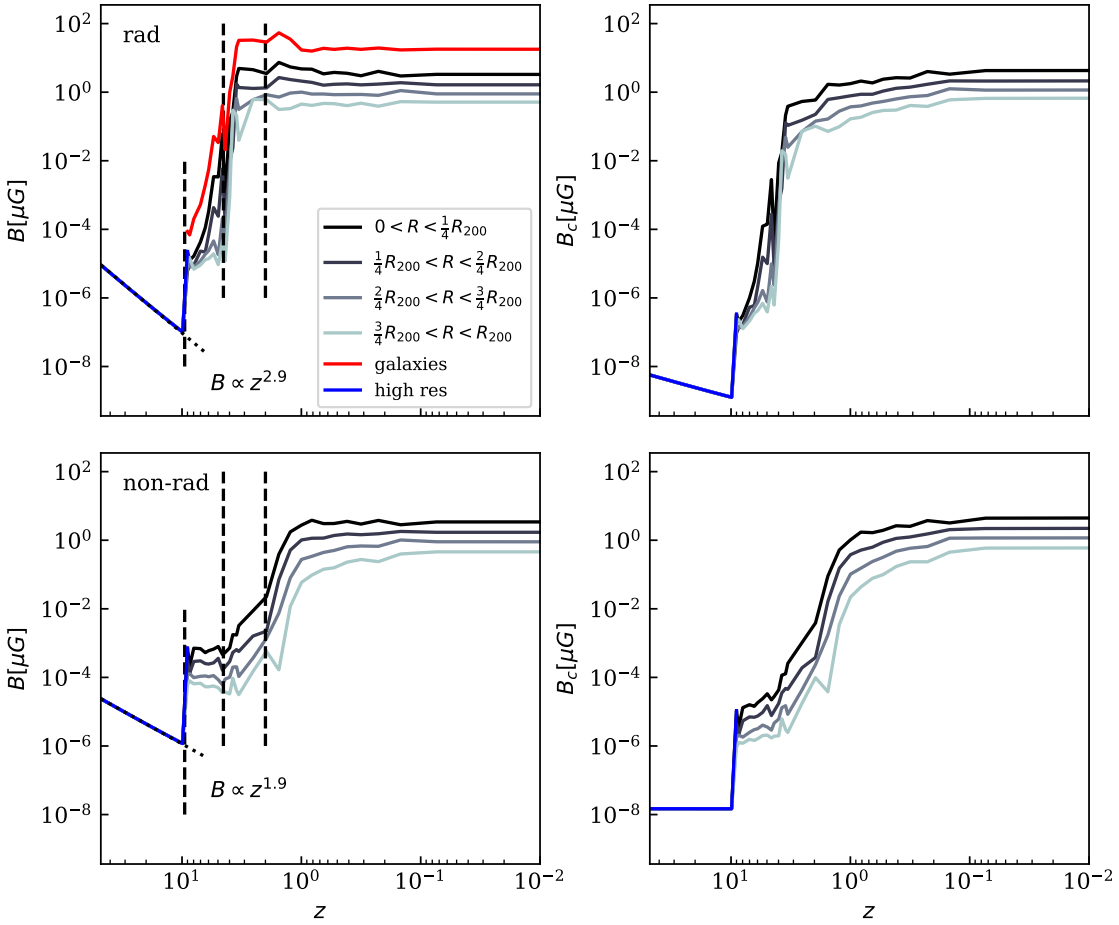

Figure 15: The volume averaged root mean square magnetic field strength. In the radiative run (upper panel) and the non-radiative run. The left panel shows the physical values, the right panel shows the comoving values. We show the volume averaged values of the magnetic field in the ICM for four different radial bins in fractions of the virial radius, indicated with the different blue colors. Blue (the high resolution label) indicates the volume averaged magnetic field strength taken from the high resolution region (The protocluster only collapses at $z = 9.5$). Star forming regions are excluded from the ICM. Red shows the volume averaged root mean square magnetic field strength of the gas inside galaxies (gas cells with a star formation rate>0). The black dotted lines indicate our power law fits. The vertical black, dashed lines indicate the collapse of the protocluster at $z = 9.5$ and merger that are happening at $z = 4.5$ and $z = 2$.

the magnetic field strength with time is characteristic for a turbulent dynamo. Smaller cells (a better resolution), enable a higher numeric Reynolds Number (see equation 55) and thus a higher growth rate (see equation 50). Contradictory to this, the growth rates in the zoom12 run are not higher, compared to the zoom8 run in the ICM, but not in the star forming regions. We can explain this with the fact that the fitted curves match the curves emerging from the simulation, not perfectly. What is also interesting is that all growth rates lie in the same order of magnitude. What amplifies the magnetic field is almost equally efficient in the galaxies, as well as in the ICM. In general, the similar growth rates confirm that the magnetic field curves in the ICM follow the tend of the curves in the galaxies very closely, which we already saw in figure 15. This shows that including radiative physics can amplify a magnetic field faster than an increased resolution does. In

fact, increasing the resolution on top of including radiative physics, does not significantly effect the magnetic field evolution.

Now we analyse the magnetic field growth in the non-radiative run (right panel of figure 16). Again, we fit growth rates to the zoom8 and the zoom12 run. We fit growth rates of $\Gamma_8 = 0.61\mathrm{Gyr}^{-1}$ to the zoom8 run and $\Gamma_{12} = 1.28\mathrm{Gyr}^{-1}$ to the zoom12 run. The zoom12 run has always a higher magnetic field, compared to the zoom8 run, in contrast to the radiative run, where initially, the zoom8 run has higher field values. The fitted curves match the simulated ones very well. This also indicates here that a dynamo is acting in the ICM. Turbulence is injected by the merger at $t = 1.4$Gyrs and the turbulent energy can then be converted into magnetic energy. The growth rate in the zoom12 run is larger by more than a factor of 2, compared to the zoom8 run. This makes sense, as the growth rate in case of a dynamo is dependent on the resolution. It is to be kept in mind, that the magnetic field keeps growing after this phase in the non-radiative run (with a higher exponent, as shown in figure 15).

Following Pfrommer et al. (2022), we estimate the numerical Reynolds numbers $\mathrm{Re_n}$ for the high resolution zoom12 run in the ICM. We can estimate the numerical Reynolds number with equation (55). Turbulence in the ICM is subsonic. We estimate the ratio of turbulence injection velocity to thermal velocity in the center as $\mathcal{V}/\mathrm{v_{th}} = 0.8$ for the radiative run and $\mathcal{V}/\mathrm{v_{th}} = 0.7$ for the non-radiative run (see figure A.1). In the radiative run, this ratio is higher, as the AGN is in the quasar mode (see section 2.4.3) and adds energy in the form of radiation to the surrounding gas cells. We estimate the cell sizes as $dx = 2$kpc for the central ICM in the radiative run. For the non-radiative run, we estimate the cell sizes in the central ICM as $dx = 6$kpc (see figure A.2). We estimate the injection scale of the turbulence as $\mathcal{L} = 120$kpc, which corresponds to the virial radius $R = R_{200}(z = 3.98) \approx 120$kpc. At $z = 3.98$, we are in the regime of the exponential growth. For the central ICM in the zoom12 run, this yields a $\mathrm{Re_n} = 144$ for the radiative run and a $\mathrm{Re_n} = 42$ for the non-radiative run. The growth rate is approximately the eddy turn over rate: $\Gamma \sim \mathrm{v}_\lambda/(2\pi\lambda)$, where $\mathrm{v}_\lambda = \mathcal{V}\mathrm{Re}^{-1/4}$. We estimate the thermal velocities in the center as $\mathrm{v_{th}} = 420$km/s in the radiative run and $\mathrm{v_{th}} = 360$km/s in the non-radiative run. This yields turbulence injection velocities of $\mathcal{V} = 336$km/s for the radiative run and $\mathcal{V} = 252$km/s in the non-radiative run. Assuming $\lambda = 2 \cdot dx$ as the scale of the eddies in the center, this yields growth rates of $\Gamma = 3.95\mathrm{Gyr}^{-1}$ in the radiative run and $\Gamma = 1.34\mathrm{Gyr}^{-1}$ in the non-radiative run. For the non-radiative run, this matches our fitted growth rate very well. Our fitted growth rate is smaller by a factor of 0.95, compared to the analytical estimate. Additionally, our analytical approach assumes smallest cell sizes, which is only valid for the very center and not for the whole $R < 0.25 \cdot R_{200}$ region like we assumed when comparing those numbers. In the radiative run, our fitted growth rate is larger than the analytical one by a factor of 3.53. This is an evidence that something is acting on top of the (presumably) dynamo and yielding a faster amplification of the magnetic field.

While an exponential fits the growth in the non-radiative run very well, this is not the case for the radiative run. This is an indicator that things apart from a "simple" dynamo are acting. Presumably, different dynamo act on top of each other or effects that are associated to the star forming regions, encounter.

3.3.5 Merger

A galaxy cluster grows through mergers. Merging galaxies can potentially have an already pre-enriched, higher magnetic field. As we have shown in figure 15, a strong magnetic field

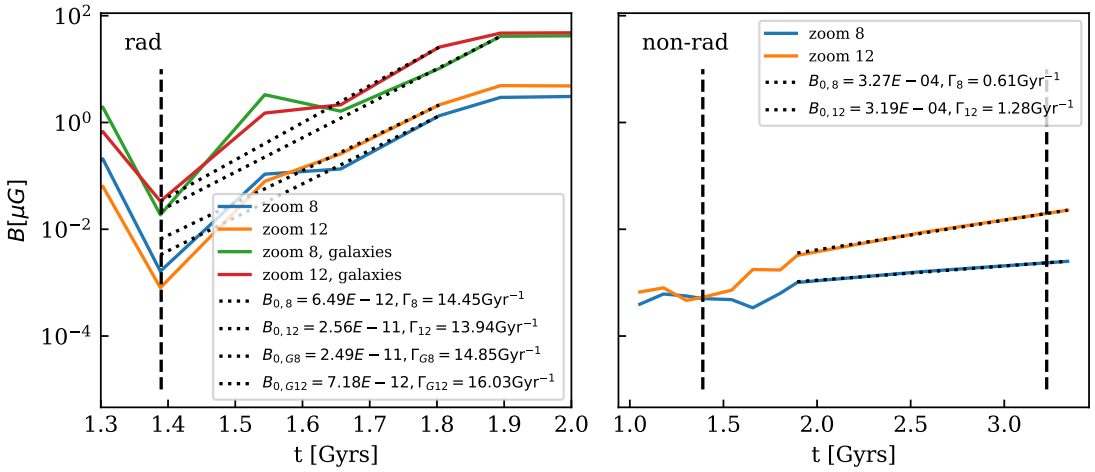

Figure 16: Zoom in from figure 15 of the central $R < 0.25 \cdot R_{200}$ into the region between merger 1 at $z = 4.5$, corresponding to $t = 1.4$Gyrs (indicated with vertical black line) and $t = 1.4$Gyrs (left panel). The right panel is a zoom in between merger 1 and merger 2 at $z = 2$, corresponding to $t = 3.2$Gyrs (second vertical black line). We show the volume weighted root mean square of the magnetic field in the radiative run (on the left) and in the non-radiative run on the right. We fit the growth rates $B = B_0 \cdot \exp \Gamma \cdot t$ (equation 49) to the zoom8 run, the zoom12 run and the star forming regions (galaxies) in the zoom8 and zoom12 run.

is associated with star formation, thus we analyse the effects of merging galaxies in the radiative run. In figure 15, we identify 2 mergers at $z = 4.5$ and $z = 2$. In figure 17, we show the magnetic field strength and the metallicity evolving with redshift for the radiative run, not only in the main cluster, but also in the merging objects. Metallicity is a tracer for stellar activity, as all metals are created in stars. We show the gas values of the high resolution region $4 \cdot R_{200}$ and indicated in black, dashed lines, $1/4 \cdot R_{200}$ and R_{200}.

The merging objects appear in the high resolution region and orbit the cluster for some time, before they merge into the cluster. At low redshifts, $z < 3$, the merging objects bring their own high magnetic field and high metallicity gas. We see that what we identify as merger 2 is in fact a series of smaller merging objects. Afterwards, smaller and bigger mergers occur frequently. The virial radius (outer dashed line) grows with each merger. The mergers contribute in two different ways to the magnetic field evolution: First, the merging objects bring their own metal and magnetic field (which has comparable field strengths to the magnetic field in the ICM of the main cluster) enriched gas to pollute the main cluster. Secondary, the mergers constantly inject new turbulence, which can prevent the magnetic field from decaying.

At high redshift, no merging objects are visible. What we identify as merger 1 at $z = 4.5$, is not visible in the magnetic field plot and only weakly visible in the metallicity plot. In the merging objects, the magnetic field starts to grow shortly after the first merger. This coincides with the time that the magnetic field in the cluster starts to grow. We conclude that the same mechanism that grows the cluster magnetic field in the second phase, also grows the field in the merging objects. Essentially, merging clusters have their own BCG that is able to amplify magnetic fields efficiently. The metallicity starts to grow slightly earlier in the merging objects. Stars in the BCG explode as SN, enrich the ICM with metals and add turbulence to the gas. This amplifies the magnetic field with a short timelag.

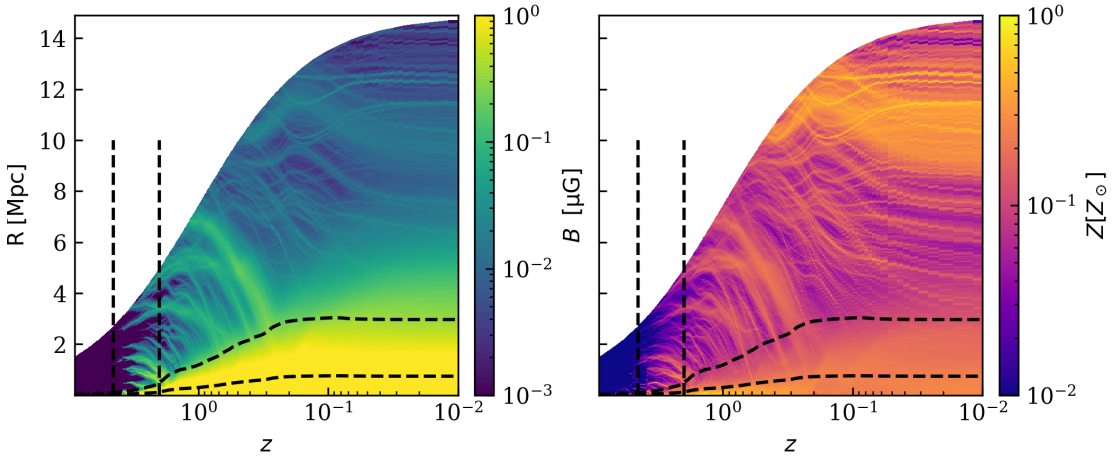

Figure 17: Timeseries of the radiative run for radially averaged magnetic field strength (left) and metallicity (right). The protocluster collapses at $z = 9.5$. We show the high resolution region $4 \cdot R_{200}$. The virial radius R_{200} and $1/4 \cdot R_{200}$ are indicated with two black, dashed lines. The vertical black, dashed lines indicate two mergers at $z = 4.5$ and $z = 2$.

3.3.6 Discussion

Magnetic Field Evolution and Growth Rates

It is only limited possible to compare our findings to observations. Galaxy clusters are extremely rare objects. As discussed in section 2.3.1, observing magnetic fields can be only done indirectly and requires knowledge about other quantities, such as densities, sizes, or about the nature of cosmic rays in this cluster. As our results are interesting in the redshift regime $9.5 < z < 3.5$, it is nearly impossible to know about these quantities. Additionally, observing high redshift clusters in general is hard, as galaxy cluster are the latest steps in structure formation and only started to form recently (see section 2.1). Thus, we will focus on comparing our results to the findings of other simulations.

Despite using zoom-in techniques, it is difficult to simulate small scale effects, such as single SN or AGN jets, in galaxy clusters properly, which would be necessary to more realistically model small-scale turbulence. Projects for simulating single SN (Gutcke et al., 2021) and AGN jets (Weinberger et al., 2022) in cosmological simulations are in development. The efficiency of the turbulent dynamo to turn turbulent energy into kinetic energy, is highly dependent on the resolution. But how much resolution is sufficient to simulate a dynamo? The fact that our magnetic field grows exponentially (see section 3.3.4) is an indicator that we can resolve a dynamo. In section 3.3.4, we have shown the resolution dependence on the growth rates of the magnetic field strength. For the radiative run, these are approximately the same in the zoom8 and zoom12 run. In the non-radiative run, they differ by more than a factor of 2. This shows: without radiative physics, a higher resolution yields a better resolved dynamo and enables thus a faster growth of the magnetic field; including radiative physics enables to lower the resolution and grow a magnetic field fast. It converges already at moderate resolution (zoom8). In order to investigate this further, we want to run a zoom24 radiative and non-radiative simulation. We also run a zoom4 simulation, but did not show it here, as the magnetic field is not converged.

Nevertheless, the numerical Reynolds number is dependent on the resolution. We compare our Reynolds number to observational findings. In the ICM, typical Reynolds numbers are Re $\sim$ 100 (Cho, 2015), which lies at the same order of magnitude like our findings. Roediger et al. (2013) highlight the importance to differentiate between magnetic and normal Reynolds Number (equations 46 and 55). A low resistivity can give high magnetic Reynolds numbers, if the viscosity is lower. Also for low Reynolds numbers in the ICM that were found Re $\sim$ 50, locally extremely high magnetic Reynolds Numbers are possible $\mathrm{Re_m} \sim 10^{10}$ (Roediger et al., 2013). A high magnetic Reynolds number, but low normal Reynolds number would yield a high Prandtl number (equation 47), which allows the magnetic field to grow efficiently on the very small scales. In our simulation, Pm $\approx$ 1, as both, numerical resistivity and viscosity are dependent on the cell sizes, which makes our setup very different to reality. Nevertheless, the fact that the growth rates in the radiative run are resolution independent shows that the effect of limited resolution on developing a sufficient dynamo, can be circumvented.

Now we compare our simulation against the findings of other groups that perform similar simulations. Marinacci et al. (2015) have a setup similar to ours, only that they analyse a cosmological box, instead of a zoom-in simulation. They run cosmological MHD simulations, where they compare an adiabatic run to a run, where they include radiative physics. They also perform the simulation for 2 different resolution levels. (As they performed the simulation almost 10 years ago though, their cosmological box is smaller by a factor of 10, only $100/h$ Mpc. Also for their complete simulation box, they have a resolution of 256^3 and 512^3 particles, while we have 425^3 particles in the high resolution region only. Their resolution would correspond to a zoom5 in our simulation.). It is to be noted that they investigate the magnetic field in the whole cosmological box and not only in selected halos. They find the strongest magnetic field to be 100μG in the radiative run in the high density regions. This roughly coincides with the values in our star forming regions. In their non-radiative run, they only reach field strengths of $10^{-2}\mu$G, which is three orders of magnitude below what we find in our non-radiative run. This shows how highly resolution dependent the growth of the magnetic field by (potentially) only the dynamo acting in the ICM is. They find that the magnetic field evolution at high redshift is very similar in both runs and is dominated by the expansion of the universe. While we also see the main effects in the early phase caused by the expansion of the universe, our radiative and non-radiative runs differ. In the radiative run, we see a dilution of the magnetic field on top of the effects of expansion, which is potentially caused by UV heating or primordial heating (as discussed in section 3.3.3). In the simulations of Marinacci et al. (2015), their magnetic field amplification for both setups starts at $z \approx 3$, where structure formation begins and injects turbulence. In our case, the collapse of the protocluster (coming with an increase of the magnetic field) is happening already at $z = 9.5$, the first main merger that inject turbulence occurs at $z = 4.5$, which is also earlier, compared to their simulation. These differences could be explained with the fact that we are looking at one of the most massive halos from our simulation (that collapses early and experiences lots of mergers), while they make statements about their whole cosmological box. The same explanations also hold, regarding their findings that the magnetic field is saturated at $z = 2$ in the radiative run, while our magnetic field in the radiative run is saturated already at $z = 3.5$. In their non-radiative run, their magnetic field is not saturated at $z = 0$, while this happens at $z = 1$ in our case. This shows again the resolution dependence of the dynamo efficiency in case of neglecting radiative physics. Their growth rates are $\Gamma = 0.14\mathrm{Gyr}^{-1}$ in the lower resolution radiative run and $\Gamma = 0.23\mathrm{Gyr}^{-1}$ in the high resolution radiative run. The growth rate in our radiative simulation was found to be $\Gamma \approx 14\mathrm{Gyr}^{-1}$, which is

about a factor of 60 higher. Reason is the lower resolution as well as the fact that they are looking at the whole cosmological box, while we are looking at a massive halo with a better resolution and where lots of radiative physics actually take place (this is not the case in cosmological voids for example).

Roh et al. (2019) simulate an isolated cluster without radiative physics. Interactions with the environment are computed separately and inforced. They have the same resolution, compared to our zoom12 run with 1024^3 particles. They find that a dynamo can amplify small seed fields to $\sim \mu$G within approximately the age of the universe. This is slower, compared to our findings in the non-radiative run, where our field is saturated already at $z = 1$. Important here is to keep in mind that they do not simulate mergers (which are the main reason for turbulence injection). As they have even smaller cell sizes, compared to our non-radiative run (they have constant cell sizes of 3.9kpc), a possible explanation would be that they underestimate the amount of turbulence that merger would inject. They find 2 exponential growth regimes: the first one at an age of $0 - 0.5$Gyrs and the second one at an age of $0.5 - 5$Gyrs. This is corresponding to our findings that there are two different growth phases in the non-radiative run. While the origin of those two different phases remains unknown in Roh et al. (2019), our assumption is that it is caused by the two different kinds of mergers. Their first phase has a higher exponent, compared to the second growth phase though, while it is vice versa in our case. They fit a growth rate to the second phase and find a rate of $\Gamma = 0.6\text{Gyr}^{-1}$ which is comparable to our zoom8 run growth rate.

Vazza et al. (2018) perform a zoom-in on a galaxy cluster within a cosmological simulation. They do not include radiative physics. They find at $z = 0$ fields of $\sim 2\mu$G within the inner Mpc^3 and a maximum value of $\sim 10\mu$G, which is comparable to our findings if we exclude the star forming regions. The magnetic field in the simulations of Vazza et al. (2018) starts to grow exponentially in the non-linear phase of the dynamo. They highlight the importance of the Reynolds number that they can resolve, as the non-linear phase can start earlier with a higher Reynolds number. They find a minimum Reynolds number of $\text{Re} \approx 380$ and a maximum Reynolds number of $\text{Re} \approx 1100$, dependent on the resolution. Though they reach higher Reynolds numbers, their magnetic field is saturated only at $z \approx 0.01$. They are not looking at the magnetic field in units of the virial radius that gets larger with time, but within a fixed physical volume, which could explain the low saturation redshift.

Steinwandel et al. (2022) perform a cosmological, non-radiative simulation. They find an exponential growth from the initial seed field value between $2 < z < 4$ to a value of 0.5μG in their low resolution run. They find differences for the high resolution runs. There, the magnetic field in the cluster peaks at around redshift $z = 2$ with a field strength of a few μG, after which the field strength decreases again and settles to $1 - 2\mu$G at $z = 0$ within the whole virial radius. They fit growth rates of $\Gamma = 0.7\text{Gyr}^{-1}$ to the low resolution run and $\Gamma = 0.15\text{Gyr}^{-1}$ to the high resolution run. They explain this with an unresolved and not properly working dynamo in the low resolution run. Interestingly, their exponential growth phase between $2 < z < 4$ is redshift-coinciding with our first exponential growth phase. Though their cluster has a comparable mass to our cluster of $2 \cdot 10^{15} M_\odot$, we reach higher growth rates and we also do not see the decrease of the magnetic field at low redshifts.

We also compare our initial seed field of comoving $B_0 = 10^{-14}$G to other people's simulations. Vazza et al. (2018), who perform non-radiative simulations, test different seed fields of

comoving 10^{-10}G and $3 \cdot 10^{-11}$G and find that the initial seed field does not have an impact on the further evolution. They state thought hat initial fields below comoving $3 \cdot 10^{-11}$G yield non-reliable results. Roh et al. (2019) test different initial magnetic field values of physical $10^{-4} - 10^{-9}$G and find that this yields different growth rates. The radiative simulations in Marinacci et al. (2015) explore using different seed fields and find that, at the beginning it plays a big role, but then they all catch up to reach the same field strengths. They test field strengths of comoving $B = 10^{-16} - 10^{-10}$G. We do not test different seed fields, but the conclusion is that it would not have big effects, at least in the radiative run.

But the discussion above shows that the initial seed field can have an influence on the growth rate in non-radiative simulations. An interesting way to view this is that the galaxies can lose their high magnetic field gas to the ICM, where it serves as higher initial magnetic seed field for a turbulent dynamo, enabling higher growth rates overall in the ICM. This could erase the effects that the original seed field has and explain the observed non-dependence of the seed field on the growth rate in the radiative run. Vazza et al. (2018) and Marinacci et al. (2015) make the same observations. In this context, also looking at the two grow regimes in our non-radiative run in figure 15 from $4.5 < z < 2$ and $2 < z <$ is interesting. Here, the exponential growth takes place (presumably caused by the dynamo). The first growth phase acts in such a way that it amplifies the magnetic field that it serves as giving a high seed field to the dynamo acting in the second phase. This could explain the increased exponent in the second growth phase.

We also compare our findings to the literature on magnetic field evolution in simulations of galaxies. As, in the radiative run, the magnetic field in the ICM is influenced by the high and fast evolving magnetic field in the galaxies, this is an indicator that we can also resolve the dynamo in our galaxies. A general remark is that our galaxies are within a galaxy cluster within a cosmological simulation, while simulations of galactic dynamos are mostly simulated in isolation. This yields a high difference in the resolution that we can afford. Pakmor et al. (2017) perform a cosmological zoom-in simulation of a galaxy. They find that the magnetic fields grows exponentially at early times due to the turbulent dynamo. They find a saturation around $2 < z < 3$ with a typical strength of 10-50μG. Our galaxies reach a constant magnetic field slightly earlier $z = 3.5$, but saturate at lower values $\approx 20\mu$G. Gent et al. (2023) solve the system of non ideal, compressible, non-adiabatic MHD equations with a model for SN-driven turbulence. They find an exponential growth within the first 100 Myrs and a saturation afterwards. They find resolution dependent growth rates of $529 - 475\text{Gyr}^{-1}$. This is much higher, compared to our growth rates in the galaxies (higher by a factor of ~ 500, but expected, as they can resolve cells at the pc scale). Pfrommer et al. (2022) simulate a galaxy where turbulence is injected via rotational body modes. They find saturation times of 0.3 Gyr for their higher mass halo and 1.5 Gyr for their lower mass halo. They measure exponential growth rates of $\Gamma = 22.4, 39.8, 48.0\text{Gyr}^{-1}$ for their low mass, intermediate mass and high mass galaxy. Comparable to our results, they also find that the magnetic field is first amplified via adiabatic compression and then a structure formation shock gives rise to the first dynamo. Later, turbulence gives rise to multiple dynamos acting on top of each other. Liu et al. (2022) also resolve a galactic dynamo. They find that strong galactic outflows enrich the intergalactic medium with its high magnetic field gas, which presumably is also the case in our radiative simulation.

Preprocessing

In figure 17, we have shown how merging substructures bring their already pre-enriched

gas to add it to the ICM. This process is referred to as 'preprocessing' (Hasan et al., 2023). There are different processes that can remove gas from galaxies. These include ram pressure stripping and galactic winds. Substructures that merge into the cluster were parts of other halos before the merger. In these halos, galaxies can already be quenched. Thus, the merging substructures add their pre-enriched gas to the cluster while merging. Galaxy clusters sit as knots in the cosmic web. They are the connection points of the filamentary structures. The density near the knots is higher in general. The high densities make galaxies within these environments easily subjects to ram pressure stripping (we discss this in more detail in section 3.8.1). Galaxies near clusters show a higher fraction of quenched gas, compared to field galaxies (A. Hou et al., 2014).

For high mass clusters ($M_{\rm cl} > 10^{14.5}{\rm M}_{\odot}$), the merging substructures consist predominantly of lower mass clusters, rather than single galaxies. In these merging subclusters, ram pressure stripping is very effective. For high mass clusters at low redshifts, most infalling galaxies (80 %) are therefore already stripped. The merging subclusters add their pre-enriched gas to the final cluster. The central AGN of the final cluster can also influence the gas stripping by heating the ICM in the cluster: galaxies at high virial radii ($R > 2 - 3R_{200}$) can lose their gas through interactions with the hot ICM (Martín-Navarro et al., 2019; Hasan et al., 2023). This is especially affecting low mass galaxies. For high mass galaxies, also their own central AGN can cause the quenching via strong galactic winds at low redshifts (Donnari et al., 2021). Major dependence of the environment on the state of the preprocessing seems to only play a larger role at lower redshifts ($z < 2$) though, where AGN feedback and merging of larger substructures becomes relevant (Hasan et al., 2023). However, we also see the effects of pre-enrichment in our simulated cluster. This shows how important it is to also simulate environmental effects, such as mergers and also the evolution of the merging objects.

Marinacci et al. (2015) who also perform a radiative cosmological simulation find that more massive halos contain a stronger magnetic field. They explain this with the fact that the most massive halos experience the most amount of mergers. These not only add more turbulence (which would be also applicable to the non-radiative run), but also the merging substructures add already boosted seed fields to the cluster, where the dynamo can work on top. In the merging substructures, the large seed fields can be reached due to gas compression and cooling. They are transported outwards by galactic feedback.

The conclusion is that pre-enrichment of merging substructures is also a relevant effect in our simulation. Especially at later times, our cluster grows together with the already highly magnetic field enriched gas of the merging objects. In order to simulate these effects, it is important to consider also the neighborhood of a simulated galaxy cluster.

3.4 Enstrophy Evolution with Time

The magnetic field evolution is tightly coupled to the turbulence evolution in the ICM (see section 2.3.3 about the small-scale dynamo). Turbulent kinetic energy can be converted into magnetic energy. In figure 18, we show the enstrophy evolution with redshift in the ICM. Enstrophy is a proxy for turbulence (see equation 23). We show the enstrophy evolution for the radiative run on the left and the evolution in the non-radiative run on the right. The different radial bins are indicated with the color scheme. We exclude the star forming regions in order to show only the enstrophy in the ICM. The merger at $z = 4.5$ and $z = 2$ that we identified in section 3.3.4 are indicated with the black vertical lines. Overall, the enstrophy is not higher in the ICM of the radiative run. The fact that there is turbulence, shows that a small-scale dynamo can potentially act in the ICM of

our simulated cluster.

After the collapse of the protocluster at $z = 9.5$, the enstrophy curve shows a sudden rise, when the collapse and structure formation shock injects a high amount of turbulence in both runs. Afterwards, the amount of turbulence remains approximately at the same level (see figure A.6 which shows a zoom-in on figure 18). Mergers constantly occur and inject new turbulent motions, as discussed in section 3.3.5. After merger 1 and merger 2, there is a small rise in the enstrophy curves. Interestingly, the enstrophy is highest for the central bin. This can be due to the following numerical effect. In order to compute the enstrophy, we compute the curl of the velocity field. This yields smaller values for bigger cells that are more likely to be found in the outskirts. In the center, the densities are highest (see section 3.2) and thus the cells are the smallest, which can yield high enstrophy values, if there is turbulence in the center. The conclusion is that the amount of turbulence in the radiative run is in general not higher, compared to the non-radiative run. The high magnetic field gas that is produced in the galaxies though can act as adding higher seed fields for a dynamo (as discussed in section 3.3.6). This could explain the steeper rise of the magnetic field values (as shown in figure 15) in the radiative run, despite that it does not have a higher amount of turbulence in the ICM. Multiple dynamos with high initial fields, acting on top of each other can explain this observation.

Comparing the radiative and the non-radiative run, we see that the most central bin shows a higher level of turbulence in the radiative run at high redshift $9.5 < z < 2$. At these high redshift, turbulence in the center is dominated by SN that explode in the BCG. The central enstrophy increase in the time between the collapse and the first merger, $9.5 < z < 4.5$ coincides with a central steep increase of the magnetic field strength in the center (see the bump in figure 15). The conclusion is that strong magnetic fields are generated in the BCG, where it is affected by cooling (higher densities) and a high amount of turbulence. This makes a dynamo act very efficiently. The small eddy turnover rates in the center, associated to turbulent small cells, can enable a fast growth of the magnetic field. The high magnetic field gas escapes the BCG to pollute the central ICM. It can use the already pre-enriched high magnetic field gas as high initial field values. The AGN is unlikely to add a high amount of turbulence at these high redshift. At this time, the central AGN is in quasar mode (see figure A.3) and adds energy in form of radiation to surrounding cells, rather than turbulence that also acts at larger radii.

At the beginning of the simulation, $z > 9.5$, the enstrophy in the radiative and in the non-radiative run behaves differently. In the radiative run, the enstrophy stays constant. In the non-radiative run, the simulation starts with an initially higher value and decreases. This could be associated to the magnetic field strength also behaving differently in the radiative and non-radiative run, at this time. This needs to be investigated further.

Although the central AGN is in radio mode at later redshifts (see figure A.3), figure 18 shows that the level of enstrophy is not enhanced in the radiative run, not even in the central bin.

3.4.1 Discussion

Turbulence in the ICM is not well understood, which makes it complicated to compare our findings to observational counterparts (Rudnick, 2019). Especially high redshift observations (the steep magnetic field amplification in the radiative run happens at $9.5 < z < 3.5$) of turbulence in the ICM are currently not possible to take. Thus, we compare our findings to the findings of other people's simulations. A general remark on the resolution dependence

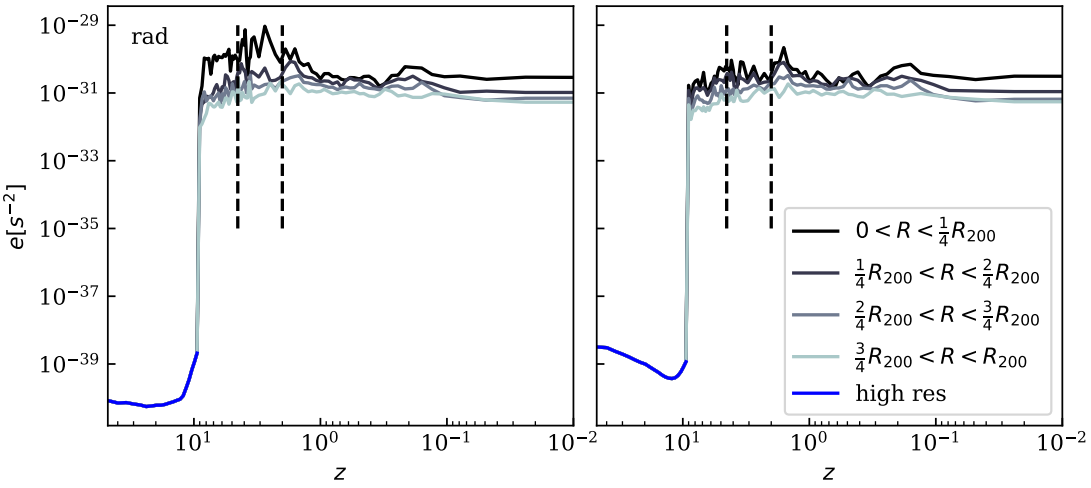

Figure 18: The mass weighted enstrophy evolution with time (see equation 23). We show different radial bins in units of the virial radius $R_{200}(z)$, indicated with the color scheme. The radiative run is shown on the left and the non-radiative run is shown on the right. The star forming regions are excluded from the ICM. Before the collapse of the protocluster at $z = 9.5$, we use the complete high resolution region to compute the enstrophy.

of turbulence is that turbulence is a multi scale problem, ranging from the injection scales (which can be at the order of the virial radius in case of larger merger) to the viscous scales (which in our inviscous simulations are determined by the cell sizes). Thus, high resolution regions (such as in the center of the cluster, where the density is high) are able to better resolve small scale turbulence. Physically, we can justify this with the fact that outer scale turbulence is driven by merger, that have a large scale anyways and where a worse resolution, compared to the high density regions, is still able to resolve the large scale turbulence properly. Larger cells come wih a higher amount of numerical viscosity (see equation 54). Also this is justified physically, as viscosity in low density regions is also higher, because of the larger particle mean free path (equation 8).

Bennett & Sijacki (2022) suggest, that merger inject the biggest amount of turbulence to the ICM, compared to oher contributors, such as AGN or stellar feedback. They perform simulations and find, that infalling substructures add a large amount of turbulence. This turbulence is created in the wake of the shocks. Also Cassano & Brunetti (2005) and Biffi et al. (2022) investigate the effect of mergers on creating turbulence and have similar findings. Additionally, they find, that the fraction of injected turbulence is highest for the largest clusters (as they experience more mergers). This is matching with our findings that structure formation processes are the main reason for turbulence in the ICM. As the cluster that we analyse here is the fifth most massive one from our simulation, we assume that , if we were to simulate a lower mass cluster, the enstrophy would probably be lower, as they also experience less mergers.

It is under debate how much of the AGN energy can be converted into turbulent kinetic energy. Hitomi Collaboration (2016) used X-ray observations of the center of the Perseus cluster to find that only 4 % of the internal energy of bubbles injected by radio mode AGN is converted to turbulent kinetic energy. Zhang, Zhuravleva, et al. (2022), who study simulations, in contrast find that about 50 % of the AGN energy can be injected into turbulence. Comparing this to our findings, we don't see an enhanced level of enstrophy (which is a proxy for turbulence) in the central ICM at lower redshifts. This is comparable to the findings of Hitomi Collaboration (2016), who also see a low level of turbulence in

the center of Perseus cluster. The high efficiency of internal energy of AGN bubbles to be converted into turbulent energy, found by Zhang, Zhuravleva, et al. (2022) could be explained by looking at how turbulence is inferred from observations (turbulence in form of solenoidal, bulk and compressible motions) and how it is injected in simulations (often explicitly injected in solenoidal form).

The Hitomi Collaboration (2016) and Zhang, Zhuravleva, et al. (2022) state, that the turbulence can spread over the whole ICM and mix ICM from the central regions with intermediate region ICM. The AGN, galaxies and merger induced turbulence can start to interact. The peak of the turbulence is still in the outskirts though, where it is associated to merger. In the context of this thesis, this is interesting as turbulence can mix the high magnetic field gas, that is first created in the center, with lower magnetic field ICM that is located at higher radii. Thus, turbulence can serve as a mechanism to grow a, on cluster scales, more homogeneous and stronger magnetic field.

Wittor et al. (2017) also investigate the enstrophy evolution in a simulated ICM. They trace the effects of single encounters by injecting tracer particles into merging substructures. Their simulated clusters are in the mass range of $0.5\text{-}3.3 \cdot 10^{14} M_{\odot}$, roughly one order of magnitude less compared to the cluster, we analyse in this thesis. They only study the enstrophy evolution for $0 < z < 1$. Similar to our findings, they find a mean enstrophy level of $10^{-32}\mathrm{s}^{-2}$ in the cluster and excesses from this, after mergers occur. This is lower by roughly one order of magnitude, compared to our findings. This difference is not unexpected as larger clusters experience more mergers, which drives more turbulence. Wittor et al. (2017) find that peaks in enstrophy appear corresponding to merger. Very high peaks are caused by major mergers or by turbulence that is interacting with each other (tracer particles from different substructures meet). Comparing this to our findings, it explains the, in general, slightly higher level of enstrophy in our cluster. Mergers occur frequently (see section 3.3.5) and turbulence injected by an earlier merger can interact with turbulence injected by a merger at later times. Wittor et al. (2017) also study the ability of turbulence to be converted into magnetic energy (we study this in more detail in section 3.7). They emphasize that the magnetic field growth becomes slower soon after the turbulence subsides. The reason is that magnetic field dissipation starts to set in, as soon as there is no new energy supply. Comparing this to our findings that the magnetic field does not decay, shows that a high level of turbulence, caused by merger, can help to sustain a magnetic field. Vallés-Pérez et al. (2021) have comparable findings.

Valdarnini (2019) study the turbulence in a setup, similar to ours. They simulate radiative and non-radiative clusters. Matching with other findings, as mentioned above, they find that the largest amount of turbulence is injected by merger. Also matching is that they find that a higher amount of turbulence is associated to a higher merger rate and thus to higher mass clusters. What is interesting in their findings is the scale-separation of turbulence. For the non-radiative clusters, they find an excess of the turbulent energy at small wavenumber scales, close to the injection scale. For their radiative run, they find that a large fraction of the total power is at the smallest scales. They attribute this to the development of a dense core (caused by cooling). The core can interact with surrounding turbulence and triggers gas instabilities that, in return cause turbulence in the dense core region. Comparing this to our findings, we also see an enhanced level of turbulence in the center in the radiative run. We associate this to star formation triggered turbulence though (we investigate this further in section 3.8.2). We do not perform a power spectrum analysis and it is unclear if we can develop instabilities caused by turbulent interactions with a cold core.

A general remark is that enstrophy is not an ideal measure for turbulence. The values are biased towards the denser regions. Also flow- and bulk motions will be considered. In general, the eddy turnover times are dependent on the eddy sizes, which we cannot directly monitor. A more sophisticated way to study the turbulence in rotational form is to use a filtering technique, similar to Valdarnini (2019), where they consider different coherence lengths of the velocity field. Apart from that, not only solenoidal motions are responsible for amplifying magnetic fields. Schober et al. (2013) state that also compressible motions can amplify magnetic fields, which we do not consider at all in our analysis.

3.5 Magnetic Field and Metallicity Radial Profiles

Metals in the ICM are a tracer for stellar activities in galaxies, such as SN induced turbulence. As shown in figure 15, galaxies grow a stronger magnetic field in a shorter period of time. Especially at high redshift $9.5 > z > 4.5$, the magnetic field evolution in the radiative run is dominated by the center (as discussed in section 3.3), where the BCG is active. We compare radial magnetic field profiles against metallicity profiles for different redshifts in figure 19. Additionally, we compare the magnetic field profiles in the radiative and non-radiative run.

We start by comparing the magnetic field radial profiles in the radiative run (upper panel) to the non-radiative ones (lower panel). At $z = 0$, both profiles are very similar. The progenitor evolution of the radial magnetic field differs among the two simulations though. In the non-radiative simulation, the magnetic field strength rises smoothly and almost homogeneous at all radii and across the whole redshift range. This picture is different in the radiative simulation. At higher redshift, there is a steep gradient in the radial magnetic field profile. First, the magnetic field rises steeply in the center, but stays rather low at the outer radii. Then, at redshifts $4 > z > 2$, the radial distribution becomes more smooth: the central values at these redshifts overshoot the central values at $z = 0$, but also in the outskirts, the magnetic field strength is higher. Then, towards $z = 0$, the central values decrease again, while the values in the outskirts stay constant. The radial profile stays constant for the two latest redshift calculations $z = 1$ and $z = 0$.

Now we compare the radiative magnetic field profiles to the metallicity profiles. Both show a similar morphology change with redshift. Also the metallicity profiles first reach very high values in the center, such that the higher redshifts overshoot the profile in the center at $z = 0$. Towards lower redshift, the metallicity in the outskirts rises at the expense of the central metallicity, which decreases. Also here, there is no evolution between the last two redshifts. What is the physical explanation for this? At high redshift, the BCG has a high SN rate. This pollutes the central regions with metals. It also injects turbulence to the central ICM, that can be converted into magnetic energy. Additionally, larger merger that start to occur frequently from $z = 4.5$ on, add a high amount of turbulence to the ICM that mixes the gas from the center with higher radii gas (as discussed in section 3.4.1). This lowers the high central values and increases the values at larger radii. Merger not only mix the ICM, they also grow the cluster with their already metal and magnetic field pre-enriched gas (see section 3.3.5). The similarity between the metallicity and magnetic field profile emphasizes how closely related the magnetic field growth in the ICM is to galactic activity. The scatter at larger radii in the magnetic field and metallicity profiles in the radiative run is due to the accretion of substructures that are already pre-eriched.

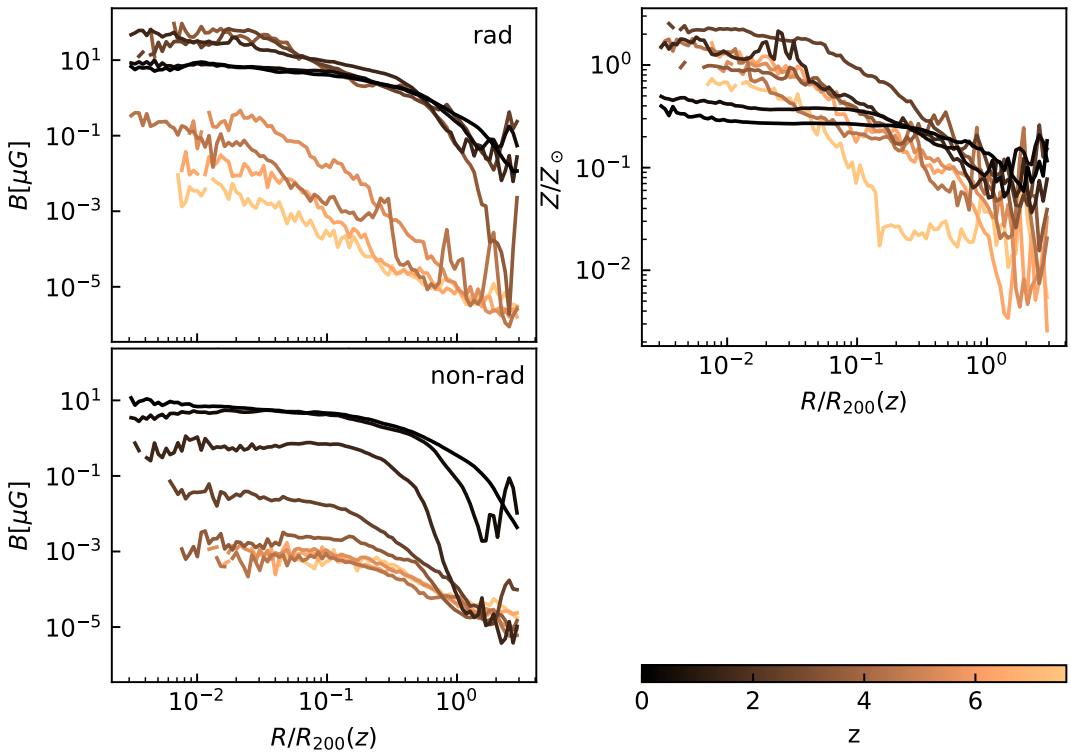

Figure 19: The volume averaged root mean square magnetic field strength as a function of radius (left panel) for the radiative (upper panel) and the non-radiative (lower panel) run. On the right, we show the mass weighted metallicity profiles. We show the profiles for 9 different redshift.

3.5.1 Discussion

For the metallicity, it is hard to compare our findings against observations, as this would require a high resolution spectral observation of the ICM. Simionescu et al. (2008) present an observation of the BCG (M87) of the Virgo cluster. In the galaxy, they find that the center is more enriched with metals, compared to the outer radii. Overall, the metal content in the galaxy is quite high (slightly more than solar metallicity; see their figure 10). Also beyond the half mass radius, the metal fraction is high and only decreases slowly. Simionescu et al. (2008) associate the metal spread to AGN activity, where radio lobes carry the high metallicity galactic gas to the surrounding ICM. Comparing this to our findings, we emphasize that we are looking at the high redshift regime $9.5 > z > 4.5$, where we associate the metallicity and magnetic field enrichment to the central galaxy. In this redshift regime, we associate the mixing of high metallicity gas from the BCG to the central ICM to SN explosions that can cause galactic winds that drive out the gas. The AGN is not in the radio mode at these high redshift (see figure A.3) and cannot inject radio bubbles.

We compare our metallicity profile findings to the findings of other simulations. Vogelsberger et al. (2018) perform simulations of the ICM, where they analyse the metal content and its origin. Their galaxy formation module is very similar to ours, only that they treat their wind particles and AGN bubbles slightly different. They find that, at higher redshift, there is a steep gradient in the metallicity profiles. This is due to the contribution of high mass star SN in the center. Later, the radial metallicity distribution becomes more

homogeneous. Especially the outer profile becomes more flat. They attribute this to SN of lower mass stars that are occurring at all radii in the cluster. They find that, from $z = 2$ on, the metallicity profile does not change anymore. They attribute this to mergers that add pre-enriched gas to the ICM. This gas has approximately the same metallicity like the ICM in the main cluster. Comparing this to our findings, we see exactly the same radial metallicity morphology evolution with redshift. We also associate the high metal content in the center at high redshift to the SN in the central galaxies. In contrast to our findings though, Vogelsberger et al. (2018) associate the flattening of the metallicity profiles at lower redshift to the ongoing activity of lower mass star SN. We do not trace the feedback of SN and can therefore not verify or deny this definitely. So far, we addressed this to the activity of mergers , that mix central and high radii ICM. There are arguments for both sides (SN and mergers). We justify the merger hypothesis with four arguments. 1) the frequent merger activity and the induced metal enrichment due to pre-processing (see section **??**). 2) the large amount of injected turbulence after a merger (see section 3.4) that can mix central ICM with ICM at larger radii. 3) the positive correlation between magnetic field strength and metallicity in the ICM, appearing at lower redshift ($z <= 2$) (see figure 20c, we discuss this later in section 3.6.3). 4) the comparably low high mass star SN activity at lower redshift ($z <= 2$) (see figure 26, we discuss this later in section 3.8.2). These indicators point towards the picture that mergers dilute the central high metallicity values. On the other hand, figure 26 shows that there is still some high mass star SN activity going on at lower redshift. Additionally, figure 26 only shows the relative abundance of the lhigh mass star SN (local wind,as discussed in section 2.4.3). For the non-local feedback, caused by lower mass stars, there is a time delay function (as was discussed in section 2.4.3). Vogelsberger et al. (2018) use a similar stellar evolution and feedback model, compared to ours. It is possible thus, that lower mass star SN contribute to the flattening of the metallicity profile.

Also Fabjan et al. (2010) investigate the metal distribution in simulations of the ICM, including AGN and SN feedback. They find that AGN feedback reduces the stellar feedback for $z < 4$ in the BCG. They also find a homogeneous metal distribution at lower redshift. They associate this though to AGN activity that can occur at all radii and remove high metallicity gas from galaxies. Comparing this to our findings, we also see a decrease in the central metallicity profiles from $z \sim 4$ on. This adds to the discussion in the previous paragraph. AGN feedback (according to Fabjan et al. 2010), low mass star SN (according to Vogelsberger et al. (2018)) or merger activity (as discussed in section 3.4.1) can cause the homogeneous metal distribution at lower redshift as a function of radius. However, the AGN and SN hypothesis would come with an increased level of turbulence at all radii, compared to the non-radiative simulation, which wo do not see (as shown in figure 18). Nevertheless, we would need to investigate the origin of these metals in detail in order to make more sophisticated statements..

A general remark is that SN, as well as AGN feedback are highly dependent on the underlying subgrid models. The stellar formation model is biased, as, for example we do not resolve single stars, but single stellar populations instead. The SN rate of low mass stars is basically unknown in such a single stellar population. Also, our galaxy formation module uses the same IMF throughout the whole simulation. A more realistic setup would take into account the evolution in the star formation with time (as discussed in section 2.4.2). Regarding the AGN module, the exact physics behind AGN feedback is not well understood yet. Often, star formation and AGN modules are set up such that they reproduce specific observables (in our case, the AGN module to solve the cooling flow problem in galaxy clusters, see Heinrich et al. 2021; the stellar formation module is set up

such that is reproduces the metal content in nearby galaxies as discussed in section 2.4.2). Especially at high redshift, these modules come with a high degree of uncertainty.

3.6 Magnetic Field Phase Space Diagrams

The magnetic field evolution is highly dependent on the plasma density, as well as on the amount of enstrophy (as discussed in sections 2.2.3 and 2.3.3). In section 3.3 we find that the magnetic field growth in the ICM is tightly correlated with the magnetic field evolution in the star forming regions. We want to answer the following questions: what influences the magnetic field growth in the galaxies? What influences the magnetic field growth in the ICM? To answer these questions, we analyse the magnetic field, mass weighted histograms in figure 20. We show a density-magnetic field phase space diagram, an enstrophy-magnetic field phase space diagram and a metallicity-magnetic field phase space diagram. We show four different redshifts: $z = 6.2, 4.0, 2.0, 0.0$ to indicate: first, $z = 6.2$ as the redshift between the collapse of the protocluster and merger1. At which, in the radiative run, the magnetic field grows in the central galaxy, while the non-radiative run magnetic field remains constant. Secondary, $z = 4.0$ as the redshift between merger1 and merger2. Here, in the radiative run, the magnetic field rises exponentially and in the non-radiative run, the magnetic field experiences its first exponential growth phase. Then, $z = 2.0$ as the redshift after the second merger. There, in the radiative run, the magnetic field is saturated and in the non-radiative run, it experiences the second exponential growth. Last, $z = 0.0$ as the redshift, where both simulations, radiative and non-radiative, are in the saturated regime. The color schemes indicate the mass, contained within each bin over the total mass of gas in the cluster over the area of the diagram. The star forming regions are indicated with red density contour lines. There is a cut-off at the lower densities of the star forming regions in the density-magnetic field phase space diagram in figure 20a. This is because of the density threshold that determines, if a cell is labeled as star forming or not (as discussed in section 2.4.3).

3.6.1 Magnetic Field - Density Phase Space Diagrams

We start with analysing the magnetic field-density phase space diagram in figure 20a. We show histograms for the radiative run in the upper row and for the non-radiative run in the lower row. We compare against the relation for adiabatic compression $B \propto \rho^{2/3}$ (equation 16) and the relation indicating a self-gravitating system with a saturated dynamo scaling $B \propto \rho^{1/2}$ (equation 52), shown as black, dashed lines. In the radiative run, the ICM deviates from the adiabatic compression scaling already at $z = 6.2$. Large parts of the ICM are star forming. The star forming regions sit at the high magnetic field and high density end. The star forming regions and the ICM close to them in the histogram seem to follow the same power law: it is steeper, compared to the 2/3 scaling. Only the low magnetic field and low density end deviates a bit. It comes with slightly lower magnetic field values. Speaking in physical terms, it confirms the picture that we have: the magnetic field growth is dominated by the star forming regions in the center. These pollute the surrounding ICM. The high magnetic field gas can expand into the virial radius R_{200}, where the field strengths decrease with increasing radius. The low magnetic field, low density end, that contains a large fraction of the total mass (indicated with the yellowish color) is presumably ICM that did not interact with the star forming region gas yet. It is to be kept in mind that the plasma in the center is still subject to compression caused by gravity and cooling (independent on dynamo action). Looking at the non-radiative run for $z = 6.2$, the distribution of cells spans a more narrow region in the phase space diagram. It follows roughly the 2/3 scaling, indicating that the plasma is mainly affected

by adiabatic compression.

In the radiative, $z = 4.0$ panel, the lower end of the distribution follows roughly the 2/3

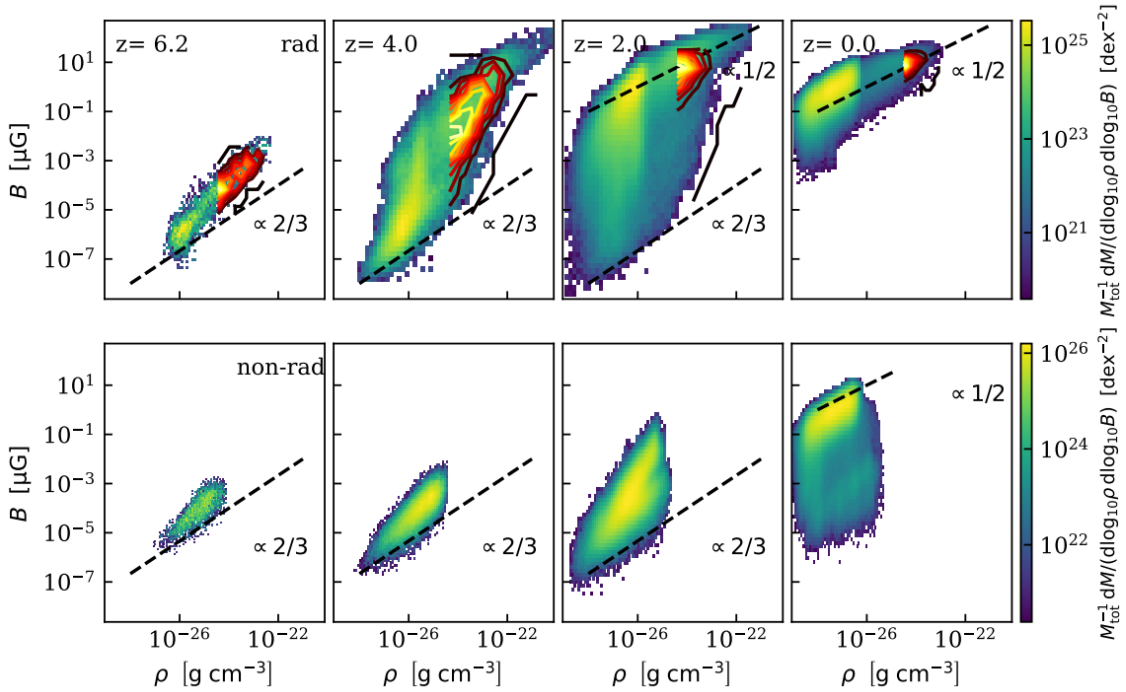

(a) Magnetic field-density mass weighted histogram. We indicate the adiabatic compression relation $B \propto \rho^{2/3}$ (equation 16) and the relation indicating a self-gravitating system with a saturated dynamo scaling $B \propto \rho^{1/2}$ (equation 52 from S. Xu & Lazarian 2020) with black, dashed lines.

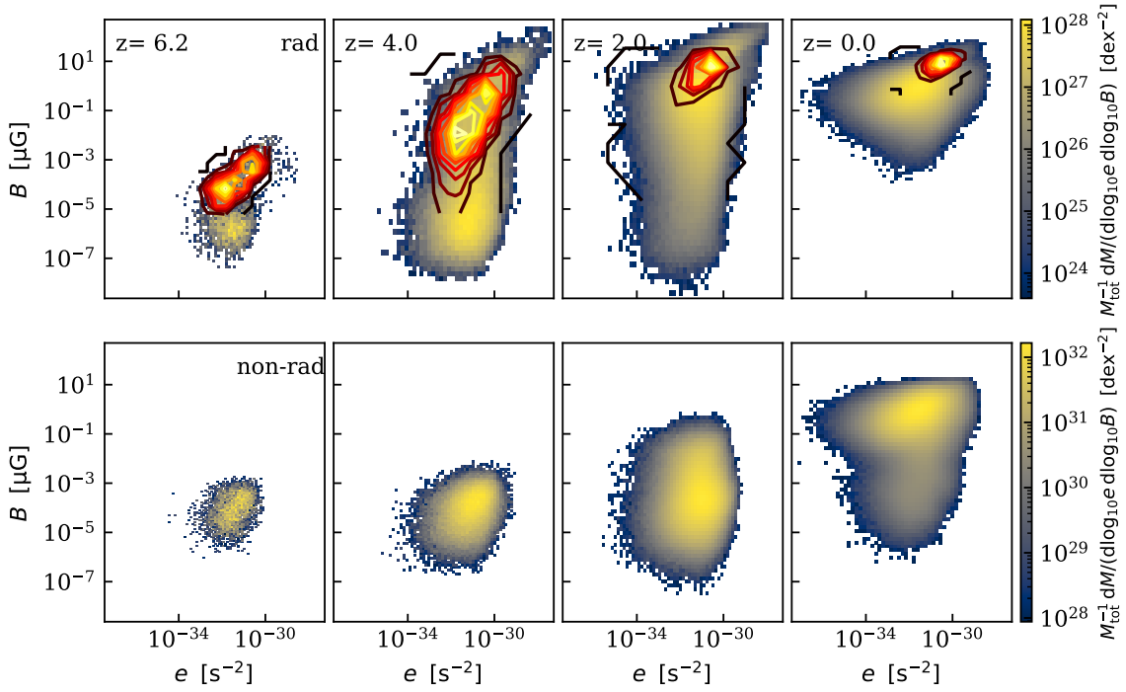

(b) Magnetic field-enstrophy mass weighted histogram.

Figure 20

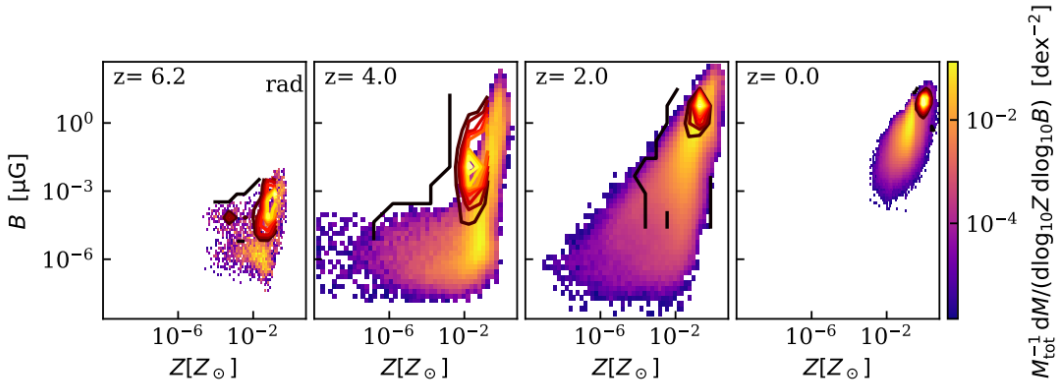

(c) Magnetic field, metallicity mass weighted histogram for the radiative run.

Figure 20: Magnetic field mass weighted density histograms. We show the density (figure a), the enstrophy (figure b) and the metallicity (figure c). We show 4 different redshifts: $z = 6.2, 4.0, 2.0, 0.0$. We show the star forming regions, indicated with red density contour lines. Light colors correspond to high densities and darker colors to less dense regions.

scaling. The remaining cells are separated into two different distributions: one that is following approximately the power law from the $z = 6.2$ distribution and the other one following a steeper power law. The star forming regions cover the high magnetic field ends of both distributions, interestingly. A high fraction of the mass is sitting at the fork to these two branches. A physical interpretation is that the magnetic field in most parts of the ICM grows non-adiabatically. The highest magnetic field values are presumably reached in the central galaxy. The strong density dependence is not so pronounced anymore. It looks like there are different effects overlying, each coming with a different density scaling. We can make assumptions: the star forming regions are split into these 2 different distributions. One is presumably the central galaxy. The other one consists of presumably galaxies that just entered the cluster. While the central galaxy has formed already very early and has already experienced non-adiabatic magnetic field growth, the newly entered galaxies start to undergo the same process that grows the magnetic field in the central galaxy in the $z = 6.2$ plot. This would explain the similar densities, but different magnetic field strengths in the star forming regions. The strong magnetic field gas from the star forming regions can expand from the galaxies and get mixed with the ICM. Additionally, a dynamo acting in the ICM can further amplify the magnetic field, as at $z = 4.5$ the first larger merger occurs.

In non-radiative, $z = 4.0$ panel, we see how the distribution slowly starts to deviate from the $B \propto \rho^{2/3}$ scaling. At this redshift, the ICM in the non-radiative run experiences its first growth phase. This is corresponding to an steeper scaling of the magnetic field with the density. Presumably, this is how the dynamo manifests. Again, the distribution covers a more narrow area in the histogram, compared to the radiative run. This is because of the lack of cooling that would allow for lower densities. Another reason is that, in contrast to the radiative run, there is only one channel that allows the magnetic field to grow (namely the dynamo).

Now we analyse the radiative $z = 2$ panel. The lower end still follows approximately the indicated adiabatic compression scaling. The lower density regions could be part of gas inside merging substructures, with a low amount of turbulence, such that the magnetic field could not grow strong in these substructures. In most parts of the ICM though, the magnetic field grows independent on density. This stretches over the complete low density

region, where the magnetic field rises almost vertically. The regions with the highest magnetic field strengths, vaguely follow the $B \propto \rho^{1/2}$ scaling, indicating a saturated dynamo. At $z = 2$, the magnetic field in the radiative run is in the saturated regime (see figure 15). A physical interpretation is that multiple galaxies, by now have grown their own strong magnetic field. These are in different stages of polluting the ICM with their gas. While some have already ejected gas at earlier times, others just start doing so. These galaxies can sit at any distances from the center. This makes the gas mixing and the resulting magnetic field strengths in the ICM very different. Apart from that, the cluster has experienced two major mergers so far that can mix gas with different densities and magnetic field strengths.

We analyse the $z = 2$ panel for the non-radiative run. Here, we can see how (presumably) different dynamos (in different stages) act on top of each other. Each comes with a different density scaling. The (presumably) dynamos are probably caused by merger1 and merger2. At this redshift, the magnetic field in the non-radiative run experiences its second growth phase (see figure 15). It manifests via a steeper scaling with the density, compared to the $z = 4.0$ panel. It is interesting that both distributions, in the radiative and in the non-radiative run, follow on the low magnetic field end the adiabatic compression relation.

In the radiative, $z = 0$ panel, the contribution from adiabatic compression completely vanishes. The distribution roughly follows the $B \propto \rho^{1/2}$ scaling, indicating a saturated dynamo in the ICM at this redshift. At the low densities, there is a small bump below the $B \propto \rho^{1/2}$ scaling at lower magnetic field strengths. This could be attributed to regions in the outskirts that are not yet fully saturated. In the non-radiative run, most of the mass is also following the $B \propto \rho^{1/2}$ scaling. There is a large contribution from a weaker magnetic field distribution that is covering the whole density range though. It would be interesting to check, whether this contribution will disappear if we let the simulation run for longer time, or whether it will remain. If latter is the case, it could mean that the magnetic field decays faster than it can be generated in some areas. The low magnetic field distribution covers the whole density range though (so this would regard areas in the center and at the outskirts), which is interesting.

3.6.2 Magnetic Field - Enstrophy Phase Space Diagrams

Now we analyse the magnetic field-enstrophy phase space diagram, shown in figure 20b. In the non-radiative run, the distribution does not change much across the different redshifts. It becomes a bit more dynamical and spans over a larger area. This happens approximately symmetrically around the initial distribution at $z = 6.2$. Mergers inject turbulence. Turbulence, on the other hand decays very fast, as it is turned into heat or magnetic energy. This could explain the range in the enstrophy distribution that grows with time (and merger activity, presumably). Overall, there is no correlation between the magnetic field and the enstrophy.

How is this matching with the theory that a dynamo is acting in the ICM and converts turbulent energy (where we use enstrophy as proxy for turbulence) into magnetic energy? First of all, the level of enstrophy in the ICM is high in general (as discussed in section 3.4). Regions with a high magnetic field are turbulent, as well as regions with a low magnetic field. Secondary, turbulence is not turned to magnetic energy instantaneously. There is a time delay that spans over the time between the injection of turbulence to the time, the magnetic field is amplified efficiently. Turbulence on the injection scales decays to the viscous scales. Turbulence at all scales amplifies the magnetic field. Though this happens fastest at the viscous scales, also the large scale turbulence is converted into

magnetic energy, only slower. These effects yield a correlation between magnetic field and turbulence with different time delays and at different correlation scales. Additionally, enstrophy is not an ideal measure for turbulence (as discussed in section 3.4.1). It is biased towards the turbulent smaller cells. These three arguments (turbulence in the ICM is high in general, the time and scale separation and the non-ideal measurement of turbulence) can explain the apparent non-correlation between the enstrophy and the magnetic field in the non-radiative run.

Now we analyse the enstrophy-magnetic field relation in the radiative run. Here, we start by looking at the star forming regions. They have a higher level of enstrophy, compared to the ICM. What is also interesting is that, for the star forming regions, there is a correlation between magnetic field strength and enstrophy. The high enstrophy level in the star forming regions makes sense, as galaxies are high density regions. In case that they are additionally turbulent, this would yield high enstrophy values. In galaxies, turbulence is injected on small scales (predominantly by SN for $z > 2$). Small-scale turbulence can be converted to magnetic energy faster with the small-scale dynamo (Pakmor et al., 2017, 2020). This explains the correlation between magnetic field and enstrophy in the star forming regions. Additionally, the star forming regions are shielded from the ICM, as hey reside inside galaxies, such that large scale turbulence does not interact with the turbulence in the galaxies. The minimization of time separation between turbulence being converted into magnetic energy and the minimization of scale separation of turbulence could explain the enstrophy-magnetic field correlation in the star forming regions.

The level of enstrophy in the ICM in the radiative run, without the star forming regions, looks very comparable to the non-radiative run. This confirms our findings from section 3.4, showing no large differences between the enstrophy in the radiative and in the non-radiative run with redshift. The main reason for turbulence in the ICM are merger (as discussed in section 3.4.1). As both, the cluster in the radiative run and in the non-radiative run, are subject to merger, the enstrophy looks very comparable. The explanation for the apparent non-existence between a magnetic field-enstrophy correlation in the ICM is the same like for the non-radiative run (discussed in the paragraphs above).

It is interesting to compare the $z = 0$ panels of the radiative and the non-radiative simulation. In the non-radiative run, the distribution in the enstrophy-magnetic field plane seems to consist of two smaller distribution that are vertically aligned, where one comes with higher magnetic field values. The other comes with lower ones. In the radiative run, there is only one distribution, which is coinciding with the higher magnetic field values distribution in the non-radiative run. We already saw in the $z = 0$ non-radiative density panel in figure 20a that the dynamo in this simulation is probably not saturated yet. Thus, the two distributions in the magnetic field-enstrophy phase space diagram could show regions that are already saturated (the upper distribution) and regions that are not yet saturated (the lower distribution). As discussed in section 2.3.3, a saturated dynamo manifests in such a way that the magnetic field backreacts onto the ICM again and releases parts of the magnetic energy into turbulent energy again. This could explain a higher level of turbulence in regions that are magnetically saturated.

3.6.3 Magnetic Field - Metallicity Phase Space Diagrams

In figure 20c, we show the metallicity-magnetic field phase space diagram for the radiative run. Metallicity is a tracer for galactic activity, as the large amount of metals is produced in galaxies. By tracing the metals in the ICM, we can see how much of the high magnetic field and metal enriched gas from galaxies pollutes the ICM. We can also check, how it

affects the magnetic field in the ICM. Figure 20c shows that the high metallicity regions also come with a strong magnetic field. These are essentially the star forming regions at $z = 6.2$ and $z = 4$. At $z = 6.2$, the magnetic field growth is dominated by the central galaxy. This is also displayed here, as the central galaxy also has a higher metal content.

At $z = 4.0$, the star forming regions have grown a stronger magnetic field, which is displaced by the distribution wandering upwards in the phase space diagram. Also, this high metallicity gas starts to pollute the ICM, yielding higher metallicity values in the ICM. Below the star forming regions in the phase space diagram, a lot of mass is sitting in an area with a high metal fraction, but low magnetic field strengths. How can we explain this high metallicity, but low magnetic field gas? There are two possibilities. 1) the metals are carried by wind particles in our simulation. Stellar wind particles themselves only carry metals, but no magnetic field (as described in section 2.4.3). If they leave the galaxy and are deposited into the ICM, they contribute to gas cells with a high metal amount, but a low magnetic field. 2) high metallicity and high magnetic field gas leaves the galaxy, through galactic winds or ram pressure striping (we discuss both ideas later in section 3.8.1 and 3.8.2). The amount of gas in galaxies, compared to the amount of gas in the ICM is very small. Even if removing all gas from the galaxies, this could explain overall high metallicity values, but not overall high magnetic field values (we do a more detailed calculation in section 3.8 to show this). Wind particles that are deposited inside the galaxy, can explain galactic winds. Wind particles, that are deposited in galaxies, rather than in the ICM, would also explain the fact, that the radiative run does not show a higher level of enstrophy. Otherwise the stellar wind particles, leaving galaxies, would add turbulence to the ICM. This explains, why a magnetic field-metallicity correlation in the $z = 4$ panel is not clearly visible, when excluding the star forming regions. This consolidates the idea that the metal and magnetic field enriched gas only serves in such a way that it adds higher seed fields to the dynamo, instead of the idea that galaxies magnetise the ICM on their own.

Looking at the $z = 2.0$ plot, the emerging picture looks a bit different. In this case, a correlation between magnetic field and metallicity is also visible in the ICM, when excluding the star forming regions. This confirms the picture that pre-processing plays an important role to grow the magnetic field at later times. Substructures that have grown a magnetic field and high metallicity content themselves constantly merge into the cluster and cause this correlation (as discussed in section 3.3.5). The $z = 0$ panel shows that the distribution in the magnetic field-metallicity phase space is more narrow, compared to the previous ones. Especially, the low magnetic field and low metallicity regions have disappeared. We have seen this behaviour already in figure 19, where we saw that, at lower redshift, the magnetic field and metal radial profiles get enriched in the outskirts (where the magnetic field and metal values are lower) at the expense of the very central regions. As was discussed in section 3.5.1, this is either due to the merging of pre-enriched substructures and a saturated dynamo, or due to the ongoing SN activity of lower mass stars that pollute also the outer regions with metals.

3.6.4 Discussion

Marinacci et al. (2015), who perform a simulation similar to ours, where they compare the magnetic field evolution in a radiative and in a non-radiative run in a cosmological box (as discussed in section 3.3.6), also look at density-magnetic field histograms. In agreement with our findings, they see that, at high redshifts, the distribution follows the $B \propto \rho^{2/3}$ scaling, which is an indicator for adiabatic compression. In the adiabatic run, they also find that the distribution deviates steeper from the 2/3 scaling with time. They explain

this with turbulence and shear flows that act on top of the compression of gas and become more dominant with time. For their radiative simulation, they also have findings that are comparable to ours. They find that the dynamical range in the magnetic field axis and on the density axis covers a broader range that increases with time. Interestingly, they also develop a second branch with an increased magnetic field, that we also identified in the upper middle panel of figure 20a. Marinacci et al. (2015) attribute this branch to the interplay of cooling, shear flows and turbulence caused by galactic outflows. They explain this with the fact that the density, at which the separation of the branches occurs, is also reached in the adiabatic run. They conclude that higher densities (reached by e.g. cooling) is not what causes the bimordial distribution and that the reason has to be an increased level of turbulence, caused by galactic physics. This is in slight contrast to our findings. We do not see an increased level of turbulence in the radiative simulation. Though we also attribute the second branch to be caused by galactic gas, we assume that it just works such that it adds a higher initial magnetic field to start with to a dynamo that is acting in the ICM (as discussed in section 3.3.4). Their distributions, in the radiative and in the non-radiative setup, at the lower magnetic field end follows the 2/3 scaling with density, like we also see it. Thus, we resemble the contribution from adiabatic compression, that still affects the low magnetic field regions. Marinacci et al. (2015) look at magnetic field-density histograms for 4 different redshifts $z = 2.0, 1.04, 0.50, 0.00$, which is in the later range, compared to the redshifts that we analyse: $z = 6.2, 4.0, 2.0, 0.0$. The fact that we, nevertheless, observe similar features can be explained, as follows. Marinacci et al. (2015) analyse a cosmological box, while we analyse a galaxy cluster. We analyse an extremely overdense region, in comparison to a cosmological box, that also comes with low density regions, e.g. in cosmic voids. Compared to our simulation, the simulation of Marinacci et al. (2015) is thus biased towards lower densities, where a dynamo is potentially worse resolved. Furthermore, their resolution, even in the high density regions, is worse, compared to ours, which makes a dynamo less efficient (as was discussed in section 3.3.6). Additionally, many galaxies form at later redshifts, while we look at a very massive cluster, where the progenitor explicitly forms very early.

Roh et al. (2019), who simulate an isolated cluster without radiative physics also analyse a density-magnetic field histogram at $t = 4.6$Gyrs, which corresponds to a redshift of $z = 1.37$. They recover a scaling of $B \propto \rho^{1/3}$ and interpret this as result of the dynamo. This is a lower exponent than the exponent for adiabatic compression, 2/3. In our non-radiative run, we see a steeper exponent, compared to 2/3, which even grows with time. As already discussed in section 3.3.6, it could be that they underestimate the level of turbulence, caused by mergers.

Also Steinwandel et al. (2022), who perform a cosmological, non-radiative simulation, analyse magnetic field-density phase space diagrams. They look at redshifts of $z = 0.3, 0.0$, which they identify as the time, where the dynamo is in the linear phase and in the non-linear growth phase. A comment at this point is that their cluster experiences a bigger merger at $z = 0.3$ which gives potentially rise to the dynamo that they resolve, while our cluster undergoes larger mergers already at $z = 4.5$ and frequently from then on. Matching with our findings, they see the relation that results from flux freezing $B \propto \rho^{2/3}$ at the low magnetic field values. At their $z = 0$, they find that the high magnetic field values follow the $B \propto \rho^{1/2}$ scaling due to diffusive reconnection, as described by S. Xu & Lazarian (2020), indicating a saturated dynamo in a self-gravitating system. This is interesting, as we see hints for this scaling in our radiative run, already at $z = 2.0$, but not at all in the non-radiative run. A conclusion is that, at $z = 2.0$, the dynamo in the non-radiative run is not yet saturated. Steinwandel et al. (2022) do not see this scaling at

$z = 0.3$. In our $z = 0$ panels, both distributions roughly follow the 1/2 scaling, though the distribution in the non-radiative run still has a contribution from non-saturated regions. As S. Xu & Lazarian (2020) derive the 1/2 relation for a star forming cloud, that can cool very efficiently, Steinwandel et al. (2022) highlight that this is not the case for a galaxy cluster, which can be approximated as being virialized. Nevertheless, they explain the 1/2 scaling that they observe with the fact that merger also drive a galaxy cluster out of equilibrium and conclude that the 1/2 relation can be upscaled to galaxy clusters.

For the enstrophy and metallicity phase space diagrams, it is more complicated to compare our findings to the results of other people, as this is rarely investigated in galaxy cluster simulations. Pakmor et al. (2020) make metallicity-magnetic field phase space diagrams for their simulated galaxy. They want to trace the magnetisation of galactic outflows. They analyse the histograms for 3 different redshifts: $z = 3.5, 2.0, 0.0$. They find that the high magnetic field gas is also highly metal enriched at $z = 3.5$ and conclude that the magnetic field must have been amplified within the galaxy. Essentially, their $z = 3.5$ plot looks extremely comparable to our $z = 4.0$ plot in figure 20c, only that our gas extends further to lower metallicities. This is interesting, as they only look at the gas directly around galaxies. A conclusion is that galactic outflows also play a big role in the ICM, indicating that the high metallicity, high magnetic field gas is indeed produced in the galaxies. At $z = 2.0$, their distribution also looks comparable to our $z = 2.0$ distribution, only that Pakmor et al. (2020) resemble an almost perfect correlation between magnetic field strength and metallicity, while our distribution is additionally extended towards the low magnetic field, high metallicity corner. There are two possible explanations, that we already introduced in section 3.6.3. The first is given by the effects of the wind particles. They do not carry any magnetic field, but they carry metals. This could explain the low magnetic field, but very high metallicity values. The second explanation is given by the galactic gas being diluted by the ICM (that covers a larger volume, compared to the galactic halo that Pakmor et al. 2020 analyse) such that the magnetic field values drop steeply. Their distribution in the $z = 0$ panel again looks very comparable to ours. We conclude that the metal and magnetic field distribution int the ICM is thus very closely linked to the distribution in galaxies and surrounding galaxies.

A general remark regarding the enstrophy and metallicity histograms is that enstrophy is not a really accurate measurement for turbulence (as was already discussed in section 3.4.1) and that the metal enrichment module, especially at high redshift, also comes with uncertainties (as was already discussed in section 3.5.1)

3.7 Magnetic and Kinetic Energy Evolution With Time

An indicator for a dynamo manifests through turbulent, kinetic energy that is converted into magnetic energy. For a turbulent, magnetised medium, where the turbulence is purely in solenoidal form, a saturated dynamo would imply an equipartition between turbulent and magnetic energy. In figure 21, we show radial profiles of the magnetic and kinetic energy densities for the radiative and for the non-radiative run for three different redshifts $z = 4.5, 4.0, 3.5$.

We start the analysis by looking at the kinetic energy density (red). It stays roughly constant within the three different redshifts in the radiative and in the non-radiative run. This is matching with our analysis of the enstrophy in section 3.4, where we found that the level of enstrophy (as a proxy for turbulence) is high in general in the ICM and stays approximately constant with time. When comparing the radiative and the non-radiative run, we also do not see big differences. This is also matching with the similar enstrophy

values between the two runs that we found in section 3.4. In the radiative run, the kinetic energy density is slightly higher in the center. This can be caused by higher densities in the center or by turbulence in the central regions. The radiative run shows a slightly steeper profile as a function of radius, compared to the non-radiative run. Reason could be the higher gas temperatures in the non-radiative run. Higher temperatures yield higher sound speeds such that the conversion of kinetic energy into internal energy via shock heating is less efficient (the internal energy profiles, shown in figure A.4, resemble the same profile like the kinetic energy density in the non-radiative simulation).

The magnetic energy density profiles (blue) in the radiative run change with redshift. The magnetic energy density rises with time. First, it rises in the center and then it slowly catches up towards the outer radii. We have already seen this behaviour in the magnetic field radial profile in figure 19. In the center, the magnetic energy density and the kinetic energy density are almost in equipartition. This can be a sign for a saturated dynamo. More likely is that compression of gas also contributes to the high magnetic energy densities ($\epsilon_B/\epsilon_{\rm kin} > 1$ for $z = 0$ in the center, see figure A.5). In the non-radiative run, the magnetic energy density stays low within all shown redshifts. This resembles the picture that a dynamo can saturate faster in the radiative run. The saturation is fasted reached in the center.

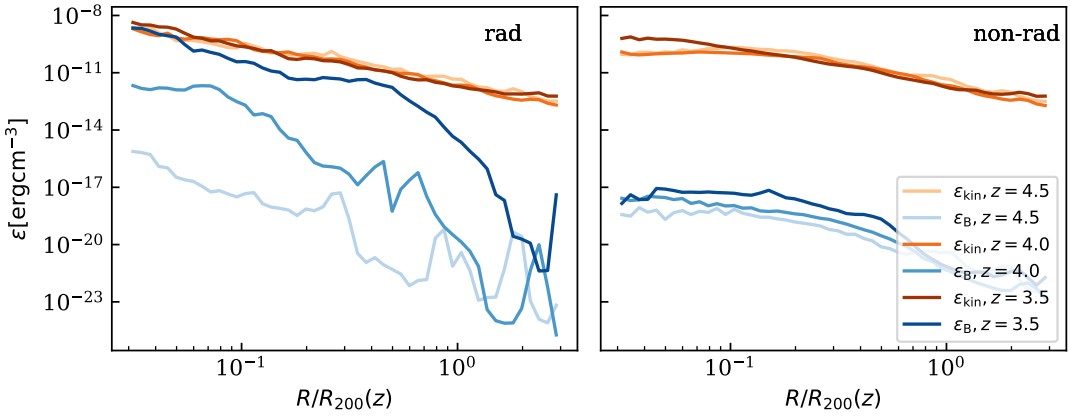

Figure 21: Radial profiles for the magnetic (blue) and kinetic (red) energy densities within $3 \cdot R_{200}(z)$. We show the radiative run, on the left, and the non-radiative run on the right. Different color shades are indicated with the color scheme. We calculate the kinetic energy density by subtracting the center of mass velocity from all cells: $\epsilon_{\rm kin} = 0.5 \cdot (\mathbf{v} - \mathbf{v_{CM}})^2 \cdot \rho$.

We study the late time, saturated regime. How much of the kinetic energy can be turned into magnetic energy? We follow Wittor et al. (2017) and calculate the efficiency factor $C_{\rm E}(z) = \epsilon_B(z)/\epsilon_{\rm kin}(z)$ (equation 53). In figure 22, we show the evolution with redshift. The magnetic energy is saturated at $z \approx 0.1$ in the radiative and in the non-radiative run. The efficiency coefficient in both runs stays constant until low redshift at $C_{\rm E} \approx 33\%$. Assuming that the magnetic field is amplified via turbulence with the small-scale dynamo only, this means that 33% of the kinetic energy can be converted into magnetic energy. The radiative (left) and the non-radiative (right) run, both look very similar. In the radiative run, the transition between increasing efficiency factor and constant efficiency factor happens abrupt. In the non-radiative run, the transition is smoother. The saturation at $z \approx 0.1$ is not matching with our findings from section 3.3, where we saw that the magnetic field strength stays approximately constant from $z = 3.5$ on in the radiative and

from $z = 1$ on in the non-radiative run. An explanation could be that the kinetic energy decays between $z = 3.5$ and $z = 0.1$ and $z = 1$ and $z = 0.1$, respectively, as the magnetic field strength stays constant at these earlier redshift. However, the fact that the ratio between magnetic and kinetic energy density stays constant towards the lower redshifts is characteristic for a saturated dynamo.

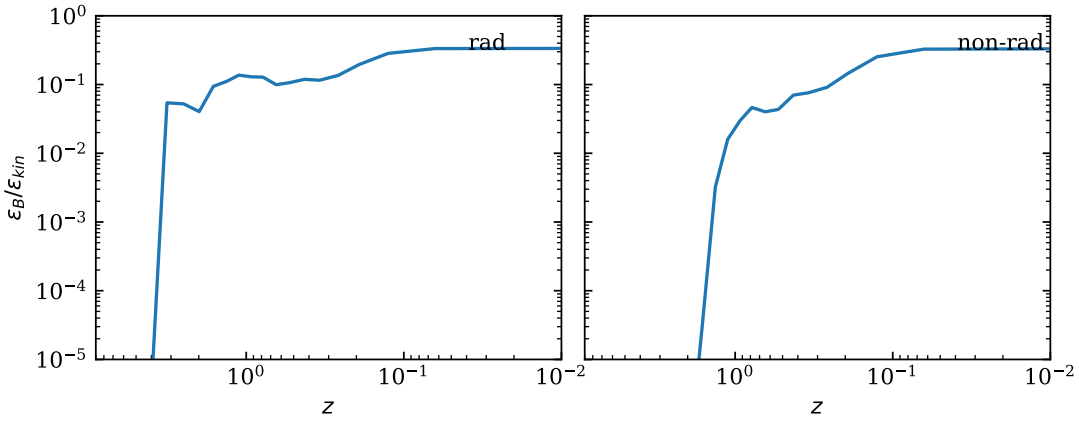

Figure 22: Redshift evolution of the ratio of magnetic energy density, ϵ_B, and kinetic energy density, ϵ_{kin}, for the radiative run (on the left) and the non-radiative run (right).

3.7.1 Discussion

We compare our findings to the work of Botteon et al. (2022), who perform observations of the galaxy cluster Abell 2255. The cluster has just experienced a merger and is therefor assumed to be turbulent. Derived from radio observations, they find an efficiency factor of turbulent energy to be converted into magnetic energy of $C_{\text{E}} = 0.05\text{-}0.1$. We find, in the saturated regime, $C_{\text{E}} \approx 0.33$. A possible explanation for this discrepancy is that we underestimate the kinetic energy the way we calculate it (as discussed below). Also, Abell 2255 just experienced the merger, so it could be the case that the magnetic energy will grow in the future.

Now we compare our results to the findings emerging from other numerical simulations. Wittor et al. (2017) also use an efficiency coefficient C_{E} (equation 53). In their simulations though, they do not include magnetic fields. They measure the turbulent energy dissipation to calculate a resulting magnetic energy. They use a constant $C_{\text{E}} \approx [4\%, 5\%]$, following Beresnyak (2012). Beresnyak (2012) do numerical simulations, where they solve MHD equations with explicit dissipation with stochastic non-helical driving. They find that $C_{\text{E}} \approx [4\%, 5\%]$ is a universal constant. They address the issue of this number being very small. They explain this by assuming that a possible decorrelation in the velocity field at the equipartition scale could wander upscale. As another explanation they mention that, in the dynamo theory, usually a low amount of resistive diffusion is assumed, such that it results in extremely tangled magnetic fields. According to Beresnyak (2012), in simulations though, magnetic fields are not observed to be so tangled at the smallest scales. They highlight that the peak in magnetic energy amplification lies above these scales. They state that turbulent diffusion, rather than resistive diffusion needs to be taken into account.

Miniati & Beresnyak (2015a) apply the work of Beresnyak (2012) to the ICM. They

justify this with describing the ICM to contain statistically isotropically and homogeneous turbulence. An efficiency coefficient of $C_{\mathrm{E}} \approx$ 4-5% is smaller by more than a factor of 6, compared to our $C_{\mathrm{E}} \approx 33\%$. An explanation is that Beresnyak (2012) include explicit diffusion, such that the effects of numerical and explicit diffusion could act on top of each other and make a dynamo less efficient. We, in contrast, solve the ideal MHD equations (equations 25- 28) without explicit diffusion. An interesting question would be to study, which model is more applicable to the ICM. Beresnyak (2012), Miniati & Beresnyak (2015a) and Wittor et al. (2017) state that C_{E} is an universal factor. We clearly see a time evolution in this efficiency factor. This shows how the efficiency factor is dependent on the shape and form of turbulence.

Vazza et al. (2014) perform simulations of the small-scale dynamo in galaxy clusters. They find an efficiency of the kinetic turbulent energy to be converted into magnetic energy between $C_{\mathrm{E}} =$ 0.1-0.3. Similar to our findings, Vazza et al. (2014) see a time evolution of the efficiency coefficient. They find that the efficiency factor rises first, when the magnetic energy gets amplified exponentially. At lower redshift though, this factor decreases again due to an increase of the kinetic energy. We only look explicitly at the kinetic energy change at the redshifts $z = 4.5, 4.0, 3.5$. Within these redshifts though, the kinetic energy stays approximately constant. Nevertheless, the results of Vazza et al. (2014) are still closest to our findings for an efficiency of the dynamo to turn kinetic turbulent energy into magnetic energy. We still sit at the high end of their estimate though.

In general, the efficiency factor is heavily dependent on the properties of the plasma and also on the properties of the turbulence. It is especially dependent on viscosity and diffusion, which are hard to observe and, in simulations, heavily affected by numerical errors. This could explain the degree of uncertainty in this efficiency factor. It could be that we do not properly estimate the kinetic turbulent energy, as was already discussed in section 3.4.1. Our estimate of the turbulent kinetic energy could be biased towards bulk or compressible motions that we did not consider in our analysis. Another reason for these differences in the efficiency factor is that the level of turbulence is dependent on the occurrence and frequency of merger. Especially in observations, it is impossible to analyse the time evolution of this efficiency factor.

3.8 Galaxies

In galaxies, the magnetic field can grow due to a high amount of turbulence and higher gas densities (see section 3.6). But how can the high magnetic field gas, that is gravitationally bound to galaxies, emerge from the galaxies to pollute the ICM? In this subsection, we first show that some of the galaxies indeed lose their gas. Then, we investigate the mechanism that is responsible for the gas loss. As already introduced in section 2.4, we discuss the effects of ram pressure striping and galactic winds. We only focus the analysis in this section on the radiative run.

For the analysis so far, we dubbed the star forming regions as "galaxies". Now, we refer to galaxies, as the subhalos that are identified with the SUBFIND algorithm (introduced in section 2.4.3).

In figure 23, we show the gas mass in galaxies in the left panel. In the middle and right panel, we show only the galaxies without gravitationally bound gas (those from the outer most left bin in the left panel). We show the distance to the center of mass of the cluster in the middle panel and the virial temperatures (accordingly to equation 7) in the right panel. We show the evolution of the subhalos for 5 different redshifts $z = 9.0, 6.2, 4.5, 4.0, 3.5$. At

a redshift of $z = 9.0$, we are in the phase after the collapse of the protocluster, in which the magnetic field grows primarily in the central galaxy. The redshift $z = 6.2$ coincides with the time shortly after or during reionization. The last redshifts, $z = 4.5$-3.5 correspond to the time, in which the magnetic field grows exponentially in the radiative run.

We start the analysis by looking at the left panel. We see that a large fraction of galaxies does not have any self bound gas. The number of galaxies without gravitationally bound gas rises by almost a factor of 10^2. At $z = 9.0$, four subhalos without gas are identified. At $z = 3.5$, this number has increased to 300. The number of galaxies without any self-bound gas makes the largest fraction of all subhalos.

We take a closer look at those subhalos without self-bound gas. In the middle panel of figure 23, we show their distances to the cluster center of mass. A large fraction of galaxies already enters the cluster without any gas. These galaxies are sitting at distances larger than the virial radius, $> R_{200}(z)$. With increasing distance from the center, also the number of galaxies without gas increases. This can be due to the fact that there are simply more galaxies in total at higher radii (as the circumference grows together with the radius). This is interesting, as the effects of ram pressure stripping (see section 2.4.2) become more dominant with decreasing distance to the center. Three possibilities emerge from this: First, the galaxies are already pre-processed in the merging substructures (see section 3.3.6), where they loose their gas, before they enter the cluster. Secondary, galactic winds, caused by massive SN explosions, set in at high radii, such that they remove the gas. The third possibility is gas loss due to the high energy radiation that comes with reionization. We analyse the third possibility in the next paragraph. Comparing the redshift evolution, we see the same trend imprinted onto all redshifts: most galaxies without self-bound gas, sit at the highest radii. The fraction decreases towards lower radii and the total number of galaxies without gas increases with time.

We analyse the right panel, showing the virial temperatures of the galaxies without any self-bound gas. Galaxies with a virial temperature $T_{200} < 10^4$K can lose their gas during reionization, that takes place at $z \approx 7$ (see section 2.4). At this redshift, the magnetic field has not yet experienced its exponential growth phase. In our simulation, FABLE implements the effects of reionization with a time varying, uniform UV background (introduced in section 2.3.4). For $z = 9.0, 6.2$, all galaxies without gravitationally bound gas have virial temperatures below the critical temperature for reionization to unbind the initial gas $T_{200} < 10^4$K. Only from $z = 4.5$ on, also galaxies with higher virial temperatures appear as gas less galaxies in the cluster. For $z < 9.0$ though, most of the galaxies have virial temperatures between 10^3-10^4K. We conclude that these galaxies could have lost their gas due to reionization. For the halos at $T_{200} > 10^4$K in the redshift range $3.5 < z < 4.5$ though, reionization is not sufficient to remove the gas, as it is too gravitationally bound. The range $3.5 < z < 4.5$ coincides with the time, where the magnetic field grows exponentially in the radiative run. In the following, we take a closer look at these galaxies and try to address the effects of ram pressure stripping and galactic winds to this.

Figure 23 shows that galaxies lose their gas. The gas in galaxies has higher magnetic field strengths, compared to those in the ICM. But, Even if all the galaxies in the cluster would lose their gas though, this would not explain the higher growth rates in the radiative run, compared to the non-radiative run. We make a simple volume argumentation, assuming that the galactic gas just expands spherically from galaxies. Assuming that the galactic gas just expands into the ICM and assuming that the magnetic energy stays constant

meanwhile, this yields

$$B_{\mathrm{Cl}}^2 \cdot V_{\mathrm{Cl}} = N_{\mathrm{gal}} \cdot B_{\mathrm{gal}}^2 \cdot V_{\mathrm{gal}}, \tag{62}$$

such that

$$\frac{B_{\mathrm{Cl}}}{B_{\mathrm{gal}}} = \sqrt{N_{\mathrm{gal}}} \left(\frac{R_{\mathrm{gal}}}{R_{\mathrm{Cl}}} \right)^{3/2} \tag{63}$$

where B_{Cl} is the magnetic field in the cluster, V_{Cl} the volume occupied by the cluster and for the galaxies, respectively and N_{gal} is the number of galaxies. At $z = 0$, there are $N_{\mathrm{gal}} = 8792$ subhalos that sit within the virial radius of the cluster $R_{\mathrm{Cl}} = 2968.5$kpc. The mean size of a galaxy at this redshift is $R_{\mathrm{gal}} = 10.2$kpc. The magnetic field strength in the cluster at this redshift is approximately $B_{\mathrm{Cl}} \approx 5\mu$G (see figure 15). Thus, in order to explain this magnetic field strength by removing the gas from galaxies only, the galaxies would need, on average, to have a magnetic field strength of $B_{\mathrm{gal}} = 264.75\mu$G, which we do not observe. Figure 15 shows instead that the galaxies reach magnetic field strengths at the order of 20μG. This is lower by more than a factor of 10. We conclude that the gas in the galaxies only gives higher initial seed fields to a dynamo in the ICM, instead of magnetising the ICM on their own.

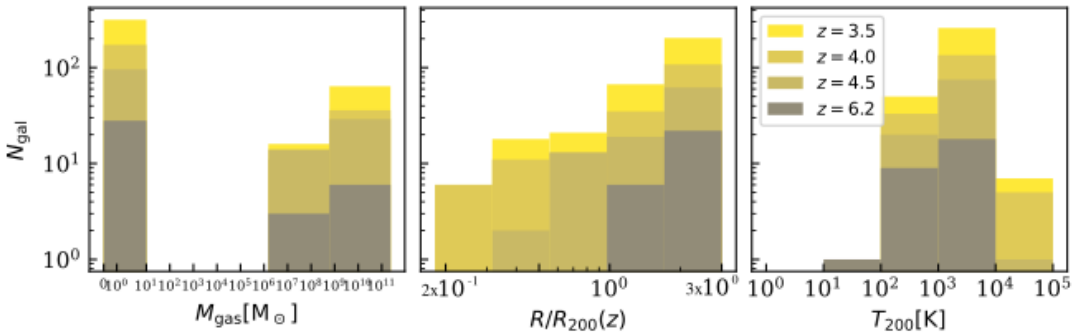

Figure 23: Histogram of the number of galaxies that have a certain gas mass (left panel). The galaxies with little, to no gas mass (outer left bin) are additionally shown in the middle and right panel. From these halos without any self-bound gas, we show the distance from the center (middle panel) in units of the virial radius $R_{200}(z)$ and the virial temperature (right panel), from equation (7). We show the evolution for 5 different redshifts, indicated with the color scheme.

3.8.1 Ram Pressure Stripping

Ram pressure stripping is a process that can remove gas from galaxies (introduced in section 2.4.2). Galaxy clusters and their environments are high density regions, which makes ram pressure stripping likely to occur. This does not only account for the cluster, but also for the merging substructures. Ram pressure stripping is discussed to solve the Butcher-Oemler effect (introduced in section 2.4.2), which describes the decreasing amount of blue galaxies in galaxy clusters with decreasing redshift. Ram pressure stripping can also be important in the context of pre-enrichment (discussed in section 3.3.6). Here, it can remove gas from galaxies in the merging substructures, such that it is mixed with the ICM after the substructures merge into the cluster.

In figure 24, we show projections of the cluster from the radiative run at 4 different redshifts $z = 6.2, 4.5, 4.0, 3.5$. The projections have sidelengths of $6 \cdot R_{200}(z)$ and a similar projection depth. The virial radius is indicated with the white circle. We show projections of the magnetic field strength on the upper panel and projections of the metallicity in the lower panel. Each red point indicates a galaxy, that fulfills the Gunn and Gott criterion (equation 57) for ram pressure stripping to occur (introduced in section 2.4.2).

Figure 24 shows that ram pressure stripping is very likely to occur. This trend remains throughout all redshifts. The number of galaxies that could be affected by ram pressure striping increases with time. In the cluster, the identified galaxies sit at all radii. The radial independence for ram pressure stripping to occur can be caused by high densities in the ICM at high radii or low galaxy masses, such that the gravitational binding force onto the galaxy is low. Most galaxies though that fulfill the Gunn and Gott criterion lie beyond the virial radius, inside of merging substructures. This is especially true for $z = 6.2$. What is interesting is that most galaxies that reside in merging substructures, sit in high metallicity and high magnetic field gas halos. We conclude that ram pressure stripping is a possible mechanism that removes gas from galaxies to enrich the halos of merging substructures. This can be important in the cluster, but also in the merging subhalos that add their pre-enriched gas to the ICM, when they merge with the main cluster.

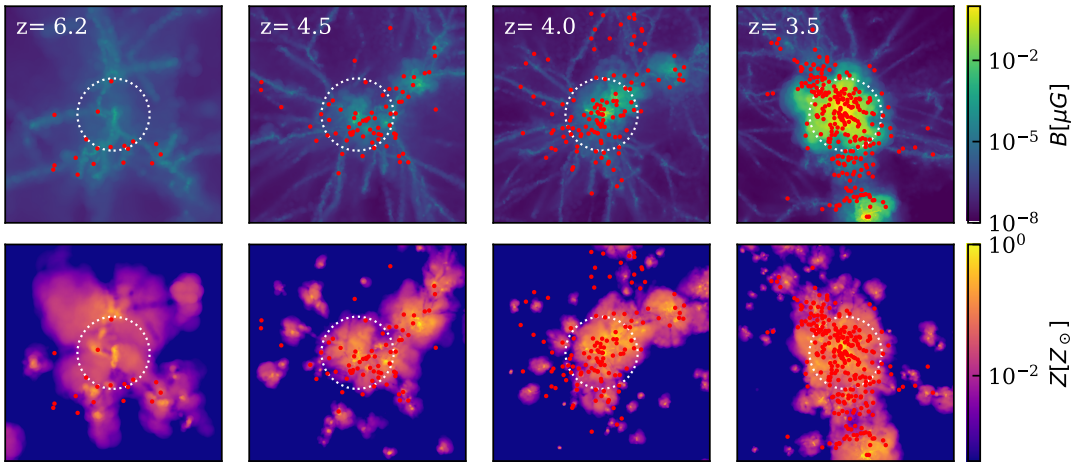

Figure 24: We show projections of the cluster in the radiative run with sidelengths of $6 \cdot R_{200}(z)$ and a similar projection depth. The redshift-dependent virial radius is indicated with the white circle. We show projections of the volume weighted root mean square magnetic field strength (upper panel) and the mass weighted metallicity (lower panel) for the radiative run. Red marker indicate the galaxies, identified with SUBFIND that are subject to ram pressure stripping, according to equation (57).

3.8.2 Galactic Winds

We take a closer look at four of the galaxies that we identify as possible ram pressure candidates. We take one galaxy, that sit inside the virial radius of the cluster, from each redshift plot in figure 24. In figure 25, we show magnetic field and metallicity projections of these galaxies. We indicate twice the half mass radii of the galaxies with the white circles. We indicate the direction of the center of mass velocity of the galaxy, relative to the surrounding ICM, with the red arrows. We show galaxies at four different redshift $z = 6.2, 4.5, 4.0, 3.5$.

Figure 25 shows that indeed high magnetic field and metal enriched gas is removed from the galaxies for $z = 4.5, 4.0, 3.5$. At $z = 6.2$, we see that the galaxy is surrounded by a metal enriched halo. This halo is not enriched with a high magnetic field. At this high redshift, the magnetic field grows predominantly in the center, where the most massive galaxy sits (see figure 15). Metals are created earlier, compared to magnetic fields (see figure 17), at the same time that the first stars are created. The enrichment of a metal enriched, but magnetic field poor halo can be due to the SN wind model in FABLE. The SN inject wind particles that carry metallicity, but no magnetic field. These wind particles can leave the galaxy and recouple in the ICM. For the galaxy at $z = 6.2$, we see artifacts of our SN wind module.

We see morphological hints for ram pressure stripping only in the galaxy at $z = 4.5$. The stripped gas is moving in anti parallel velocity direction and forming a tail like structure behind the galaxy. The galaxies at $z = 4.0$ and $z = 3.5$ do not show this feature though. At $z = 4.0$ and $z = 3.5$, the morphology of the removed gas is more characteristic for galactic outflows. The outflows lie in front of the galaxies, whereas ram pressure stripping would cause the gas to move behind the galaxies. Also, the removed gas extends over a large region, whereas ram pressure stripped gas is thought to form a more narrow tail. Especially for the galaxy at $z = 4.0$, we see hints for a bipolar outflows that would be characteristic for galactic winds. The fact that the metals seem to be spread more smoothly within the projected area, compared to the agetic field (also at $z = 6.2$), is an indicator for SN driven winds. As discussed in section 2.4.3, the wind particles in FABLE carry metals, but no magnetic field. If deposited in the ICM, the magnetic field in the galaxies remains untouched. If deposited inside the galaxy, the wind particles deposit their momentum, which can lead the gas cell, including its magnetic field and metallicity, to leave the galaxy. This could be an explanation for the slightly more smooth metal distribution. We conclude that galactic winds caused by galaxies are a possible mechanism to remove gas from galaxies.

We show that SN wind particles are likely to occur. We show the evolution of the star formation rate (SFR) in galaxies with redshift in figure 26. The SFR is proportional to the SN rate, as star particles and wind particles (for high mass stars; the local wind) are created in the same timestep (see section 2.4.3). We only include galaxies that sit within the virial radius of the cluster. We add up the SFRs of all gas cells that are inside galaxies. Figure 26 shows that the high SFRs are high in the redshift range $4.5 > z > 3.5$. At these high redshifts, the cluster consists only of a few galaxies. At $z = 4.5$, it contains 28 galaxies, while at $z = 0$, it contains 8792 galaxies. Normalizing the SFR by the number of galaxies, yields even higher SFRs per single galaxies at the high redshifts. We conclude that the star formation efficiency and thus, the SN rate is way higher in these high redshift galaxies, compared to the lower redshift ones. An additional effect is that the high redshift galaxies are smaller, compared to the low redshift galaxies (an average radius of a galaxy at $z = 4.5$ is $R_{\text{gal}} \approx 5$kpc, while at $z = 0.0$ it is $R_{\text{gal}} \approx 10$kpc in our simulation). In smaller galaxies, that also have a lower mass, wind particles can more easily remove the gas from galaxies, as it is less gravitationally bound. We conclude that SN feedback in high redshift galaxies is a possible cause for removing gas from galaxies.

3.8.3 Discussion

Observations show that galaxies undergo a morphology change in galaxy clusters. They transform from blue and gas rich galaxies to quenched, red ones. This is described by the Butcher-Oemler effect, as described in section 2.4.2. We also see this evolution in our

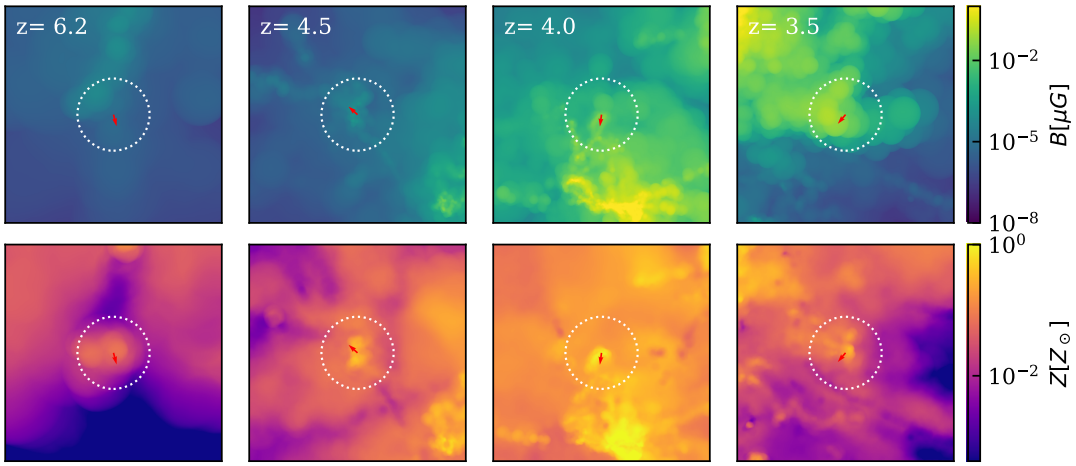

Figure 25: We show projections of four of the galaxies identified in figure 24 that lie within the cluster virial radius. We show projections with sidelengths of $6 \cdot R_{200}(z)$ in units of the virial radii of the galaxies and a similar projection depth. The redshift-dependent virial radius is indicated with the white circle. We show projections of the volume weighted root mean square magnetic field strength (upper panel) and the mass weighted metallicity (lower panel) for the radiative run. Red arrows indicate the center of mass velocity of the galaxies, relative to the mean velocity of the ICM within $5 \cdot R_{200}(z) < R < 6 \cdot R_{200}(z)$. We show galaxies at four different redshifts: $z = 6.2, 4.5, 4.0, 3.5$.

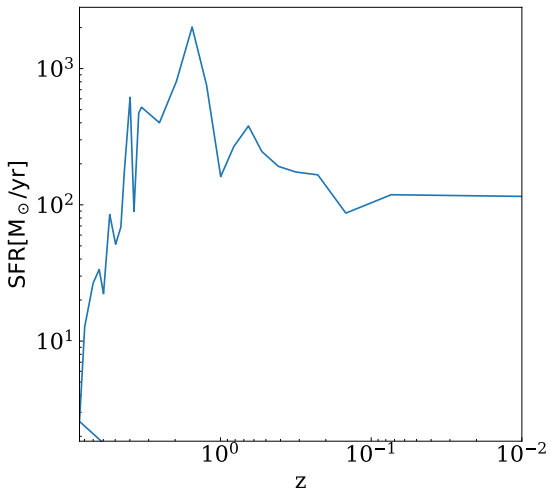

Figure 26: We show the evolution of the summed up star formation rate of all star forming cells that are inside subhalos, within the virial radius of the cluster $R_{200}(z)$ with redshift.

simulation, starting already at high redshift $z = 9$ and becoming more pronounced with time. Also other simulations support this picture. Dolag et al. (2009) find that, at $z = 0$, only about one percent of all galaxies inside the virial radius have self-bound gas.

We start by discussing the effects of reionization. In our analysis, we assumed that reionization occurs at $z \approx 7$ and affects all galaxies with $T_{200} <= 10^4$K. Observationally, the redshifts, at which reionization occurs can be inferred from quasar observations at high redshift (Barkana & Loeb, 2001). Clouds of neutral hydrogen that lie on the line of sight to the quasar modify its spectrum which gives hints about the corresponding redshifts. In fact, reionization spans over a larger redshift range (Barkana & Loeb, 2001). Such a time range would result in slightly different virial temperatures of galaxies that are subject to

reionization. Also, the ability of reionization to ionize a galaxy is highly dependent on the stellar content within the galaxy. This makes reionization not equally efficient in all subhalos. In our simulation, FABLE implements a uniform, time varying UV background, which does not take into account the spatial variability. Thus, it is possible that we overestimate the effects of reionization and the gas mass loss of small galaxies due to this. This would yield even stronger hints that the galaxies have to lose their gas via some other channel (ram pressure stripping and galactic winds).

Different groups performed simulations to study the ability of reionization to quench small galaxies. Shapiro et al. (2004) perform numerical simulations, including a model for radiative transfer in order to study the effects of reionization. They find that, at $z = 7 - 9$, small mass galaxies with $M_{200} < 10^7 M_\odot$ can lose all their gas. As ionizing sources, they take SN and high redshift quasars into account. Barkana & Loeb (1999) find that between $z = 10 - 5$, the halos with $T_{200} < 10^4$K can lose all their gas. This gas can enrich the surrounding material. They state that, according to theory of structure formation, this concerns 50-90 % of all galaxies.

Madau et al. (2001) suggest that photoreionization combined with SN feedback can create a galactic halo of already pre-enriched gas. They assume that the same stars are the source for the ionizing photons and for SN feedback. They find that reionization heats the gas around halos. Madau et al. (2001) state that tangled SN can create superbubbles, filled with hot gas, that sweep up gas from the galaxy and that expands into the pre-heated halo. The thermal pressure of the halo halters the outflowing galactic gas and keeps it trapped in the halo. This could be interesting in the context of pre-enrichment. The effects of reionization can cause galactic gas to be moved into galactic halos, where it is efficiently stripped by the cluster (as the gravitational binding force onto the galaxy is lower at higher distances from the galaxies center) and added to the ICM. This gas can already be enriched with a high magnetic field. We conclude that, at high redshifts, also reionization can lead low mass galaxies to lose gas in the ICM and in merging substructures. The question is though, how effectively small mass galaxies have grown a strong magnetic field at these high redshifts.

Now we discuss the effects of ram pressure stripping. We begin with a general remark on our method of estimating the effects of ram pressure stripping (according to equation 57). We made a lot of simplifying assumptions and probably overestimate the number of galaxies that are subject to ram pressure striping. Galaxies do not always move face on. Galaxies are also not cylinders, nor do they have a constant density. Also magnetic draping needs to be considered. As a galaxy moves through the ICM, magnetic field lines can drape around it. This can potentially shield the galaxy, as the ICM is transported along the field lines (Sparre et al., 2019). Most studies find that ram pressure stripping alone cannot remove all the gas contained in galaxies. Especially in the bulge, the gas is too gravitationally bound (Abadi et al., 1999; Quilis et al., 2000).

The effects of ram pressure stripping can be observed e.g. via observations of neutral hydrogen. Serra et al. (2023) make neutral hydrogen observations in the Fornax cluster. They identify several ram pressure stripped galaxies that carry a tail of neutral hydrogen. They contribute this to ram pressure stripping, as the tails lie within the radial movement of the galaxies. They find that the densities in the Fornax ICM are too low for ram pressure stripping to occur. They suggest that tidal interactions lift the galactic gas into the halos, where it is less gravitationally bound and can be more easily stripped by the ICM. We did not investigate tidal interactions in our analysis. The Fornax cluster is less

massive than our simulated cluster by a factor of more than 50. This would yield lower gas densities in the ICM of the Fornax cluster that is less effective in strippng the gas from galaxies. Our ram pressure analysis shows that many galaxies can potentially be ram pressure stripped, even without accounting for tidal interaction.

Vogelsberger et al. (2018) use a similar galaxy formation module, compared to ours. The difference to our module is that their wind is purely kinetic and their AGN radio bubble model has a slight modification. They take clusters from a cosmological simulation and analyse the origin of metals in the ICM. They find that ram pressure stripping contributes to 10-15 percent of the total metal content in the ICM. They find that ram pressure stripping is more dominant near cluster center, whereas galactic winds are mostly what outdrives metals at the outskirts. At $z = 0$, most metals (80 %) are accreted via merging substructures. This is matching with our findings on the effects of pre-enrichment. We do not see a radial dependence for the ram pressure stripping candidate galaxies. Dolag et al. (2009), who do cluster zoom-in simulations, taken from a cosmological simulation find that, at $z = 0$, only one percent of all galaxies inside their simulated cluster has self-bound gas. They find a radial dependence and address ram pressure stripping to this. As we do not see a radial dependence of the ram pressure galaxy candidates, we can not definitely say that ram pressure stripping is responsible for removing the gas.

In the following, we discuss the possible effects of galactic winds. Fujita et al. (2008) perform X-ray observations of the cluster binary A399 and A401. They find a uniform metal distribution within the area, in which both clusters sit. They exclude ram pressure stripping as the reason, because the gas densities are too low. They suggest that the cluster has formed in an environment that is already pre-enriched with metals. According to Fujita et al. (2008), the pre-enrichment can be due to AGN outbursts or episodes of intense star formation at high redshift $z > 2$. Comparing this to our findings, an interesting question is to think about when a cluster actually forms. We attribute the homogeneous metal distribution to the accretion of already pre-enriched substructures. We state that the cluster, mainly consisting of the BCG at high redshift, accretes these pre-enriched substructures. To say that the cluster forms in a pre-enriched environment is maybe another way of describing the same effect. In general, we can resemble the peak of star formation to be at $z \approx 2$, which is also inferred from observations Hughes et al. (1998).

M. Hou et al. (2021) perform X-ray observations of galaxies in the Virgo cluster. They study 80 low to intermediate mass galaxies. They find that most of the galaxies, 72 out of 80, have lost their gas. Only two galaxies show morphological features for ram pressure stripping. They also perform observations of field galaxies and see the same trend. They conclude that galactic winds are the main cause for removing the gas, as field galaxies do not live in high density environments, where they are affected by ram pressure stripping. Comparing to our findings, we see only one out of four galaxies with morphological hints pointing towards ram pressure stripping. Also matching with our findings, we see galaxies that are not inside the cluster, without any self-bound gas.

Koudmani et al. (2021) use the same galaxy formation model like us, FABLE, to study the quenching of low mass galaxies at high redshift. They find that, at high redshift $z > 2$, AGN in quasar mode are responsible for removing gas from low mass galaxies. For low redshift galaxies $z < 2$, they find that SN feedback is the reason. This is somewhat in contradiction to what is usually assumed: SN feedback is dominant for $z > 2$ and AGN feedback for $z < 2$ (Mutch et al., 2013). Koudmani et al. (2021) state that they probably overestimate the amount of stellar feedback. This could lead to reduced AGN feedback at

low redshift, as the stellar feedback quenches the gas reservoir for the AGN. On the other side, they find larger AGN black hole masses, than is usually assumed, in some of their low mass galaxies. This leads to strong galactic winds at high redshift. As we use the same galaxy formation model, the overestimation of stellar feedback and black hole masses might also play a role in our simulations. We would need to investigate the time evolution of AGN and stellar feedback in our galaxies further in order to determine whether this is the case.

Höller et al. (2014) study clusters in their simulations. They find that the largest contribution from galactic gas inside the ICM comes from galactic winds. They state that the effect of ram pressure stripping only becomes important at low redshift and shows a strong radial trend.

A remark at this point is that we did not perform any detailed analysis on the ouflows from galaxies. We have not in detail studied the outflows from galaxies due to stellar or AGN feedback. We also did not perform a detailed morphology analysis of mutliple possibly ram pressure stripped galaxies. We also did not perform a detailed analysis of our implemented UV background that could give hints about the effects due to reionization. We only analysed certain indicators for ram pressure stripping, galactic winds and photonionization to occur. Namely applying the Gunn and Gott criterion to galaxies to identify possible ram pressure stripped candidates, look at the morphology of the removed gas of four of these galaxies, look at the SFR evolution with time and calculating virial temperatures of galaxies without any self-bound gas.

However, we see that a large fraction of galaxies loses their gas. This fraction increases with time. In our simulation, we see possible effects of reionization, ram pressure stripping and galactic winds. Probably, it is an interplay of these. Though we need to perform a more sophisticated analysis (as described above), the points mentioned in this discussion-section let the following picture emerge: galaxies lose their gas, in the cluster but also outside the cluster. Ram pressure stripping alone is probably not responsible for removing all the gas from galaxies. It is thought to have a radial dependence and to become more dominant with lower redshift (as discussed above). SN outflows are thought to play a more dominant role at higher redshift, whereas AGN outflows are thought to play a dominant role at lower redshift. We see hints for galactic outflows caused by SN feedback in the morphology of the displaced gas, as well as the high SFR at high redshifts. The discussion in this section shows that it is important to also simulate the environments of clusters (as in a cosmological box). Otherwise, the effects of accreted halos are not considered. Galactic physics are highly dependent on the underlying model for galaxy formation. These come with big uncertainties and can yield potentially very different results.

4 Summary and Outlook

We summarise our methodology and findings. We analysed zoom-in simulations of the fifth most massive cluster from a cosmological box. We analysed two different simulations of this cluster: 1) the radiative simulation, which includes the galaxy formation module and the MHD module, and 2) the non-radiative simulation, which includes the MHD module only. The former's galaxy formation module includes models for gas cooling, AGN seeding, growth and feedback, and stellar formation and feedback. We studied and compared the magnetic field evolution in both simulations from $z = 47\text{-}10^{-2}$, in order to isolate the effects of galaxy formation on the magnetic field evolution. We studied the magnetic field and metal enrichment of merging substructures. We analysed the amount of turbulence in both simulations. We studied the correlation between enstrophy-magnetic field strength, and the correlation between density-magnetic field strength in both simulations. In the simulation, including the galaxy formation module, we analysed the contribution of galaxies. Moreover, we looked at enstrophy-magnetic field and density-magnetic field correlations in the galaxies in detail. We studied the gas masses in galaxies. We identified galaxies that can be subject to gas loss during reionization, due to ram pressure stripping or due to galactic winds.
Our conclusions are as follows:

- The magnetic field strength reaches values of $\sim 5\mu$G in the center in both simulations (figure 15). The magnetic field has higher growth rates in the radiative run (figure 16). The final field strengths are already reached at $z = 3.5$. In the non-radiative run, this happens at $z = 1$. Inside galaxies, the magnetic field reaches higher values compared to the ICM. In the radiative run, the growth experiences one exponential growth phase, where the magnetic field grows almost independent on resolution (figure 16). It grows with a similar rate in the ICM and in the galaxies (figure 16). In the non-radiative run, the magnetic field experiences two growth phases (figure 15). Each phase has a different growth rate (figure 16).

- The galaxies potentially lose their high magnetic field gas, which pollutes the ICM (figure 23). We conclude that the galactic gas adds higher initial magnetic field values to a dynamo in the ICM. Galaxies are not able to magnetise the ICM on their own, as the mass ratio between all star forming gas and total gas in the ICM is low. In galaxies, the magnetic field can grow fast due to high densities and a high amount of turbulence. The magnetic field strength is positively correlated to density and enstrophy in the star forming regions (figures 20a and 20b).

- A large fraction of galaxies loses their gas. The fraction of galaxies without any self-bound gas increases with time (figure 23). In many of those galaxies, the conditions for ram-pressure stripping to occur are fulfilled (figure 24). We looked at the morphological features of the displaced gas of four of these galaxies. One galaxy shows morphological evidence for ram pressure stripping, namely the displacement of gas aligned with the velocity of the galaxy. Three galaxies show indications for galactic winds caused by SN. Namely a smoother distribution of the displaced metallicity in comparison to a narrower distribution of the displaced magnetic field gas. This is characteristic for our SN wind model (figure 25). Furthermore, photoionization due to reionization can remove gas from high redshift, low mass galaxies. The virial temperatures of these galaxies lie below the critical temperature for gas loss due to reionization (figure 24).

- At high redshift, between the collapse of the protocluster and the first bigger merger, $9.5 > z > 4.5$, the magnetic field growth is dominated by the central region (figure 15). This is dominated by the BCG at these high redshift.

- The other channel to grow the magnetic field in the ICM goes via mergers. Galaxy clusters grow by merging with substructures. These have developed their own, already metal and magnetic field enriched ICM. This is added to the ICM of the main cluster after the merger. This process is referred to as pre-enrichment (figure 17). The constant merging of substructures that are pre-enriched leads to a positive correlation between the magnetic field strength and the metallicity from $z \approx 2$ and onwards (figure 20c).

- We see indicators for a turbulent small-scale dynamo in the ICM and in the galaxies. The evidences are: the rise of magnetic field after events that drive turbulence (figure 15), the constant ratio between the magnetic and the kinetic energy density as redshift decreases (figure 22), the positive correlation between the magnetic field strength and the enstrophy in the star forming regions (figure 20b), and the magnetic field-density scaling $B \propto \rho^{1/2}$ in the radiative run, beginning from $z = 2$ on (figure 20a). The latter is an indicator for a saturated dynamo.

- We identify three events that lead to an amplification of the magnetic field. The first one is the collapse of the protocluster at $z = 9.5$. This enables higher densities and thus higher magnetic field strengths. It also adds turbulence to the ICM via a structure formation shock. The second and the third one are the 2 mergers at $z = 4.5$ and $z = 2$, which inject turbulence to the ICM. These mergers could be responsible for the two different growth phases in the non-radiative run (figure 15).

- The evolution in the magnetic field radial profiles across a large redshift range ($9.5 > z > 0$) is very similar to the evolution of the metallicity profiles in the same redshift range (figure 18). From $z = 2$ on, we see a positive correlation between metallicity and magnetic field strength in the ICM (figure 20c). The reason for the similarity in the higher redshift range, $4.5 > z > 3.5$, is that both, magnetic field and metallicity enrichment are dominated by the BCG. At lower redshifts, $z < 2$, we explain the correlation between magnetic field and metallicity with mergers that bring their metal and magnetic field enriched gas into the ICM. Turbulence mixes the central with the outer radii gas.

- At $z = 0$ both simulations - the radiative and the non-radiative simulation show similar features in the magnetic field. The spatial distribution, morphology, and the inferred field strengths look very similar (figure 13).

- The main drivers for turbulence in the ICM are the collapse of the protocluster, as well as mergers, that are constantly occurring. The level of turbulence remains high and nearly constant with redshift. Due to this, the amounts of turbulence in the radiative and non-radiative run are very similar. Only the central ICM in the radiative run shows a higher amount of turbulence at high redshift ($9.5 > z > 4.5$). This phenomenon is possibly caused by SN feedback (figure 18). We do not see a correlation between enstrophy and magnetic field strength in the ICM in both runs (figure 20b).

- At very high redshift, $z > 9.5$, the magnetic field is lowered due to adiabatic expansion, caused by the expansion of the universe (figure 15).

- The density profiles in both simulations look very similar, especially at lower redshifts. At $z = 0$, they can be described with a single beta profile. At higher redshift, the radiative run shows higher densities in the very center, caused by radiative cooling, that enables higher densities (figure 19).

Having summarized the results of our analysis, we will now discuss some of its shortcomings. We mainly use indirect indicators for what happens in the simulations. For example, we use enstrophy as measurement for turbulence and conclude that a dynamo can act in the ICM. It would be useful to make a powerspectrum of the turbulent energy, as well as of the magnetic energy. This could yield a clear proof that we develop turbulence (the turbulent powerspectrum should scale, accordingly to the Kolmogorov spectrum in equation 20) and that we can resolve a dynamo (the magnetic power should scale, accordingly to the Kazantsev spectrum in equation 48).

The efficiency of a dynamo is dependent on the smallest scales that we can resolve. So far, we only analysed the effects of the resolution on the growth rate of the magnetic field for two different resolutions: zoom8 and zoom12. At least in the radiative run, these did yield similar results with only small differences. It would be interesting to see, how a higher resolution affects the magnetic field growth in the radiative run. Can we grow the field faster in the galaxies? Also a higher resolution in the non-radiative simulation would be interesting to study. Which resolution without galaxy formation is needed in order to grow the magnetic field equally fast as in the radiative simulation, but at a lower resolution?

Another improvement to our analysis would be to monitor more carefully, how exactly the galaxies lose their gas. We did not analyse the AGN interactions inside galaxies. An idea for doing this would be to trace the outflowing flux from a specific galaxy and compare it to the SN and AGN activity, as well as constantly check if the ram pressure stripping criterion is fulfilled. For the ram pressure stripping criterion, we would need to take the inclination of the galaxy towards the ICM into account. A more sophisticated morphological study of the outflows could be performed. We would need to perform this analysis on a sample of galaxies. Another point is that the galactic physics is strongly dependent on our galaxy formation model. Different galaxy formation models show huge differences among different simulation codes (as discussed in section 3.8.3). We would need to carefully compare the outputs of different simulations and find relations to the underlying galaxy formation modules. Moreover, tidal interactions between the cluster and a galaxy can potentially strip gas from galaxies, which we also have not investigated.

We only analyse one cluster from the simulation, which is the fifth most massive one. This prevents us from making general statements about the magnetic field evolution in the ICM, as we are heavily biased towards more massive clusters. These clusters experience mergers at an increased rate. Additionally, the AGN in high mass clusters has more powerful outputs compared to lower mass clusters (as discussed in section 2.4.3), which can modify the magnetic field evolution. Furthermore, galaxy clusters are not completely self-similar. Each cluster has a unique history and appearance. Therefore, our analysis could be heavily biased towards exactly this cluster, which we analysed. A next step would be to simulate a sample of clusters and analyse all of them in order to make more general statements about the magnetic field evolution.

Our analysis has shown how important it is to consider the evolution of galaxies in order to understand the evolution of magnetic fields in the ICM. The interplay of magnetic fields in galaxies and the ICM can yield a faster growth of the magnetic field in the ICM, compared to only considering non-radiative approaches. Our analysis has also shown how important it is to simulate environmental effects. Large contributions to the magnetic field in the ICM come from pre-enriched merging substructures. However, in order to get an unambiguous picture, a more sophisticated analysis is required to prove our hypothesis.

A Appendix

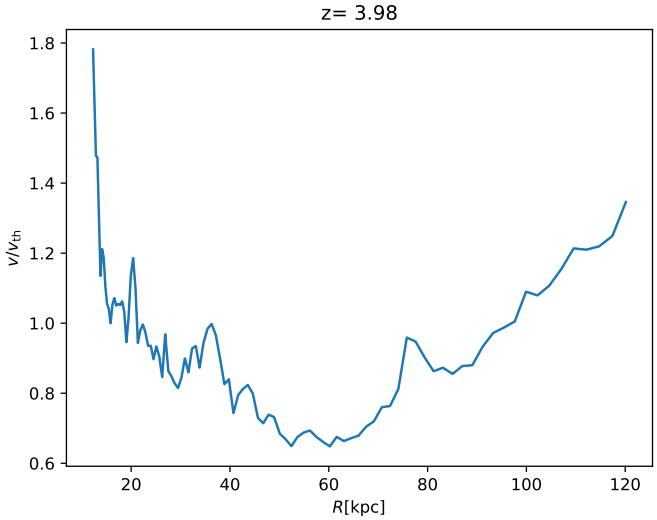

(a) The radiative run.

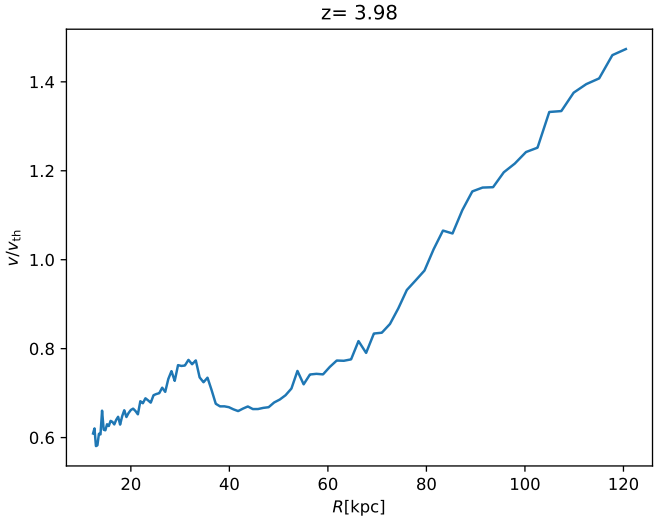

(b) The non-radiative run.

Figure A.1: Radial profiles of the zoom12 run within $R < R_{200}(z = 3.98) = 120$kpc of the ratio of turbulent velocities, computed as the gas velocities subtracted by the center of mass velocity of the cluster and the thermal gas velocity, computed from the internal energy of the gas.

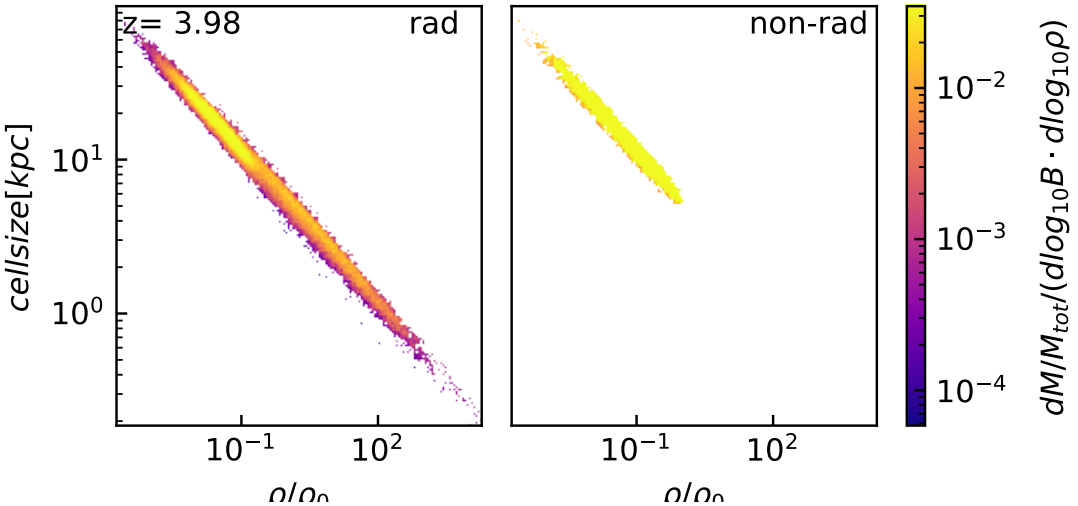

Figure A.2: Histogram of the cellsizes vs. normalised densities in the zoom12 radiative (left) and non-radiative (right) run at $z = 3.98$. The normalisation $\rho_0 = 4.05 \cdot 10^{-25}$g/cm^{-3} corresponds to the star forming threshold, such that below 1, we are looking at the ICM and above 1, we are looking at the ISM.

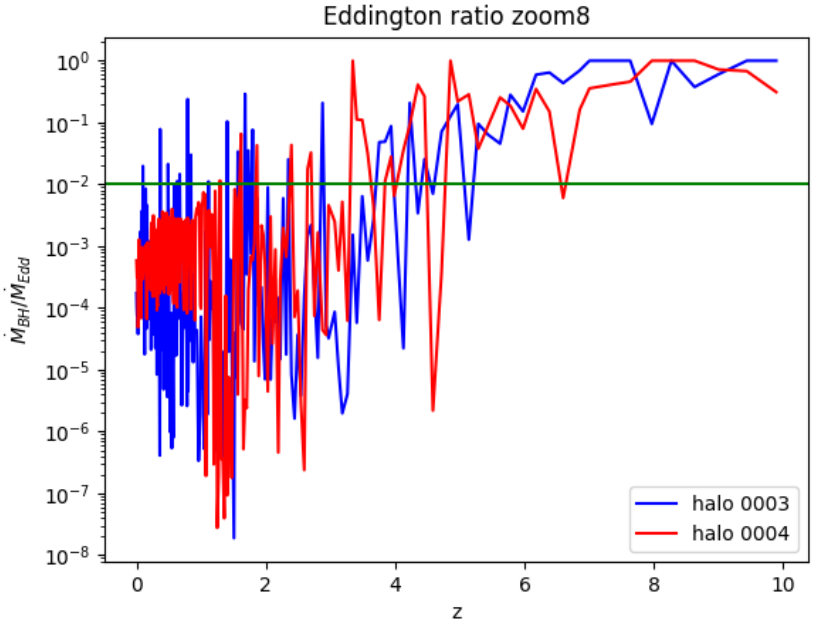

Figure A.3: The ratio of the actual black hole accretion rate, $\dot{M}_{\rm BH}$, and the Eddington accretion rate, $\dot{M}_{\rm Edd}$. We show the ratio for the central AGN of halo3 and halo4 (analysed in this thesis) of the zoom8 run. The green, horizontal line at $\dot{M}_{\rm BH}/\dot{M}_{\rm Edd} = 10^{-2}$ indicates the differentiation between quasar mode feedback ($\dot{M}_{\rm BH}/\dot{M}_{\rm Edd} > 10^{-2}$) and radio mode feedback ($\dot{M}_{\rm BH}/\dot{M}_{\rm Edd} < 10^{-2}$). For $z < 2$, radio mode feedback is the dominant feedback channel in halo4.

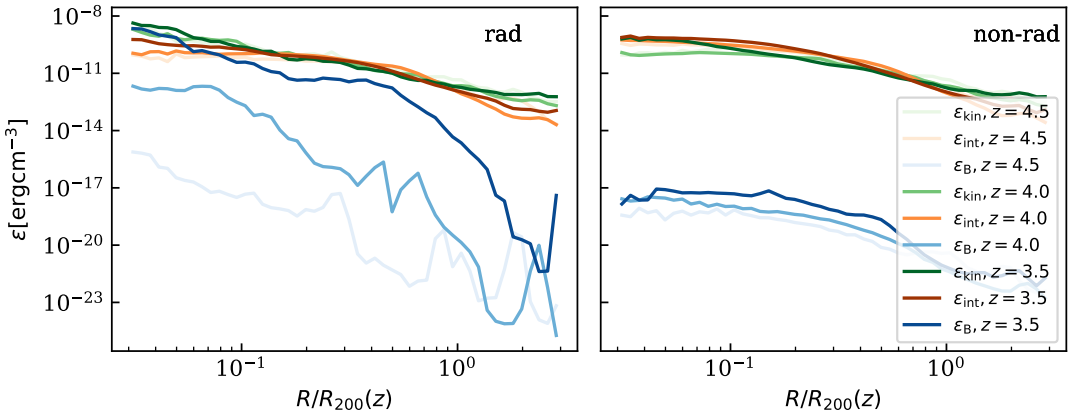

Figure A.4: Radial profiles for the magnetic (blue), kinetic (red) and internal (green) energy densities within $3 \cdot R_{200}(z)$. We show the radiative run, on the left, and the non-radiative run on the right. Different color shades are indicated with the color scheme and display different redshifts: $z = 4.5, 4.0, 3.5$. We calculate the kinetic energy density by subtracting the center of mass velocity from all cells: $\epsilon_{\rm kin} = 0.5 \cdot (\mathbf{v} - \mathbf{v_{CM}})^2 \cdot \rho$.

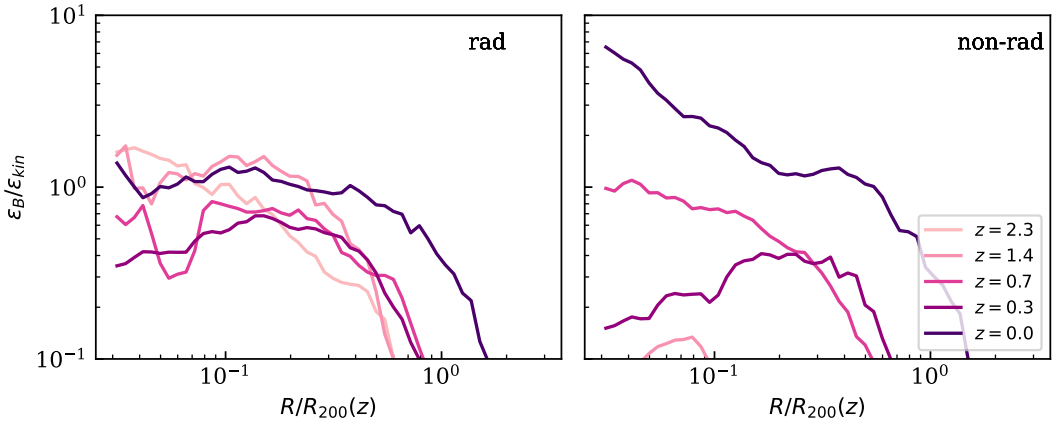

Figure A.5: Radial profiles for the ratio magnetic energy density over kinetic energy density within $3 \cdot R_{200}(z)$. We show the radiative run, on the left, and the non-radiative run on the right. Different color shades are indicated with the color scheme and display different redshifts: $z = 2.3, 1.4, 0.7, 0.3, 0.0$. We calculate the kinetic energy density by subtracting the center of mass velocity from all cells: $\epsilon_{\rm kin} = 0.5 \cdot (\mathbf{v} - \mathbf{v_{CM}})^2 \cdot \rho$.

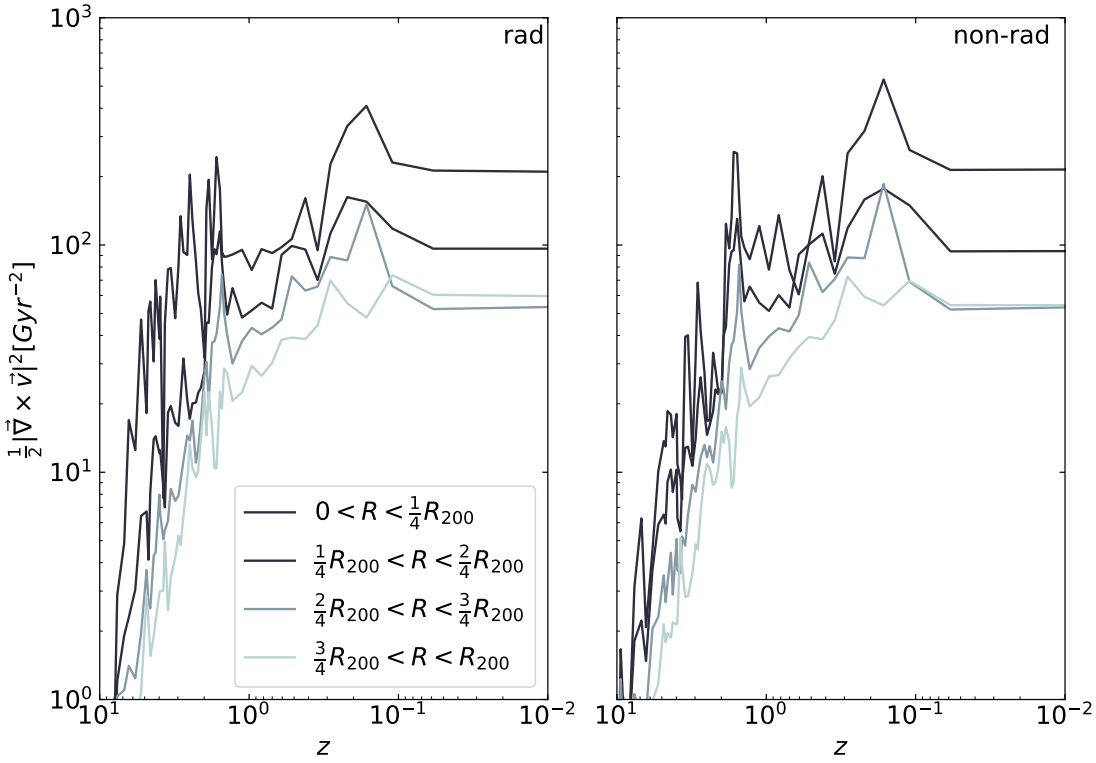

Figure A.6: Zoom in on figure 18. The mass weighted enstrophy evolution with time (see equation 23). We show different radial bins in units of the virial radius $R_{200}(z)$, indicated with the color scheme. The radiative run is shown on the left and the non-radiative run is shown on the right. The star forming regions are excluded from the ICM. Before the collapse of the protocluster at $z = 9.5$, we use the complete high resolution region to compute the enstrophy.

References

Abadi, M. G., Moore, B., & Bower, R. G. (1999, October). Ram pressure stripping of spiral galaxies in clusters. , *308*(4), 947-954. doi: 10.1046/j.1365-8711.1999.02715.x

Abel, T., Bryan, G. L., & Norman, M. L. (2002, January). The Formation of the First Star in the Universe. *Science*, *295*(5552), 93-98. doi: 10.1126/science.295.5552.93

Adduci Faria, S., Barai, P., & de Gouveia Dal Pino, E. M. (2020, August). Cosmic magnetic fields from cosmological simulations. *Boletin de la Asociacion Argentina de Astronomia La Plata Argentina*, *61C*, 80-80.

Aghanim, N., Akrami, Y., Ashdown, M., Aumont, J., Baccigalupi, C., Ballardini, M., ... Zonca, A. (2020, sep). iplanck/i2018 results. *Astronomy &amp Astrophysics*, *641*, A6. Retrieved from https://doi.org/10.1051%2F0004-6361%2F201833910 doi: 10.1051/0004-6361/201833910

Aghanim, N., de Luca, A., Bouchet, F. R., Gispert, R., & Puget, J. L. (1997, September). Cosmology with Sunyaev-Zeldovich observations from space. , *325*, 9-18.

Akamatsu, H., Inoue, S., Sato, T., Matsusita, K., Ishisaki, Y., & Sarazin, C. L. (2013, August). Suzaku X-Ray Observations of the Accreting NGC 4839 Group of Galaxies and a Radio Relic in the Coma Cluster. , *65*, 89. doi: 10.1093/pasj/65.4.89

Andreasyan, R. R. (1996, January). Mechanism of formation of a dipole magnetic field in the central regions of active galaxies. *Astrophysics*, *39*(1), 58-62. doi: 10.1007/BF02044955

Angulo, R. E., Springel, V., White, S. D. M., Jenkins, A., Baugh, C. M., & Frenk, C. S. (2012, November). Scaling relations for galaxy clusters in the Millennium-XXL simulation. , *426*(3), 2046-2062. doi: 10.1111/j.1365-2966.2012.21830.x

Asgari-Targhi, M., & Berger, M. A. (2009). Writhe in the stretch-twist-fold dynamo. *Geophysical & Astrophysical Fluid Dynamics*, *103*(1), 69-87. Retrieved from https://doi.org/10.1080/03091920802531791 doi: 10.1080/03091920802531791

Balsara, D. S., Kim, J., Mac Low, M.-M., & Mathews, G. J. (2004, December). Amplification of Interstellar Magnetic Fields by Supernova-driven Turbulence. , *617*(1), 339-349. doi: 10.1086/425297

Barkana, R., & Loeb, A. (1999, September). The Photoevaporation of Dwarf Galaxies during Reionization. , *523*(1), 54-65. doi: 10.1086/307724

Barkana, R., & Loeb, A. (2001, July). In the beginning: the first sources of light and the reionization of the universe. , *349*(2), 125-238. doi: 10.1016/S0370-1573(01)00019-9

Barnes, D. J., Vogelsberger, M., Kannan, R., Marinacci, F., Weinberger, R., Springel, V., ... McDonald, M. (2018, December). A census of cool-core galaxy clusters in IllustrisTNG. , *481*(2), 1809-1831. doi: 10.1093/mnras/sty2078

Barnes, J., & Hut, P. (1986, December). A hierarchical O(N log N) force-calculation algorithm. , *324*(6096), 446-449. doi: 10.1038/324446a0

Bartelmann, M. (2012). *Cosmology.* University Lecture.

Basu, A., & Sur, S. (2021, September). Properties of Polarized Synchrotron Emission from Fluctuation Dynamo Action—II. Effects of Turbulence Driving in the ICM and Beam Smoothing. *Galaxies*, *9*(3), 62. doi: 10.3390/galaxies9030062

Baugh, C. M., Lacey, C. G., Frenk, C. S., Granato, G. L., Silva, L., Bressan, A., ... Cole, S. (2005, January). Can the faint submillimetre galaxies be explained in the Λ cold dark matter model? , *356*(3), 1191-1200. doi: 10.1111/j.1365-2966.2004.08553.x

Beck, R., & Krause, M. (2005, July). Revised equipartition and minimum energy formula for magnetic field strength estimates from radio synchrotron observations. *Astronomische Nachrichten*, *326*(6), 414-427. doi: 10.1002/asna.200510366

Bennett, J. S., & Sijacki, D. (2022, July). A disturbing FABLE of mergers, feedback, turbulence, and mass biases in simulated galaxy clusters. , *514*(1), 313-328. doi: 10.1093/mnras/stac1216

Beresnyak, A. (2012, January). Universal Nonlinear Small-Scale Dynamo. , *108*(3), 035002. doi: 10.1103/PhysRevLett.108.035002

Berlok, T. (2022, September). Hydromagnetic waves in an expanding universe - cosmological MHD code tests using analytic solutions. , *515*(3), 3492-3511. doi: 10.1093/mnras/stac1882

Biermann, L. (1950, January). Über den Ursprung der Magnetfelder auf Sternen und im interstellaren Raum (miteinem Anhang von A. Schlüter). *Zeitschrift Naturforschung Teil A*, *5*, 65.

Biffi, V., Borgani, S., Murante, G., Rasia, E., Planelles, S., Granato, G. L., ... Dolag, K. (2016, August). On the Nature of Hydrostatic Equilibrium in Galaxy Clusters. , *827*(2), 112. doi: 10.3847/0004-637X/827/2/112

Biffi, V., Planelles, S., Borgani, S., Fabjan, D., Rasia, E., Murante, G., ... Beck, A. M. (2017, June). The history of chemical enrichment in the intracluster medium from cosmological simulations. , *468*(1), 531-548. doi: 10.1093/mnras/stx444

Biffi, V., ZuHone, J. A., Mroczkowski, T., Bulbul, E., & Forman, W. (2022, July). The velocity structure of the intracluster medium during a major merger: Simulated microcalorimeter observations. , *663*, A76. doi: 10.1051/0004-6361/202142764

Bîrzan, L., Rafferty, D. A., McNamara, B. R., Wise, M. W., & Nulsen, P. E. J. (2004, June). A Systematic Study of Radio-induced X-Ray Cavities in Clusters, Groups, and Galaxies. , *607*(2), 800-809. doi: 10.1086/383519

Block, L. P. (1978, May). A Double Layer Review (Paper dedicated to Professor Hannes Alfvén on the occasion of his 70th birthday, 30 May 1978). , *55*(1), 59-83. doi: 10.1007/BF00642580

Bookbinder, J., Cowie, L. L., Ostriker, J. P., Krolik, J. H., & Rees, M. (1980, May). The contribution of young galaxies to the X-ray background. , *237*, 647-654. doi: 10.1086/157911

Boselli, A., Fossati, M., & Sun, M. (2022, December). Ram pressure stripping in high-density environments. , *30*(1), 3. doi: 10.1007/s00159-022-00140-3

Botteon, A., van Weeren, R. J., Brunetti, G., Vazza, F., Shimwell, T. W., Brüggen, M., ... Gastaldello, F. (2022, November). Magnetic fields and relativistic electrons fill entire galaxy cluster. *Science Advances*, *8*(44), eabq7623. doi: 10.1126/sciadv.abq7623

Bresci, V., Gremillet, L., & Lemoine, M. (2022, March). Saturation of the asymmetric current filamentation instability under conditions relevant to relativistic shock precursors. , *105*(3), 035202. doi: 10.1103/PhysRevE.105.035202

Bret, A., Gremillet, L., & Dieckmann, M. E. (2010, December). Multidimensional electron beam-plasma instabilities in the relativistic regime. *Physics of Plasmas*, *17*(12), 120501. doi: 10.1063/1.3514586

Brunetti, G., & Jones, T. W. (2014, March). Cosmic Rays in Galaxy Clusters and Their Nonthermal Emission. *International Journal of Modern Physics D*, *23*(4), 1430007-98. doi: 10.1142/S0218271814300079

Butcher, H., & Oemler, J., A. (1984, October). The evolution of galaxies in clusters. V. A study of populations since Z 0.5. , *285*, 426-438. doi: 10.1086/162519

Cagas, P., Hakim, A., Scales, W., & Srinivasan, B. (2017, November). Nonlinear saturation of the Weibel instability. *Physics of Plasmas*, *24*(11), 112116. doi: 10.1063/1.4994682

Carteret, Y., Schleicher, D., & Schober, J. (2023, March). Small-scale dynamo with finite correlation times. *arXiv e-prints*, arXiv:2303.01097. doi: 10.48550/arXiv.2303.01097

Cassano, R., & Brunetti, G. (2005, March). Cluster mergers and non-thermal phenomena: a statistical magneto-turbulent model. , *357*(4), 1313-1329. doi: 10.1111/j.1365-2966.2005.08747.x

Cavaliere, A., & Fusco-Femiano, R. (1976, May). X-rays from hot plasma in clusters of galaxies. , *49*, 137-144.

Chabrier, G. (2003, July). Galactic Stellar and Substellar Initial Mass Function. , *115*(809), 763-795. doi: 10.1086/376392

Chen, Y., Reiprich, T. H., Böhringer, H., Ikebe, Y., & Zhang, Y. Y. (2007, May). Statistics of X-ray observables for the cooling-core and non-cooling core galaxy clusters. , *466*(3), 805-812. doi: 10.1051/0004-6361:20066471

Cho, J. (2015, October). Origin of Magnetic Fields in the Intracluster Medium. In N. V. Pogorelov, E. Audit, & G. P. Zank (Eds.), *Numerical modeling of space plasma flows astronum-2014* (Vol. 498, p. 53).

Churazov, E., Forman, W., Jones, C., & Böhringer, H. (2003, June). XMM-Newton Observations of the Perseus Cluster. I. The Temperature and Surface Brightness Structure. , *590*(1), 225-237. doi: 10.1086/374923

Clarke, T. E., Kronberg, P. P., & Böhringer, H. (2001, February). A New Radio-X-Ray Probe of Galaxy Cluster Magnetic Fields. , *547*(2), L111-L114. doi: 10.1086/318896

Dadina, M., Cappi, M., Piconcelli, E., Zappacosta, L., Bianchi, S., Vignali, C., ... Torresi, E. (2022, November). Probing AGN feedback in the most luminous QSO at cosmic noon. , *93*(2-3), 56. doi: 10.36116/MEMSAIT_93N2_3.2022.7

de Gouveia Dal Pino, E. M., Melioli, C., D'Ercole, A., Brighenti, F., & Raga, A. C. (2009, August). Supernova Explosions and the Triggering of Galactic Fountains and Outflows. In *Revista mexicana de astronomia y astrofisica conference series* (Vol. 36, p. 17-24).

De Lucia, G., & Blaizot, J. (2007, February). The hierarchical formation of the brightest cluster galaxies. , *375*(1), 2-14. doi: 10.1111/j.1365-2966.2006.11287.x

Doi, K., & Susa, H. (2011, November). Generation of a Seed Magnetic Field around First Stars: The Biermann Battery Effect. , *741*(2), 93. doi: 10.1088/0004-637X/741/2/93

Dolag, K., Borgani, S., Murante, G., & Springel, V. (2009, October). Substructures in hydrodynamical cluster simulations. , *399*(2), 497-514. doi: 10.1111/j.1365-2966.2009.15034.x

Donnari, M., Pillepich, A., Joshi, G. D., Nelson, D., Genel, S., Marinacci, F., ... Hernquist, L. (2021, January). Quenched fractions in the IllustrisTNG simulations: the roles of AGN feedback, environment, and pre-processing. , *500*(3), 4004-4024. doi: 10.1093/mnras/staa3006

Donnert, J., Vazza, F., Brüggen, M., & ZuHone, J. (2018, December). Magnetic Field Amplification in Galaxy Clusters and Its Simulation. , *214*(8), 122. doi: 10.1007/s11214-018-0556-8

Durrive, J. B., & Langer, M. (2015, October). Intergalactic magnetogenesis at Cosmic Dawn by photoionization. , *453*(1), 345-356. doi: 10.1093/mnras/stv1578

Ehlert, K., Weinberger, R., Pfrommer, C., & Springel, V. (2021, May). Connecting turbulent velocities and magnetic fields in galaxy cluster simulations with active galactic nuclei jets. , *503*(1), 1327-1344. doi: 10.1093/mnras/stab551

Ensslin, T. A., Biermann, P. L., Klein, U., & Kohle, S. (1998, April). Cluster radio relics as a tracer of shock waves of the large-scale structure formation. , *332*, 395-409. doi: 10.48550/arXiv.astro-ph/9712293

Fabjan, D., Borgani, S., Tornatore, L., Saro, A., Murante, G., & Dolag, K. (2010, January). Simulating the effect of active galactic nuclei feedback on the metal enrichment of galaxy clusters. , *401*(3), 1670-1690. doi: 10.1111/j.1365-2966.2009.15794.x

Field, G. B., & Carroll, S. M. (2000, November). Cosmological magnetic fields from primordial helicity. , *62*(10), 103008. doi: 10.1103/PhysRevD.62.103008

Fujita, Y., Tawa, N., Hayashida, K., Takizawa, M., Matsumoto, H., Okabe, N., & Reiprich, T. H. (2008, January). High Metallicity of the X-Ray Gas Up to the Virial Radius of a Binary Cluster of Galaxies: Evidence of Galactic Superwinds at High-Redshift. , *60*, S343. doi: 10.1093/pasj/60.sp1.S343

Furlanetto, S. R., & Loeb, A. (2001, August). Intergalactic Magnetic Fields from Quasar Outflows. , *556*(2), 619-634. doi: 10.1086/321630

Gao, L., Navarro, J. F., Cole, S., Frenk, C. S., White, S. D. M., Springel, V., ... Neto, A. F. (2008, June). The redshift dependence of the structure of massive Λ cold dark matter haloes. , *387*(2), 536-544. doi: 10.1111/j.1365-2966.2008.13277.x

Garaldi, E., Pakmor, R., & Springel, V. (2021, April). Magnetogenesis around the first galaxies: the impact of different field seeding processes on galaxy formation. , *502*(4), 5726-5744. doi: 10.1093/mnras/stab086

Gaspari, M., & Churazov, E. (2013, November). Constraining turbulence and conduction in the hot ICM through density perturbations. , *559*, A78. doi: 10.1051/0004-6361/201322295

Gent, F. A., Mac Low, M.-M., Korpi-Lagg, M. J., & Singh, N. K. (2023, February). The Small-scale Dynamo in a Multiphase Supernova-driven Medium. , *943*(2), 176. doi: 10.3847/1538-4357/acac20

Giacintucci, S., Markevitch, M., Cassano, R., Venturi, T., Clarke, T. E., & Brunetti, G. (2017, June). Occurrence of Radio Minihalos in a Mass-limited Sample of Galaxy Clusters. , *841*(2), 71. doi: 10.3847/1538-4357/aa7069

Gnedin, N. Y., Ferrara, A., & Zweibel, E. G. (2000, August). Generation of the Primordial Magnetic Fields during Cosmological Reionization. , *539*(2), 505-516. doi: 10.1086/309272

Gnedin, N. Y., & Ostriker, J. P. (1997, September). Reionization of the Universe and the Early Production of Metals. , *486*(2), 581-598. doi: 10.1086/304548

Governato, F., Zolotov, A., Pontzen, A., Christensen, C., Oh, S. H., Brooks, A. M., ... Wadsley, J. (2012, May). Cuspy no more: how outflows affect the central dark matter and baryon distribution in Λ cold dark matter galaxies. , *422*(2), 1231-1240. doi: 10.1111/j.1365-2966.2012.20696.x

Govoni, F., Murgia, M., Vacca, V., Loi, F., Girardi, M., Gastaldello, F., ... Vazza, F. (2017, July). Sardinia Radio Telescope observations of Abell 194. The intra-cluster magnetic field power spectrum. , *603*, A122. doi: 10.1051/0004-6361/201630349

Grasso, D., & Rubinstein, H. R. (2001, July). Magnetic fields in the early Universe. , *348*(3), 163-266. doi: 10.1016/S0370-1573(00)00110-1

Gunn, J. E., & Gott, I., J. Richard. (1972, August). On the Infall of Matter Into Clusters of Galaxies and Some Effects on Their Evolution. , *176*, 1. doi: 10.1086/151605

Gutcke, T. A., Pakmor, R., Naab, T., & Springel, V. (2021, March). LYRA - I. Simulating the multiphase ISM of a dwarf galaxy with variable energy supernovae from individual stars. , *501*(4), 5597-5615. doi: 10.1093/mnras/staa3875

Halenka, V., & Miller, C. J. (2020, October). Testing emergent gravity with mass densities of galaxy clusters. , *102*(8), 084007. doi: 10.1103/PhysRevD.102.084007

Hanayama, H., Takahashi, K., Kotake, K., Oguri, M., Ichiki, K., & Ohno, H. (2005, November). Biermann Mechanism in Primordial Supernova Remnant and Seed Magnetic Fields. , *633*(2), 941-945. doi: 10.1086/491575

Hasan, F., Burchett, J. N., Abeyta, A., Hellinger, D., Mandelker, N., Primack, J. R., ... Nagai, D. (2023, March). How Cosmic Web Environment Affects Galaxy Quenching Across Cosmic Time. *arXiv e-prints*, arXiv:2303.08088.

Heckman, T. M., Armus, L., & Miley, G. K. (1990, December). On the Nature and Implications of Starburst-driven Galactic Superwinds. , *74*, 833. doi: 10.1086/191522

Heinrich, A. M., Chen, Y.-H., Heinz, S., Zhuravleva, I., & Churazov, E. (2021, August). Constraining black hole feedback in galaxy clusters from X-ray power spectra. , *505*(3), 4646-4654. doi: 10.1093/mnras/stab1557

Helmholtz, H. (1858). Über integrale der hydrodynamischen gleichungen, welche den wirbelbewegungen entsprechen. , *1858*(55), 25–55. Retrieved 2022-12-09, from https://doi.org/10.1515/crll.1858.55.25 doi: doi:10.1515/crll.1858.55.25

Henden, N. A. (2019). Exploring galaxy clusters and groups with cosmological simulations. Retrieved from https://www.repository.cam.ac.uk/handle/1810/295064 doi: 10.17863/CAM.42142

Henden, N. A., Puchwein, E., Shen, S., & Sijacki, D. (2018, October). The FABLE simulations: a feedback model for galaxies, groups, and clusters. , *479*(4), 5385-5412. doi: 10.1093/mnras/sty1780

Hernquist, L., & Springel, V. (2003, June). An analytical model for the history of cosmic star formation. , *341*(4), 1253-1267. doi: 10.1046/j.1365-8711.2003.06499.x

Hitomi Collaboration. (2016, July). The quiescent intracluster medium in the core of the Perseus cluster. , *535*(7610), 117-121. doi: 10.1038/nature18627

Höller, H., Stöckl, J., Benson, A., Haider, M., Steinhauser, D., Lovisari, L., & Pranger, F. (2014, September). Metal distribution in the intracluster medium: a comprehensive numerical study of twelve galaxy clusters. , *569*, A31. doi: 10.1051/0004-6361/201323362

Hou, A., Parker, L. C., & Harris, W. E. (2014, July). The pre-processing of subhaloes in SDSS groups and clusters. , *442*(1), 406-418. doi: 10.1093/mnras/stu829

Hou, M., Li, Z., Jones, C., Forman, W., & Su, Y. (2021, October). X-Ray Constraints on the Hot Gas Content of Early-type Galaxies in Virgo. , *919*(2), 141. doi: 10.3847/1538-4357/ac1344

Hudson, D. S., Mittal, R., Reiprich, T. H., Nulsen, P. E. J., Andernach, H., & Sarazin, C. L. (2010, April). What is a cool-core cluster? a detailed analysis of the cores of the X-ray flux-limited HIFLUGCS cluster sample. , *513*, A37. doi: 10.1051/0004-6361/200912377

Hughes, D. H., Serjeant, S., Dunlop, J., Rowan-Robinson, M., Blain, A., Mann, R. G., ... Jenness, T. (1998, July). High-redshift star formation in the Hubble Deep Field revealed by a submillimetre-wavelength survey. , *394*(6690), 241-247. doi: 10.1038/28328

Ito, K., Kashikawa, N., Toshikawa, J., Overzier, R., Tanaka, M., Kubo, M., ... Huang, S. (2019, June). The Brightest UV-selected Galaxies in Protoclusters at z $\sim$ 4: Ancestors of Brightest Cluster Galaxies? , *878*(1), 68. doi: 10.3847/1538-4357/ab1f0c

Jáchym, P., Kenney, J. D. P., Sun, M., Combes, F., Cortese, L., Scott, T. C., ... Fumagalli, M. (2019, October). ALMA Unveils Widespread Molecular Gas Clumps in the Ram Pressure Stripped Tail of the Norma Jellyfish Galaxy. , *883*(2), 145. doi: 10.3847/1538-4357/ab3e6c

Jappsen, A.-K., Mac Low, M.-M., Glover, S. C. O., Klessen, R. S., & Kitsionas, S. (2009, April). Star Formation at Very Low Metallicity. V. The Greater Importance of Initial Conditions Compared to Metallicity Thresholds. , *694*(2), 1161-1170. doi: 10.1088/0004-637X/694/2/1161

Kauffmann, G., Heckman, T. M., White, S. D. M., Charlot, S., Tremonti, C., Peng, E. W., ... York, D. (2003, May). The dependence of star formation history and internal structure on stellar mass for 10^5 low-redshift galaxies. , *341*(1), 54-69. doi: 10.1046/j.1365-8711.2003.06292.x

Kazantsev, A. P. (1968, May). Enhancement of a Magnetic Field by a Conducting Fluid. *Soviet Journal of Experimental and Theoretical Physics*, *26*, 1031.

Kolmogorov, A. (1941, January). The Local Structure of Turbulence in Incompressible Viscous Fluid for Very Large Reynolds' Numbers. *Akademiia Nauk SSSR Doklady*, *30*, 301-305.

Koudmani, S., Henden, N. A., & Sijacki, D. (2021, May). A little FABLE: exploring AGN feedback in dwarf galaxies with cosmological simulations. , *503*(3), 3568-3591. doi: 10.1093/mnras/stab677

Kraichman, M. (1966, May). The near field beyond a perfectly conducting plane screen with a small circular aperture. *IEEE Transactions on Antennas and Propagation*, *14*(3), 389-390. doi: 10.1109/TAP.1966.1138691

Kravtsov, A. V., & Borgani, S. (2012, September). Formation of Galaxy Clusters. , *50*, 353-409. doi: 10.1146/annurev-astro-081811-125502

Kubo, M., Umehata, H., Matsuda, Y., Kajisawa, M., Steidel, C. C., Yamada, T., ... Matsuda, K. (2021, September). A Massive Quiescent Galaxy Confirmed in a Protocluster at z = 3.09. , *919*(1), 6. doi: 10.3847/1538-4357/ac0cf8

Kulsrud, R. M., Cen, R., Ostriker, J. P., & Ryu, D. (1997, May). The Protogalactic Origin for Cosmic Magnetic Fields. , *480*(2), 481-491. doi: 10.1086/303987

Kunz, M. W., Jones, T. W., & Zhuravleva, I. (2022, May). Plasma physics of the intracluster medium. *arXiv e-prints*, arXiv:2205.02489.

Lapi, A., Raimundo, S., Aversa, R., Cai, Z. Y., Negrello, M., Celotti, A., ... Danese, L. (2014, February). The Coevolution of Supermassive Black Holes and Massive Galaxies at High Redshift. , *782*(2), 69. doi: 10.1088/0004-637X/782/2/69

Laporte, C. F. P., White, S. D. M., Naab, T., & Gao, L. (2013, October). The growth in size and mass of cluster galaxies since z = 2. , *435*(2), 901-909. doi: 10.1093/mnras/stt912

Lehnert, M. D., Heckman, T. M., & Weaver, K. A. (1999, oct). Very extended x-ray and h emission in m82: Implications for the superwind phenomenon. *The Astrophysical Journal*, *523*(2), 575. Retrieved from https://dx.doi.org/10.1086/307762 doi: 10.1086/307762

Lewis, A., & Bridle, S. (2002). Cosmological parameters from CMB and other data: A Monte Carlo approach. , *66*, 103511. doi: 10.1103/PhysRevD.66.103511

Lewis, A., Challinor, A., & Lasenby, A. (2000). Efficient computation of CMB anisotropies in closed FRW models. , *538*, 473-476. doi: 10.1086/309179

Liu, Y., Kretschmer, M., & Teyssier, R. (2022, July). A subgrid turbulent mean-field dynamo model for cosmological galaxy formation simulations. , *513*(4), 6028-6041. doi: 10.1093/mnras/stac1266

Lobanov, A. P. (1998, February). Ultracompact jets in active galactic nuclei. , *330*, 79-89. doi: 10.48550/arXiv.astro-ph/9712132

Madau, P., Ferrara, A., & Rees, M. J. (2001, July). Early Metal Enrichment of the Intergalactic Medium by Pregalactic Outflows. , *555*(1), 92-105. doi: 10.1086/321474

Mandelbaum, R., Seljak, U., Kauffmann, G., Hirata, C. M., & Brinkmann, J. (2006, May). Galaxy halo masses and satellite fractions from galaxy-galaxy lensing in the Sloan Digital Sky Survey: stellar mass, luminosity, morphology and environment dependencies. , *368*(2), 715-731. doi: 10.1111/j.1365-2966.2006.10156.x

Marinacci, F., Vogelsberger, M., Mocz, P., & Pakmor, R. (2015, November). The large-scale properties of simulated cosmological magnetic fields. , *453*(4), 3999-4019. doi: 10.1093/mnras/stv1692

Markevitch, M., & Vikhlinin, A. (2007, May). Shocks and cold fronts in galaxy clusters. , *443*(1), 1-53. doi: 10.1016/j.physrep.2007.01.001

Martin-Alvarez, S., Devriendt, J., Slyz, A., Sijacki, D., Richardson, M. L. A., & Katz, H. (2022, July). Towards convergence of turbulent dynamo amplification in cosmological simulations of galaxies. , *513*(3), 3326-3344. doi: 10.1093/mnras/stac1099

Martín-Navarro, I., Burchett, J. N., & Mezcua, M. (2019, October). Quantifying the Effect of Black Hole Feedback from the Central Galaxy on the Satellite Populations of Groups and Clusters. , *884*(2), L45. doi: 10.3847/2041-8213/ab4885

McDonald, M., Allen, S. W., Bayliss, M., Benson, B. A., Bleem, L. E., Brodwin, M., ... Murray, S. S. (2017, July). The Remarkable Similarity of Massive Galaxy Clusters from z $\sim$ 0 to z $\sim$ 1.9. , *843*(1), 28. doi: 10.3847/1538-4357/aa7740

McNamara, B. R., & Nulsen, P. E. J. (2012, May). Mechanical feedback from active galactic nuclei in galaxies, groups and clusters. *New Journal of Physics*, *14*(5), 055023. doi: 10.1088/1367-2630/14/5/055023

Meng, X.-H., & Dou, X. (2009, August). Friedmann Cosmology with Bulk Viscosity: A Concrete Model for Dark Energy. *Communications in Theoretical Physics*, *52*(2), 377-382. doi: 10.1088/0253-6102/52/2/36

Meng, X.-H., Ren, J., & Hu, M.-G. (2005, September). Friedmann cosmology with a generalized equation of state and bulk viscosity. *arXiv e-prints*, astro-ph/0509250. doi: 10.48550/arXiv.astro-ph/0509250

Miniati, F., & Beresnyak, A. (2015a, July). Self-similar energetics in large clusters of galaxies. , *523*(7558), 59-62. doi: 10.1038/nature14552

Miniati, F., & Beresnyak, A. (2015b, August). Self similarity of turbulence and dynamo action in the largest cosmic structures. In *Iau general assembly* (Vol. 29, p. 2250507).

Miranda, O. D., Opher, M., & Opher, R. (1998, December). Seed magnetic Fields Generated by Primordial Supernova Explosions. , *301*(2), 547-550. doi: 10.1046/j.1365-8711.1998.02041.x

Mohr, J. J., Mathiesen, B., & Evrard, A. E. (1999, June). Properties of the Intracluster Medium in an Ensemble of Nearby Galaxy Clusters. , *517*(2), 627-649. doi: 10.1086/307227

Mouschovias, T. C. (1976, June). Nonhomologous contraction and equilibria of self-gravitating, magnetic interstellar clouds embedded in an intercloud medium: star formation. I. Formulation of the problem and method of solution. , *206*, 753-767. doi: 10.1086/154436

Mtchedlidze, S., Domínguez-Fernández, P., Du, X., Brandenburg, A., & Kahniashvili, T. (2021, June). Primordial Magnetic Fields through Large Scale Structure. In *American astronomical society meeting abstracts* (Vol. 53, p. 109.09).

Mtchedlidze, S., Domínguez-Fernández, P., Du, X., Brandenburg, A., Kahniashvili, T., O'Sullivan, S., ... Brüggen, M. (2022, April). Evolution of Primordial Magnetic Fields during Large-scale Structure Formation. , *929*(2), 127. doi: 10.3847/1538-4357/ac5960

Mutch, S. J., Croton, D. J., & Poole, G. B. (2013). The simplest model of galaxy formation – i. a formation history model of galaxy stellar mass growth. *Monthly Notices of the Royal Astronomical Society*, *435*, 2445-2459.

Nishikawa, H., & Liu, Y. (2018, January). Hyperbolic advection-diffusion schemes for high-Reynolds-number boundary-layer problems. *Journal of Computational Physics*, *352*, 23-51. doi: 10.1016/j.jcp.2017.09.039

Nobels, F. S. J., Schaye, J., Schaller, M., Bahé, Y. M., & Chaikin, E. (2022, October). The interplay between AGN feedback and precipitation of the intracluster medium in simulations of galaxy groups and clusters. , *515*(4), 4838-4859. doi: 10.1093/mnras/stac2061

O'Dea, K. P., Quillen, A. C., O'Dea, C. P., Tremblay, G. R., Snios, B. T., Baum, S. A., ... Voit, G. M. (2010, August). Hubble Space Telescope Far-ultraviolet Observations of Brightest Cluster Galaxies: The Role of Star Formation in Cooling Flows and BCG Evolution. , *719*(2), 1619-1632. doi: 10.1088/0004-637X/719/2/1619

Osinga, E., van Weeren, R. J., Andrade-Santos, F., Rudnick, L., Bonafede, A., Clarke, T., ... Röttgering, H. J. A. (2022, September). The detection of cluster magnetic fields via radio source depolarisation. , *665*, A71. doi: 10.1051/0004-6361/202243526

Pakmor, R., Bauer, A., & Springel, V. (2011, December). Magnetohydrodynamics on an unstructured moving grid. , *418*(2), 1392-1401. doi: 10.1111/j.1365-2966.2011.19591.x

Pakmor, R., Gómez, F. A., Grand, R. J. J., Marinacci, F., Simpson, C. M., Springel, V., ... White, S. D. M. (2017, August). Magnetic field formation in the Milky Way like disc galaxies of the Auriga project. , *469*(3), 3185-3199. doi: 10.1093/mnras/stx1074

Pakmor, R., & Springel, V. (2013, June). Simulations of magnetic fields in isolated disc galaxies. , *432*(1), 176-193. doi: 10.1093/mnras/stt428

Pakmor, R., van de Voort, F., Bieri, R., Gómez, F. A., Grand, R. J. J., Guillet, T., ... Springel, V. (2020, November). Magnetizing the circumgalactic medium of disc galaxies. , *498*(3), 3125-3137. doi: 10.1093/mnras/staa2530

Patej, A., & Loeb, A. (2015, January). A Simple Physical Model for the Gas Distribution in Galaxy Clusters. , *798*(1), L20. doi: 10.1088/2041-8205/798/1/L20

Perret, V., Renaud, F., Epinat, B., Amram, P., Bournaud, F., Contini, T., ... Lambert, J. C. (2014, February). Evolution of the mass, size, and star formation rate in high redshift merging galaxies. MIRAGE - A new sample of simulations with detailed stellar feedback. , *562*, A1. doi: 10.1051/0004-6361/201322395

Pfrommer, C. (2022). *The physics of galaxy clusters.* University Lecture.

Pfrommer, C., Springel, V., Enßlin, T. A., & Jubelgas, M. (2006, March). Detecting shock waves in cosmological smoothed particle hydrodynamics simulations. , *367*(1), 113-131. doi: 10.1111/j.1365-2966.2005.09953.x

Pfrommer, C., Werhahn, M., Pakmor, R., Girichidis, P., & Simpson, C. M. (2022, September). Simulating radio synchrotron emission in star-forming galaxies: small-scale magnetic dynamo and the origin of the far-infrared-radio correlation. , *515*(3), 4229-4264. doi: 10.1093/mnras/stac1808

Planelles, S., Borgani, S., Fabjan, D., Killedar, M., Murante, G., Granato, G. L., ... Dolag, K. (2014, February). On the role of AGN feedback on the thermal and chemodynamical properties of the hot intracluster medium. , *438*(1), 195-216. doi: 10.1093/mnras/stt2141

Powell, K. G., Roe, P. L., Linde, T. J., Gombosi, T. I., & De Zeeuw, D. L. (1999, September). A Solution-Adaptive Upwind Scheme for Ideal Magnetohydrodynamics. *Journal of Computational Physics*, *154*(2), 284-309. doi: 10.1006/jcph.1999.6299

Press, W. H., & Davis, M. (1982, August). How to identify and weigh virialized clusters of galaxies in a complete redshift catalog. , *259*, 449-473. doi: 10.1086/160183

Price, D. J. (2012, February). Resolving high Reynolds numbers in smoothed particle hydrodynamics simulations of subsonic turbulence. , *420*(1), L33-L37. doi: 10.1111/j.1745-3933.2011.01187.x

Prochaska, J. X., Gawiser, E., Wolfe, A. M., Castro, S., & Djorgovski, S. G. (2003, September). The Age-Metallicity Relation of the Universe in Neutral Gas: The First 100 Damped Lyα Systems. , *595*(1), L9-L12. doi: 10.1086/378945

Quilis, V., Moore, B., & Bower, R. (2000, June). Gone with the Wind: The Origin of S0 Galaxies in Clusters. *Science*, *288*(5471), 1617-1620. doi: 10.1126/science.288.5471.1617

Reblinsky, K. (2000). *Projection effects in clusters of galaxies* (Unpublished doctoral dissertation). Ludwig-Maximilians University of Munich, Germany.

Rees, M. J. (1987, September). The origin and cosmogonic implications of seed magnetic fields. , *28*, 197-206.

Rees, M. J., & Ostriker, J. P. (1977, June). Cooling, dynamics and fragmentation of massive gas clouds: clues to the masses and radii of galaxies and clusters. , *179*, 541-559. doi: 10.1093/mnras/179.4.541

Rincon, F. (2019). Dynamo theories. *Journal of Plasma Physics*, *85*(4), 205850401. doi: 10.1017/S0022377819000539

Roediger, E., Kraft, R. P., Nulsen, P., Churazov, E., Forman, W., Brüggen, M., & Kokotanekova, R. (2013, December). Viscous Kelvin-Helmholtz instabilities in highly ionized plasmas. , *436*(2), 1721-1740. doi: 10.1093/mnras/stt1691

Roh, S., Ryu, D., Kang, H., Ha, S., & Jang, H. (2019, October). Turbulence Dynamo in the Stratified Medium of Galaxy Clusters. , *883*(2), 138. doi: 10.3847/1538-4357/ab3aff

Rudnick, L. (2019). *The stormy life of galaxy clusters: astro version.* arXiv. Retrieved from https://arxiv.org/abs/1901.09448 doi: 10.48550/ARXIV.1901.09448

Ruppin, F., McDonald, M., Bleem, L. E., Allen, S. W., Benson, B. A., Calzadilla, M., ... Floyd, B. (2021, September). Stability of Cool Cores during Galaxy Cluster Growth: A Joint Chandra/SPT Analysis of 67 Galaxy Clusters along a Common Evolutionary Track Spanning 9 Gyr. , *918*(2), 43. doi: 10.3847/1538-4357/ac0bba

Ruppin, F., McDonald, M., Hlavacek-Larrondo, J., Bayliss, M., Bleem, L. E., Calzadilla, M., ... Tothill, N. (2022, July). Redshift Evolution of the Feedback / Cooling Equilibrium in the Core of 48 SPT Galaxy Clusters: A Joint ***Chandra***-SPT-ATCA analysis. *arXiv e-prints*, arXiv:2207.13351. doi: 10.48550/arXiv.2207.13351

Santini, P., Fontana, A., Castellano, M., Di Criscienzo, M., Merlin, E., Amorin, R., ... Shu, X. (2017, September). The Star Formation Main Sequence in the Hubble Space Telescope Frontier Fields. , *847*(1), 76. doi: 10.3847/1538-4357/aa8874

Sarazin, C. L. (1986, January). X-ray emission from clusters of galaxies. *Reviews of Modern Physics*, *58*(1), 1-115. doi: 10.1103/RevModPhys.58.1

Sarkar, K. C., Dey, A., & Sharma, P. (2022, October). Deprojection of X-ray data in galaxy clusters: confronting simulations with observations. , *516*(1), 992-1007. doi: 10.1093/mnras/stac2296

Sartorio, N. S., Fialkov, A., Hartwig, T., Mirouh, G. M., Izzard, R. G., Magg, M., ... Hendriks, D. D. (2023, March). Population III X-ray Binaries and their Impact on the Early Universe. *arXiv e-prints*, arXiv:2303.03435. doi: 10.48550/arXiv.2303.03435

Schawinski, K., Thomas, D., Sarzi, M., Maraston, C., Kaviraj, S., Joo, S.-J., ... Silk, J. (2007, December). Observational evidence for AGN feedback in early-type galaxies. , *382*(4), 1415-1431. doi: 10.1111/j.1365-2966.2007.12487.x

Schawinski, K., Urry, C. M., Simmons, B. D., Fortson, L., Kaviraj, S., Keel, W. C., ... Yi, S. K. (2014, May). The green valley is a red herring: Galaxy Zoo reveals two evolutionary pathways towards quenching of star formation in early- and late-type galaxies. , *440*(1), 889-907. doi: 10.1093/mnras/stu327

Schekochihin, A. A. (2022). *Mhd turbulence: A biased review.*

Schlickeiser, R., & Shukla, P. K. (2003, December). Cosmological Magnetic Field Generation by the Weibel Instability. , *599*(2), L57-L60. doi: 10.1086/381246

Schober, J., Schleicher, D., Federrath, C., Glover, S., Klessen, R. S., & Banerjee, R. (2012, August). The Small-scale Dynamo and Non-ideal Magnetohydrodynamics in Primordial Star Formation. , *754*(2), 99. doi: 10.1088/0004-637X/754/2/99

Schober, J., Schleicher, D. R. G., & Klessen, R. S. (2013, December). Magnetic field amplification in young galaxies. , *560*, A87. doi: 10.1051/0004-6361/201322185

Serra, P., Maccagni, F. M., Kleiner, D., Molnar, D., Ramatsoku, M., Loni, A., ... Verheijen, M. A. W. (2023, February). The MeerKAT Fornax Survey – I. Survey description and first evidence of ram pressure in the Fornax galaxy cluster. *arXiv e-prints*, arXiv:2302.11895. doi: 10.48550/arXiv.2302.11895

Shapiro, P. R., Iliev, I. T., & Raga, A. C. (2004, March). Photoevaporation of cosmological minihaloes during reionization. , *348*(3), 753-782. doi: 10.1111/j.1365-2966.2004.07364.x

Shields, G., Gebhardt, K., Salviander, S., Wills, B., Xie, B., Brotherton, M., ... Dietrich, M. (2008, 12). The black hole-bulge relationship in quasars. *The Astrophysical Journal*, *583*, 124. doi: 10.1086/345348

Sijacki, D., Springel, V., Di Matteo, T., & Hernquist, L. (2007, September). A unified model for AGN feedback in cosmological simulations of structure formation. , *380*(3), 877-900. doi: 10.1111/j.1365-2966.2007.12153.x

Simionescu, A., Werner, N., Finoguenov, A., Böhringer, H., & Brüggen, M. (2008, April). Metal-rich multi-phase gas in M 87. AGN-driven metal transport, magnetic-field supported multi-temperature gas, and constraints on non-thermal emission observed with XMM-Newton. , *482*(1), 97-112. doi: 10.1051/0004-6361:20078749

Snowden, S. L., Mushotzky, R. F., Kuntz, K. D., & Davis, D. S. (2008, February). A catalog of galaxy clusters observed by XMM-Newton. , *478*(2), 615-658. doi: 10.1051/0004-6361:20077930

Sparre, M., Pfrommer, C., & Vogelsberger, M. (2019, February). The physics of multiphase gas flows: fragmentation of a radiatively cooling gas cloud in a hot wind. , *482*(4), 5401-5421. doi: 10.1093/mnras/sty3063

Spitzer, L. (1978). *Physical processes in the interstellar medium.* doi: 10.1002/9783527617722

Springel, V. (2005, December). The cosmological simulation code GADGET-2. , *364*(4), 1105-1134. doi: 10.1111/j.1365-2966.2005.09655.x

Springel, V. (2010, jan). ie pur si muove:/igalilean-invariant cosmological hydrodynamical simulations on a moving mesh. *Monthly Notices of the Royal Astronomical Society*, *401*(2), 791–851. Retrieved from https://doi.org/10.1111%2Fj.1365-2966.2009.15715.x doi: 10.1111/j.1365-2966.2009.15715.x

Springel, V. (2021). *Modern computational astrophysics: Concepts and applications.* University Lecture.

Springel, V., & Hernquist, L. (2003, February). The history of star formation in a Λ cold dark matter universe. , *339*(2), 312-334. doi: 10.1046/j.1365-8711.2003.06207.x

Springel, V., White, S. D. M., Jenkins, A., Frenk, C. S., Yoshida, N., Gao, L., ... Pearce, F. (2005, June). Simulations of the formation, evolution and clustering of galaxies and quasars. , *435*(7042), 629-636. doi: 10.1038/nature03597

Springel, V., White, S. D. M., Tormen, G., & Kauffmann, G. (2001, December). Populating a cluster of galaxies - I. Results at [formmu2]z=0. , *328*(3), 726-750. doi: 10.1046/j.1365-8711.2001.04912.x

Steinwandel, U. P., Böss, L. M., Dolag, K., & Lesch, H. (2022, July). On the Small-scale Turbulent Dynamo in the Intracluster Medium: A Comparison to Dynamo Theory. , *933*(2), 131. doi: 10.3847/1538-4357/ac715c

Subramanian, K. (2008, February). Magnetizing the universe. *arXiv e-prints*, arXiv:0802.2804.

Subramanian, K. (2016, July). The origin, evolution and signatures of primordial magnetic fields. *Reports on Progress in Physics*, *79*(7), 076901. doi: 10.1088/0034-4885/79/7/076901

Subramanian, K. (2018, September). Magnetic Fields in the Universe. *arXiv e-prints*, arXiv:1809.03543.

Taylor, G. B., Govoni, F., Allen, S. W., & Fabian, A. C. (2001, September). Magnetic fields in the 3C 129 cluster. , *326*(1), 2-10. doi: 10.1046/j.1365-8711.2001.04587.x

Torrey, P., Hopkins, P. F., Faucher-Giguère, C.-A., Anglés-Alcázar, D., Quataert, E., Ma, X., ... Murray, N. (2020, October). The impact of AGN wind feedback in simulations of isolated galaxies with a multiphase ISM. , *497*(4), 5292-5308. doi: 10.1093/mnras/staa2222

Treumann, R. A., & Baumjohann, W. (2013, December). Collisionless Magnetic Reconnection in Space Plasmas. *Frontiers in Physics*, *1*, 31. doi: 10.3389/fphy.2013.00031

Urry, C. M., & Padovani, P. (1995, September). Unified Schemes for Radio-Loud Active Galactic Nuclei. , *107*, 803. doi: 10.1086/133630

Vachaspati, T. (1991, August). Magnetic fields from cosmological phase transitions. *Physics Letters B*, *265*(3-4), 258-261. doi: 10.1016/0370-2693(91)90051-Q

Valdarnini, R. (2019, March). A Multifiltering Study of Turbulence in a Large Sample of Simulated Galaxy Clusters. , *874*(1), 42. doi: 10.3847/1538-4357/ab0964

Vallés-Pérez, D., Planelles, S., & Quilis, V. (2021, June). Troubled cosmic flows: turbulence, enstrophy, and helicity from the assembly history of the intracluster medium. , *504*(1), 510-527. doi: 10.1093/mnras/stab880

van Weeren, R. J., de Gasperin, F., Akamatsu, H., Brüggen, M., Feretti, L., Kang, H., ... Zandanel, F. (2019, February). Diffuse Radio Emission from Galaxy Clusters. , *215*(1), 16. doi: 10.1007/s11214-019-0584-z

van Weeren, R. J., Röttgering, H. J. A., Bagchi, J., Raychaudhury, S., Intema, H. T., Miniati, F., ... Erben, T. (2009, November). Radio observations of ZwCl 2341.1+0000: a double radio relic cluster. , *506*(3), 1083-1094. doi: 10.1051/0004-6361/200912287

Van De Ven, G., Mandelbaum, R., & Keeton, C. R. (2009, 09). Galaxy density profiles and shapes – I. Simulation pipeline for lensing by realistic galaxy models. *Monthly Notices of the Royal Astronomical Society*, *398*(2), 607-634. Retrieved from https://doi.org/10.1111/j.1365-2966.2009.15167.x doi: 10.1111/j.1365-2966.2009.15167.x

Vazza, F., Brüggen, M., Gheller, C., & Wang, P. (2014, December). On the amplification of magnetic fields in cosmic filaments and galaxy clusters. , *445*(4), 3706-3722. doi: 10.1093/mnras/stu1896

Vazza, F., Brunetti, G., Brüggen, M., & Bonafede, A. (2018, February). Resolved magnetic dynamo action in the simulated intracluster medium. , *474*(2), 1672-1687. doi: 10.1093/mnras/stx2830

Vazza, F., Jones, T. W., Brüggen, M., Brunetti, G., Gheller, C., Porter, D., & Ryu, D. (2017, January). Turbulence and vorticity in Galaxy clusters generated by structure formation. , *464*(1), 210-230. doi: 10.1093/mnras/stw2351

Veilleux, S., Cecil, G., & Bland-Hawthorn, J. (2005, September). Galactic Winds. , *43*(1), 769-826. doi: 10.1146/annurev.astro.43.072103.150610

Vikhlinin, A. (2019, September). Lynx X-ray Observatory. In *Bulletin of the american astronomical society* (Vol. 51, p. 30).

Vogelsberger, M., Genel, S., Sijacki, D., Torrey, P., Springel, V., & Hernquist, L. (2013, December). A model for cosmological simulations of galaxy formation physics. , *436*(4), 3031-3067. doi: 10.1093/mnras/stt1789

Vogelsberger, M., Marinacci, F., Torrey, P., Genel, S., Springel, V., Weinberger, R., ... Nelson, D. (2018, February). The uniformity and time-invariance of the intra-cluster metal distribution in galaxy clusters from the IllustrisTNG simulations. , *474*(2), 2073-2093. doi: 10.1093/mnras/stx2955

Von Der Linden, A., Best, P. N., Kauffmann, G., & White, S. D. M. (2007, August). How special are brightest group and cluster galaxies? , *379*(3), 867-893. doi: 10.1111/j.1365-2966.2007.11940.x

Wada, K., Papadopoulos, P. P., & Spaans, M. (2009, September). Molecular Gas Disk Structures Around Active Galactic Nuclei. , *702*(1), 63-74. doi: 10.1088/0004-637X/702/1/63

Walker, S., & Nagai, D. (2019, May). Unveiling the Galaxy Cluster - Cosmic Web Connection with X-ray observations in the Next Decade. , *51*(3), 218.

Wang, L., & Steinhardt, P. J. (1998, December). Cluster Abundance Constraints for Cosmological Models with a Time-varying, Spatially Inhomogeneous Energy Component with Negative Pressure. , *508*(2), 483-490. doi: 10.1086/306436

Weinberger, R., Su, K.-Y., Ehlert, K., Pfrommer, C., Hernquist, L., Bryan, G. L., ... Faucher-Giguère, C.-A. (2022, November). Active galactic nucleus jet feedback in hydrostatic halos. *arXiv e-prints*, arXiv:2211.11771. doi: 10.48550/arXiv.2211.11771

White, S. D. M., & Frenk, C. S. (1991, September). Galaxy Formation through Hierarchical Clustering. , *379*, 52. doi: 10.1086/170483

Wiersma, R. P. C., Schaye, J., & Smith, B. D. (2009, February). The effect of photoionization on the cooling rates of enriched, astrophysical plasmas. , *393*(1), 99-107. doi: 10.1111/j.1365-2966.2008.14191.x

Wiersma, R. P. C., Schaye, J., Theuns, T., Dalla Vecchia, C., & Tornatore, L. (2009, October). Chemical enrichment in cosmological, smoothed particle hydrodynamics simulations. , *399*(2), 574-600. doi: 10.1111/j.1365-2966.2009.15331.x

Winske, D., & Quest, K. B. (1988, September). Magnetic field and density fluctuations at perpendicular supercritical collisionless shocks. , *93*(A9), 9681-9693. doi: 10.1029/JA093iA09p09681

Wittor, D., & Gaspari, M. (2020, November). Dissecting the turbulent weather driven by mechanical AGN feedback. , *498*(4), 4983-5002. doi: 10.1093/mnras/staa2747

Wittor, D., Jones, T., Vazza, F., & Brüggen, M. (2017, November). Evolution of vorticity and enstrophy in the intracluster medium. , *471*(3), 3212-3225. doi: 10.1093/mnras/stx1769

Woosley, S. E., & Weaver, T. A. (1995, November). The Evolution and Explosion of Massive Stars. II. Explosive Hydrodynamics and Nucleosynthesis. , *101*, 181. doi: 10.1086/192237

Xu, H. (2009). *The AGN origin of cluster magnetic fields* (Unpublished doctoral dissertation). University of California, San Diego.

Xu, S., & Lazarian, A. (2020, August). Nonlinear Turbulent Dynamo during Gravitational Collapse. , *899*(2), 115. doi: 10.3847/1538-4357/aba7ba

Yoshida, N., Abel, T., Hernquist, L., & Sugiyama, N. (2003, August). Simulations of Early Structure Formation: Primordial Gas Clouds. , *592*(2), 645-663. doi: 10.1086/375810

Yoshida, N., Omukai, K., Hernquist, L., & Abel, T. (2006, November). Formation of Primordial Stars in a ΛCDM Universe. , *652*(1), 6-25. doi: 10.1086/507978

Zakamska, N. L., Hamann, F., Pâris, I., Brandt, W. N., Greene, J. E., Strauss, M. A., ... Ross, N. P. (2016, July). Discovery of extreme [O III] λ5007 Å outflows in high-redshift red quasars. , *459*(3), 3144-3160. doi: 10.1093/mnras/stw718

Zenteno Vivanco, A. A. (2014). *Galaxy populations in galaxy clusters selected by the Sunyaev-Zeldovich Effect* (Unpublished doctoral dissertation). Ludwig-Maximilians University of Munich, Germany.

Zhang, C., Wu, Y., Sinclair, M., Farrell, A., Marsh, K. A., Petrushina, I., ... Joshi, C. (2022, December). Mapping the self-generated magnetic fields due to thermal Weibel instability. *Proceedings of the National Academy of Science*, *119*(50), e2211713119. doi: 10.1073/pnas.2211713119

Zhang, C., Zhuravleva, I., Gendron-Marsolais, M.-L., Churazov, E., Schekochihin, A. A., & Forman, W. R. (2022, November). Bubble-driven gas uplift in galaxy clusters and its velocity features. , *517*(1), 616-631. doi: 10.1093/mnras/stac2282

Zhao, F., Alvarez, M., & Abel, T. (2008, March). The Biermann Battery and Early Structure Formation. In B. W. O'Shea & A. Heger (Eds.), *First stars iii* (Vol. 990, p. 39-41). doi: 10.1063/1.2905616

B Declaration of Authorship

I hereby certify that I have written this thesis independently and that I have not used any sources or auxiliaries other than those indicated.

Larissa Tevlin